Dynamic Compensation Using High-speed Visual Feedback Based on Relative Coordinate

（相対座標における高速視覚フィードバックに基づくダイナミックコンペンセーション）

黄　守仁

Abstract

High-performance interactive manipulations such as high-speed and accurate endpoint regulations towards a dynamically uncertain target in a large workspace by the robotic system are very attractive for manufacturing industry. However, it has been rather challenging for a traditional big industrial robot to accomplish such regulations, not only due to the difficulty in building the real-time feedback system, but also due to the mechanical defects like backlash as well as the nonlinear dynamics, especially under high-speed motions, while most of the commercial industrial robots are controlled without modeling the complex dynamic models.

In order to deal with this problem, this thesis propose a dynamic compensation concept. The dynamic compensation concept is realized by fusing the high-speed visual feedback based on relative coordinate information and a high-speed lightweight compensation actuator (for fine regulation) to cooperate with the main traditional robot (for coarse regulation). The methodology of the proposed concept is that: the high-speed vision sensing in terms of task-space can inspect the uncertain target as well as the dynamic uncertainties brought by the main robot (the main plant) under high-speed motions, and by the compensation actuator (the compensation plant), which is capable of high-speed response, the uncertainties can be compensated based on the relative coordinate visual information between target, main plant and compensation plant. Here, the high-speed visual feedback refers to 1000 Hz feedback of image features, and hereafter, the robotic system developed based on the proposed concept is referred as the dynamic compensation robotic system (DCRS). With experimental evaluations of the dynamic compensation concept based on a 1-DOF DCRS prototype, the quantitative analysis of the two aspects of the proposed concept is conducted. By exploiting the feature of the DCRS, a simplified image-based visual servo (IBVS) approach is proposed for control of the main robot arm, and a pre-compensated proportional-derivative (PD) control method is proposed for the compensation actuator.

As the basic application, the 1D dynamic picking for a flying object is addressed by a 1-DOF DCRS. With the proposed pre-compensation fuzzy logic control (PFLC) algorithm for compensation plant and the cooperation algorithm for coordinating the big range coarse positioning (by main plant) and the accurate positioning within a small range (by compensation plant), dynamic picking (catching) of a flying object with small clearance is realized. After that, as the extension, the application task - 3D peg-and-hole alignment with large position and attitude uncertainty is addressed by the monocular approach and binocular approach with the introduction of a high-speed active peg as well as the high-speed visual feedback based on the dynamic compensation concept. Both the 1D dynamic picking task and the 3D peg-and-hole alignment task show that the system can realize high-speed as well as accurate interactive manipulation without much calibrations and without modeling of the system's dynamics. At last, conclusions are summarized and a scenario for application in the near future is presented to unveil the promising prospect of the proposed dynamic compensation concept in manufacturing.

Contents

List of Figures

List of Tables

Chapter 1

Introduction

1.1 The background

Robots have been employed in automation industry for several dozens of years. With advantages such as good accuracy, big power, as well as good reliability than human, they find applications in the so-called "4D tasks", tasks that are dangerous, dull, dirty or dumb [6]. As the human population ages and the number of wage earners becomes a smaller fraction of our population, robots have already been accelerating their process of filling in the labor for manufacturing. As an example, in June 2011, Foxconn CEO Terry Gou announced plans to deploy one million robots across factory assembly lines, as part of a company-wide effort to adopt more automated manufacturing processes and cope with rising labor costs [7].

Nowadays industrial robot has a good performance in doing autonomous manipulations in some structured environment and for instance, is capable of realizing accurate repetitive positioning even under high-speed motions. However, robots would have far less impact in applications where the object placement and the environment cannot be accurately controlled. For the realization of interactive manipulations where the target as well as the environment is dynamically uncertain, the difficulty in building the real-time feedback system, as well as the mechanical defects like backlash and the nonlinear dynamics of the robot especially under high-speed motions are still blocking the way of robot's applications in lots of fields. In order to build the feedback system for interactive manipulations, sensors for robot, target and environment should be configured, and sensor integration has been supposed to be fundamental to increase the versatility and application of robots. Among the many types of sensors, vision sensor is one of the most important sensors which have been widely used in robotic control because of its many advantages such as non-contact sensing, safety, flexibility, full of information and so on.

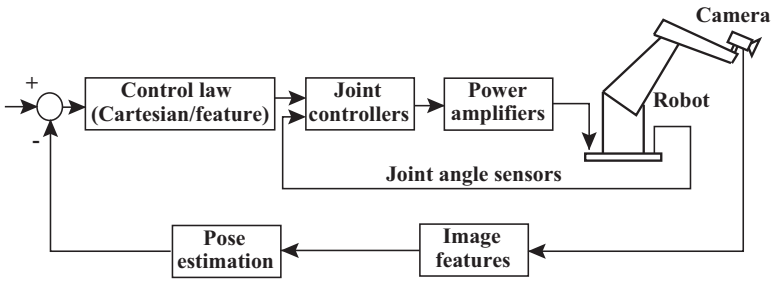

Figure 1.1: The dynamic look-and-move approach

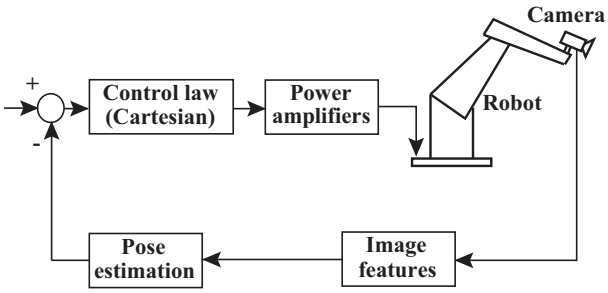

Figure 1.2: The position-based visual servo approach

1.1.1 Robotic control based on vision sensors

1.1.1.1 Traditional approaches

There are several categories for robotic control based on visual feedback, such as the dynamic look-and-move approach, position-based visual servo (PBVS), image-based visual servo (IBVS) [8]. The look-and-move approach is implemented in a hierarchical way and holds two feedback loops as shown in Figure 1.1, an inner kinematic loop and an outer visual feedback loop, and still most of the commercial robots adopt this approach for several reasons [8]. One of the main reasons has been the great gap between the low sampling rates of the vision loop (for instance, 30 Hz) and the high sampling rates of the joint level feedback (for instance, 1000 Hz). Visual control algorithms have been developed separately from the kinematic loop without considering the dynamic interactions between these two loops. However, as has been pointed out in [9], this approach may work well for slow robot motion, but not for high-speed manipulations where the robot dynamics are not negligible.

The PBVS approach (shown in Figure 1.2) basically needs the recovering of the 3D information from images and has a strict request on the accurate

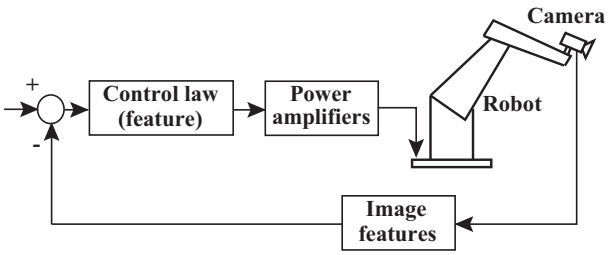

Figure 1.3: The image-based visual servo approach

Table 1.1: Summary of three control approaches based on vision sensor.

	Look-and-move	PBVS	IBVS
Fit for uncertain kinematics	×	△	△
Global optimal regulation	◯	◯	×
Less camera calibration	×	×	◯
Robust to noise	×	△	◯
High-speed regulation	×	△	△

×: negative; △: possible ; ◯: positive

calibration for cameras. Since the feedback is computed by reducing errors in estimated pose space, it is possible to lose the image features during regulation process by PBVS approach.

The IBVS approach (shown in Figure 1.3) is generally assumed to be much more suitable for applications due to its robustness to calibration errors and easy control for keeping the image features within the camera's field of view. However, IBVS has its own weaknesses, such as the interaction matrix being dependent on the depth of feature points and thus not being directly available. An interaction matrix built by current image features and estimated depth may involve inadequate camera motion, leading to possible local minima or task singularities (especially when point features are used) [10].

Features for these three approaches are summarized in Table 1.1. As for the high-speed regulation issue, the PBVS and IBVS approach may be adoptable if the dynamic model of the system is available. Besides, in order to realize the smooth high-speed regulation, high-speed vision systems should be provided.

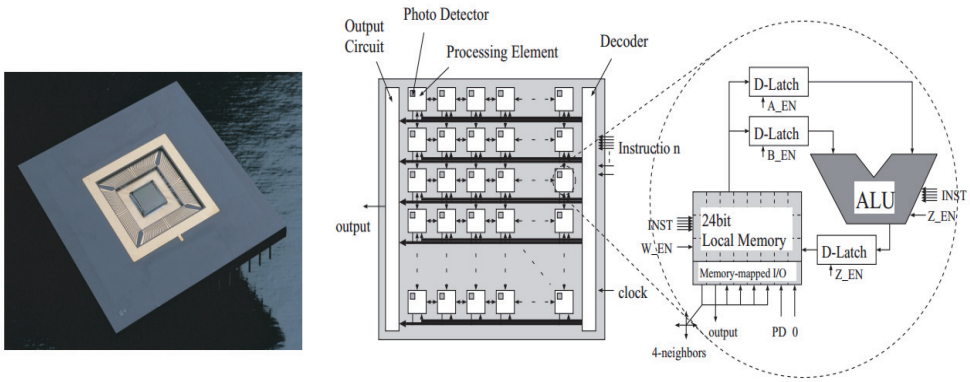

Figure 1.4: Vision chip and its architecture [1]

1.1.1.2 High-speed vision systems

In the common knowledge, the feedback rate of a vision sensor is still far more beyond the needs of real-time control, for instance, most CCD cameras are restricted to the video frame rate (NTSC 30 Hz, PAL 25 Hz), and this is the main reason for the two-loop design of the dynamic look-and-move approach for robotic control as described above. However, high-speed vision system such as column parallel vision (CPV) with 1KHz feedback rate has been introduced more than ten years ago [1, 11]. As shown in Figure 1.4, the CPV system has a 128×128 PD array and an all parallel processor array connect to each other in a column parallel architecture, thus high-speed image transfer was realized. High-speed vision system not only provides with the great possibility of real-time control based on high-speed feedback information in terms of task-space, but also does good to the image processing algorithm. Nowadays, high-speed vision systems with much better performance are commercially available, such as EoSens system, and we will introduce them in the next chapter.

1.1.1.3 Evaluation of robotic interactive manipulation

As a background for robotic interactive manipulation based on vision sensors, we focus on several key aspects for evaluation as shown in Figure 1.5: accuracy, speed, flexibility, workspace, in-dependency of models (dynamic models or kinematic models). For most commercially available industrial manipulators, their control systems are treated as decoupled systems and dynamics are neglected thereby known as non-model-based controllers [12]. Such approximation is acceptable for low-speed motion since Coriolis and centripetal torques are limited due to powerful motors and high gear reductions [12, 13]. However, this approach

can not apply for high-speed motions [14]. On the other hand, most of the industrial manipulators are controlled highly dependent on their accurate kinematic models. Besides, a majority of solutions for the automation of industrial robots through the adoption of vision sensors are based on the strict calibrations of camera and robot's coordinate systems. These reasons have led to a poor flexibility for robots, and they are limited to structured environments. Recently, by means of high-speed visual feedback as well as high-speed dynamic manipulation strategies, several fantastic manipulations and applications have been conducted in *Ishikawa Oku laboratory, the University of Tokyo*. In [15, 16], with the adoption of a high-speed active stereo vision system as well as a high-speed manipulator, the batting action for a plastic ball with an initial velocity of about 6-8 m/s were successfully realized for most of the time. In [17, 18, 19], high-speed tracking and controlling of micro-organisms have been realized with satisfying accuracy on a small work range XY-stage. As a summary, currently, most robotic manipulations are realized with the trade-off among these five aspects. However, it will be rather difficult to realize the robotic interactive manipulation that has good scores in all of these five issues, because of issues such as backlash of mechanism, nonlinear dynamics of large robots, calibration errors both on robot and sensors, as well as the delay of the feedback for the dynamical unstructured environment. Among these issues, the conflict between the motion speed and accuracy is a great weakness for conventional heavy industrial robots because of the complex nonlinear dynamics issue as well as the mechanical backlash. In order to reach a good trade-off between these issues, the dynamic compensation is the main approach to address it. Throughout of this thesis, we will focus on the dynamic compensation approach in coping with the five issues of the robotic interactive manipulation.

1.1.2 Traditional approaches for dynamic compensation

In order to deal with the nonlinear dynamics issue, the general approach is to realize dynamic compensation by identifying the parameters of the dynamic model which is known as the model-based approach [12, 20, 21]. However, the problem is that the computation is too complex to realize real-time compensation, and the physical values of the dynamic model are difficult to estimate and often not known accurately. Moreover, these parameter values may change with robot ages or robot configurations. Adaptive control methods (e.g., [22, 23, 24]) are thus proposed to deal with uncertain parameters of dynamic models. The adaptive approach attempts to 'learn' the uncertain parameters of the system, and it can be applicable to a wider range of uncertainties. However, usually the computation for adaptive control is complex. Besides, the adaptive control exhibits poor transient behavior and may result to the possible loss of exponential stability of

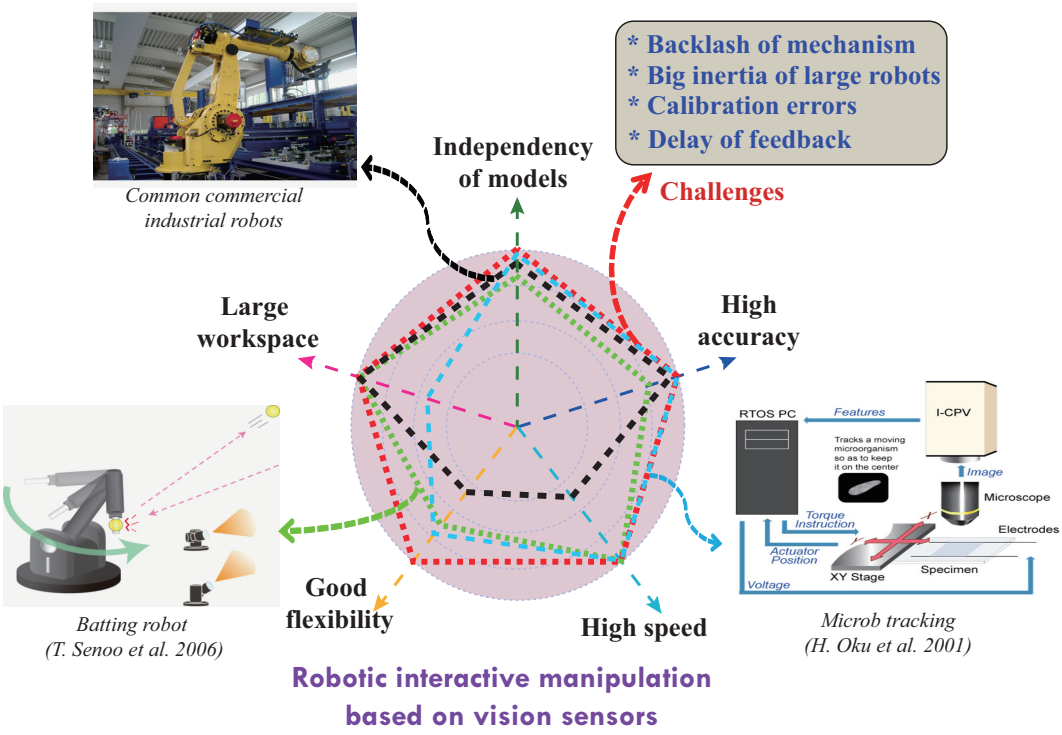

Figure 1.5: A background for robotic interactive manipulation based on vision sensor

the overall control system [25].

For the control of robots within a constraint space i.e., the end-effector are in contact with the environment, dynamic compensation approaches based on impedance control [26] have been conducted [27, 28]. The methodology of impedance control is that the motion of the manipulator is governed by a spring-like behavior, the control torques on the robot mimic a spring that is connected between the end-effector and its desired position. The objective of the impedance control is not to control force and position but to control their dynamic relationship i.e., the desired impedance along each task-space direction.

There is another approach by mounting a small robot onto the robot arm known as the macro-micro architecture [29, 30]. The macro-micro approach has been proposed to apply to rigid manipulators for increasing system bandwidth, as well as to flexible manipulators for suppressing bending vibrations and improving dynamic tracking performance (e.g., [31, 32]). Since the micro-manipulator is mounted on the macro-manipulator, the system is dynamically coupled, especially for flexible manipulators [33, 34], and several complex control methods involving the system's dynamics have been proposed (e.g., [35]). Whereas, in real factory

and automation field, the simple control methods are much more practical for implementation.

Usually, for a lightweight micro-manipulator, the coupling dynamic interaction to the macro part is negligible as the inertia of the macro part is much greater than that of the micro part [36, 37]. In [36], the dynamic effect of the macro part to the micro part is represented by a disturbance force, and by choosing a large proportional gain factor of the PD controller for the micro-manipulator, the disturbance force can be reduced and the system stability can be proved. It should be noted that this approach is model independent, and it represents a kind of methods that don't need to model the system's dynamics. Although this approach is very simple and easy for application in case of static positioning, it can hardly be a general approach for dynamic positioning where the acceleration of the system should be dynamically accommodated. In [35] and [38], the dynamic trajectory tracking problems have been studied, and the dynamics of the system were taken into account with a fine model including the macro-manipulator's deformation. In [35], a simple PD controller is assigned for the macro-manipulator, and a non-linear dynamic compensating control law is applied to the micro-manipulator. In [38], an oppose strategy is adopted by applying the PD control to the micro part, and adopting the nonlinear controller for the macro part to damp out vibrations. In both approaches the trajectory planner is needed for the macro-manipulator. These approaches obtained good performance for dynamic compensation, yet the modeling for the system's dynamics is not easy.

1.2 Purpose of this research

The purpose of this research is to come up with a practical solution for realizing high-speed, accurate endpoint interactive regulation towards an uncertain target within an unstructured large workspace, and the simple robust control strategy such as dynamic model independent control is favorable.

As shown in Figure 1.6, by using high-speed visual feedback based on relative coordinate information and high-speed & lightweight compensation actuator, this research presents a simple methodology of dynamic compensation for a traditional robot arm to enable interactive regulations with high performance. In particular, for robot arms of which the dynamic models are not accurately calibrated or even not known, yet high-speed or fast position regulations are expected to be realized with good accuracy, the proposed approach may be a highly practical solution. Since the proposed dynamic compensation concept is based on modular cooperation, and the main robot is only scheduled for coarse regulation, a great number of tradition heavy robots that exhibit poor performance under high-speed regulation or suffer from large regulation errors after long years of mechanical

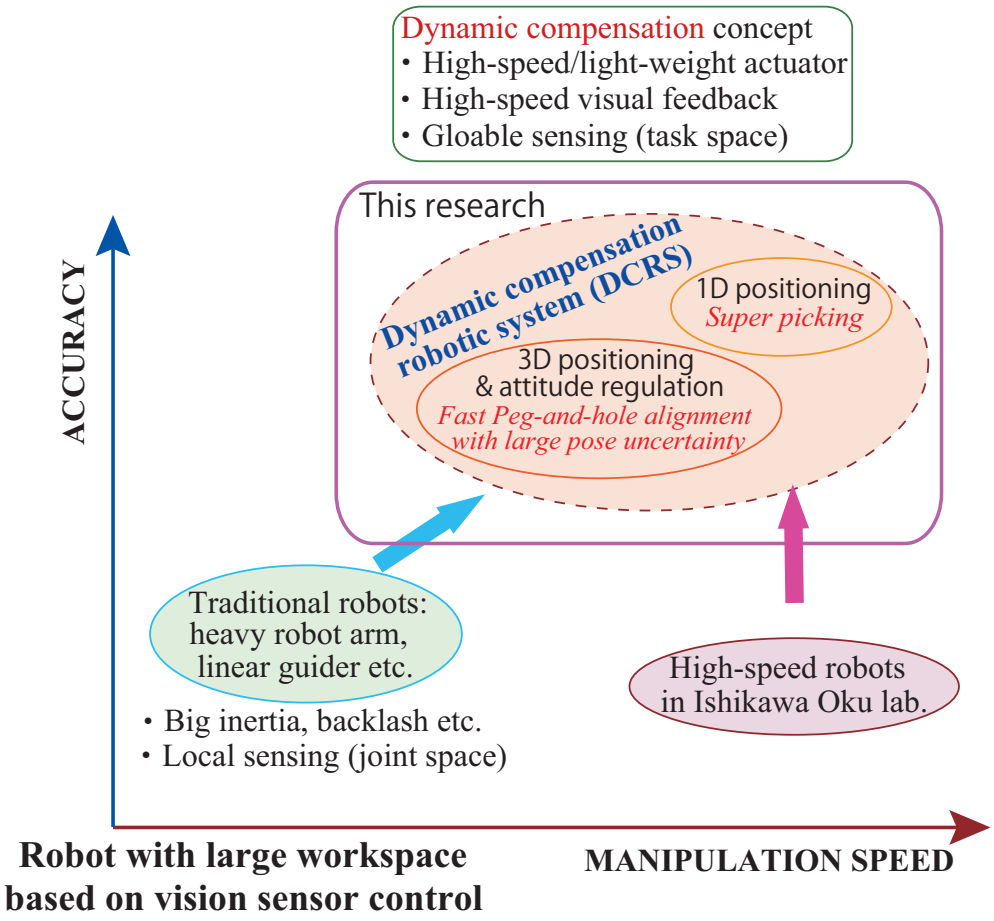

Figure 1.6: The purpose of this research

wear can be reformed to accomplish high performance regulations according to the proposed concept. The developed system based on the proposed concept will be referred as the dynamic compensation robotic system (DCRS) hereafter. In order to evaluate the effectiveness of the proposed dynamic compensation concept, a basic 1-DOF DCRS system will be designed to realize the 1D dynamic picking of flying objects for evaluation. As the extension, the task of 3D peg-and-hole alignment with large position and attitude uncertainty will be also addressed.

1.3 Overview of this thesis

As shown in Figure 1.7, this thesis is organized as follows:

In Chapter 2, the methodology of the proposed dynamic compensation ap-

proach will be introduced, and then the experimental systems used in this research will be addressed. With experimental evaluations of the dynamic compensation concept, the quantitative analysis on the two aspects of the proposed concept will be discussed.

In Chapter 3, by exploiting the feature of the DCRS, a simplified IBVS approach is proposed for control of the main robot arm, and a pre-compensated PD control method is proposed for the compensation actuator.

In Chapter 4, as the basic application, the 1D dynamic super picking for a flying object will be addressed by a 1-DOF DCRS. By introducing the pre-compensation fuzzy logic control (PFLC) algorithm for compensation plant and the cooperation algorithm for coordinating the big range coarse positioning by main plant and the accurate positioning by compensation plant within a small range, dynamic picking (catching) of a flying object with small clearance will be realized.

In Chapter 5, as the extension, the application task - 3D peg-and-hole alignment with large position and attitude uncertainty will be addressed based on the dynamic compensation approach. Both monocular approach and binocular approach will be realized by introducing a high-speed active peg as well as the high-speed visual feedback.

In Chapter 6, conclusions are summarized and a scenario for application in the near future is presented to unveil the promising prospect of the proposed dynamic compensation concept in manufacturing.

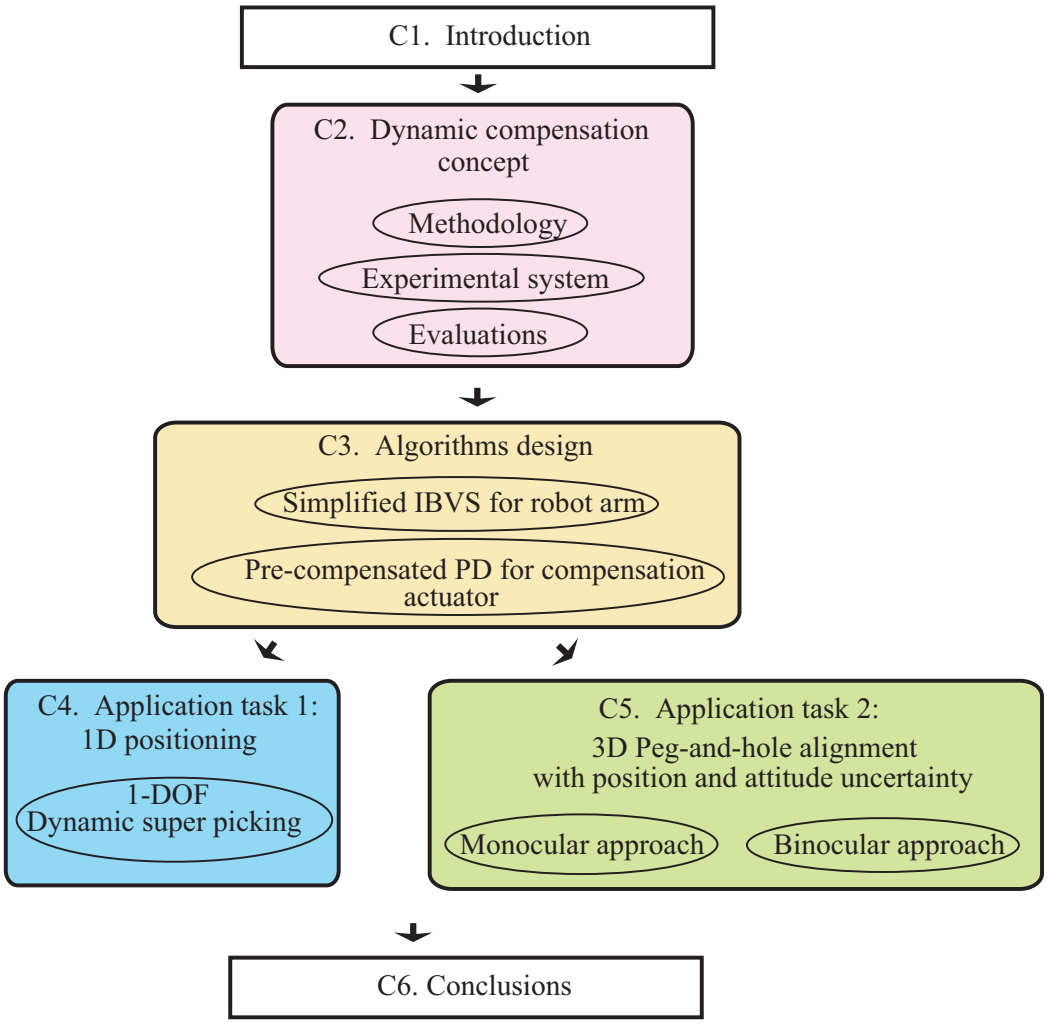

Figure 1.7: The structure of this thesis

Chapter 2

The proposed dynamic compensation concept

In this chapter, the concept of dynamic compensation through high-speed & lightweight compensation actuator as well as high-speed visual feedback based on relative coordinate is proposed. Quantitative experimental evaluations based on a 1-DOF DCRS prototype will be addressed. The experimental systems involved in this research will also be introduced.

2.1 The methodology

For high-speed operations, dynamic defects such as vibration due to large inertia of the robot arm and the backlash, would reduce the performance. Suppose for a general robot system as shown in Figure 2.1, there are some uncertainties about the kinematics as well as uncertainties about the system's calibrations (including the calibrations for sensors). Besides, the backlash for the joints of the robot also contribute to the systematic uncertainties. Now the robot is supposed to be regulated to reach the target's position with the high-speed visual feedback. The high-speed camera inspects both of the robot's tool point and the target point (since here we are analyzing the dynamic compensation for the uncertainties brought by robot itself, it is reasonable to assume the target to be motionless), thus it follows the endpoint close-loop method (ECL) [8]. Let's refer to the image feature of the target and that of the robot's tool to be $\boldsymbol{\xi}_T$ and $\boldsymbol{\xi}_r$ respectively from the high-speed visual feedback, and the error $\boldsymbol{e}$ for the regulation can be noted as:

$$\boldsymbol{e} = \boldsymbol{\xi}_r - \boldsymbol{\xi}_T \tag{2.1}$$

Assume the ideal accurate models for the interaction relationship (optical-motion model) as well as the kinematic model to be $\boldsymbol{J}_{img}$ and $\boldsymbol{J}_r$ respectively,

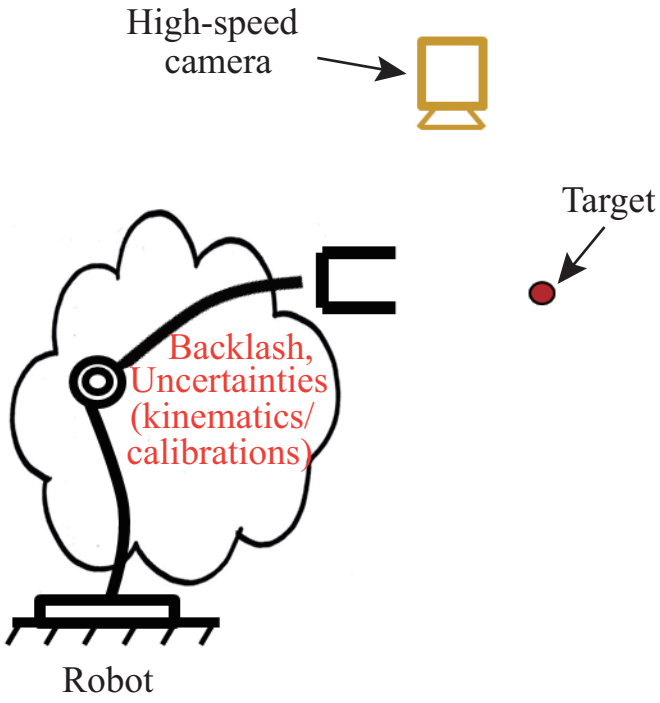

Figure 2.1: A general robot system with uncertainties

then we have

$$\dot{\boldsymbol{\xi}}_r = \boldsymbol{J}_{img} \cdot \boldsymbol{J}_r \cdot \dot{\boldsymbol{\theta}} \tag{2.2}$$

where $\dot{\boldsymbol{\theta}}$ represents the joint velocity vector. Exponential convergence of the regulation can be obtained if we apply the feedback control such as

$$\dot{\boldsymbol{\theta}} = -\lambda \cdot \boldsymbol{J}_r^{+} \cdot \boldsymbol{J}_{img}^{+} \cdot \boldsymbol{e} \tag{2.3}$$

where λ is a positive-definite coefficient, while $\boldsymbol{J}_{img}^{+}$ and $\boldsymbol{J}_r^{+}$ represents the pseudo-inverse of $\boldsymbol{J}_{img}$ and $\boldsymbol{J}_r$ respectively.

However, in the real case, due to the uncertainties of the system, there shall be the unknown factor within the regulation error, and we note it as $\boldsymbol{\delta}$ (although there may be several uncertainties, it is reasonable to sum them by one factor as the total effect on the regulation result of each step), then the error for the real case of the regulation at time of k, for instance, is

$$\boldsymbol{E}^k = \boldsymbol{\xi}_r^k + \boldsymbol{\delta}^k - \boldsymbol{\xi}_T \tag{2.4}$$

In order to compensate for the uncertain part $\boldsymbol{\delta}^k$ at time of k, we introduce a compensation part $\boldsymbol{\xi}_c^{k+1}$ which is to be realized by a lightweight and high-speed actuator at the next time cycle $k+1$, then we have

$$\boldsymbol{E}^{k+1} = \boldsymbol{\xi}_r^{k+1} + \boldsymbol{\delta}^{k+1} + \boldsymbol{\xi}_c^{k+1} - \boldsymbol{\xi}_T \tag{2.5}$$

Suppose $\boldsymbol{\xi}_r^k - \boldsymbol{\xi}_T \Rightarrow 0$ always exists under the ideal accurate models of the system, thus the value for the compensation part $\boldsymbol{\xi}_c^{k+1}$ can be obtained from the visual feedback as

$$\boldsymbol{\xi}_c^{k+1} = -\widehat{\boldsymbol{E}}^k \Rightarrow -\widehat{\boldsymbol{\delta}}^k \tag{2.6}$$

Since here, high-speed visual feedback is adopted, and the time gap between two control cycle is sufficiently small, then it is reasonable to make the following approximation as

$$\widehat{\boldsymbol{\delta}}^k \doteq \boldsymbol{\delta}^{k+1} \tag{2.7}$$

With Equations 2.5, 2.6, 2.7, we have

$$\boldsymbol{E}^{k+1} = \boldsymbol{\xi}_r^{k+1} - \boldsymbol{\xi}_T \Rightarrow 0 \tag{2.8}$$

From the analysis above, it can be seen that the system is still capable of realizing stable convergence although there is the constant existing of the uncertainty brought by many factors, thanks to the dynamic compensation. As well, the proposed dynamic compensation concept involves three important issues as:

- The compensation actuator should be fast enough to response to the dynamic uncertain factor;
- The approximation involved in Equation 2.7 requires the time between two control step to be small enough, or saying the feedback rate should be high-speed;
- The value for the compensation part $\boldsymbol{\xi}_c^{k+1}$ in Equation 2.6 from the visual feedback is the relative information towards the target position in image coordinates, and it can be directly obtained.

Note that although we have assumed the target to be motionless in the analysis above, it is reasonable to apply the same analysis to the general case where the target is uncertain under the high-speed visual feedback based on relative information between main plant, compensation plant and target. Since the time

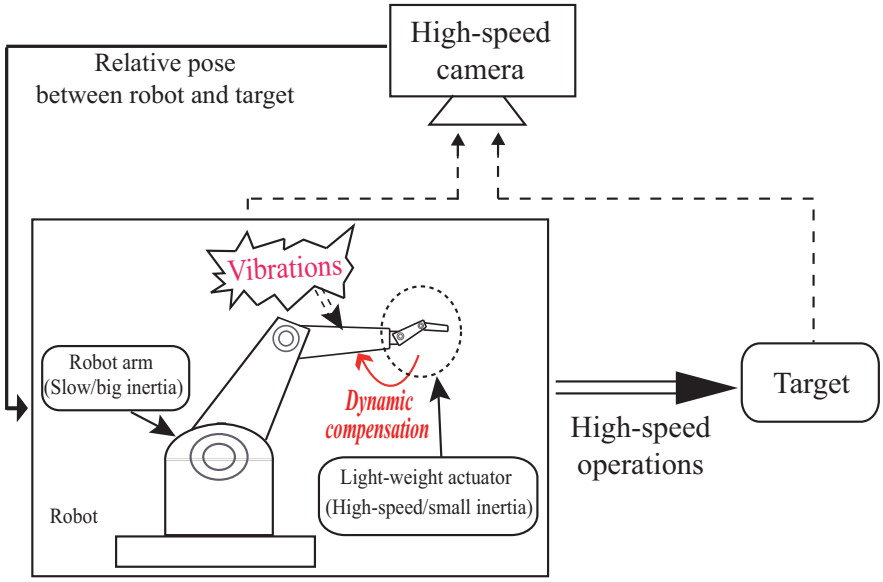

Figure 2.2: Concept of the proposed dynamic compensation

between two image frames is sufficiently small that we can ignore the target's motion.

Based on the analysis above, the proposed dynamic compensation concept in this research is shown in Figure 2.2. The compensation actuator with small inertia offers the necessary DOFs to compensate for the robot arm's dynamical uncertainties. The high bandwidth means it can realize quick response during the robot arm's dynamical converge, which is always realized in a very short time. At the same time, high-speed cameras are adopted to provide with feedback information of the relative information between main plant, compensation plant and target. Since the compensation actuator can realize quick response with the high-speed visual feedback, a simple PD control law may be adoptable, and the dynamic model of the system is not needed.

It should be pointed out that, although the proposed concept is somehow similar to the traditional macro-micro approach as has been described by the related works [29, 30, 31, 32, 33, 34, 35, 39], there are several different issues focused in this study as follows:

- High-speed visual feedback that offers the relative position information between robot and target is one important aspect of the proposed dynamic compensation concept, whereas the traditional macro-micro system itself doesn't involve a global high-speed visual feedback;

- The traditional macro-micro systems have been proposed mainly for regu-

lating flexible robotic systems such as the macro-micro manipulator (3M) system. Whereas our concept is more focused on accomplishing the high-speed and accurate interactive manipulations;

- In our dynamic compensation concept, rather than analyzing the complicated dynamic models and dynamic couplings, we focus on developing a simple control law that is easy for implementation. This is not only for relief of the works in real applications, but also for the versatility issue to adapt for much more applications;
- The relationship between visual feedback rate and compensation performance;
- The relationship between the compensation performance and the difference of bandwidth between robot arm and compensation actuator.

2.2 Experimental systems

In order to realize the proposed dynamic compensation concept, robots (including big workspace robots that realize coarse motion and small high-speed lightweight robot modules to realize dynamic compensation), high-speed vision sensors and image processing, as well as the real-time computation system have been adopted. We will address them one by one as follows.

2.2.1 Robots

5-DOF high-speed robot arm

A high-speed robot arm [2] as shown in Figure 2.3 is adopted. The maximum velocity of the robot arm's end-effector can reach 27.22 m/s. The D-H parameters and specifications for actuators of the high-speed robot arm is listed in Table 2.1 and Table 2.2 respectively.

2-DOF high-speed finger module

One finger module (Figure 2.4) of the high-speed hand [40] developed by our laboratory is adopted in this research. The high-speed hand has been adopted in several applications such as one of the hot topics of these days - the Janken (rock-paper-scissors) Robot with 100% winning rate [41] and good performance for high-speed dynamic manipulations has been demonstrated [42]. The finger is lightweight and capable of high-speed motion, and it can close its joints at a speed of 1800° / s. Its specification is listed in Table 2.3.

Table 2.1: D-H parameters for the robot arm.

i	a_{i-1}	α_{i-1}	d_i	θ_i
1	0	$\pi/4$	367.7	θ_1
2	0	-$\pi/4$	200	θ_2
3	0	-$\pi/2$	360	θ_3
4	0	$\pi/2$	-85	θ_4
5	0	-$\pi/2$	175	θ_5

Table 2.2: Specification of actuators of the robot arm.

	Joint 1	Joint 2	Joint 3	Joint 4	Joint 5
Reduction ratio	50	50	50	50	50
Max. angular velocity (rad/sec)	9.42	11.73	9.42	5.23	5.23
Max. torque (Nm)	150	150	150	32.5	32.5

Table 2.3: Specification of high-speed finger module

	Tip joint	Root joint
Reduction ratio	30	50
Max. angular velocity (rad/sec)	30	30
Max. torque (Nm)	0.245	1.71
Peak power output (W)	8	53
Weight (g)	25	60

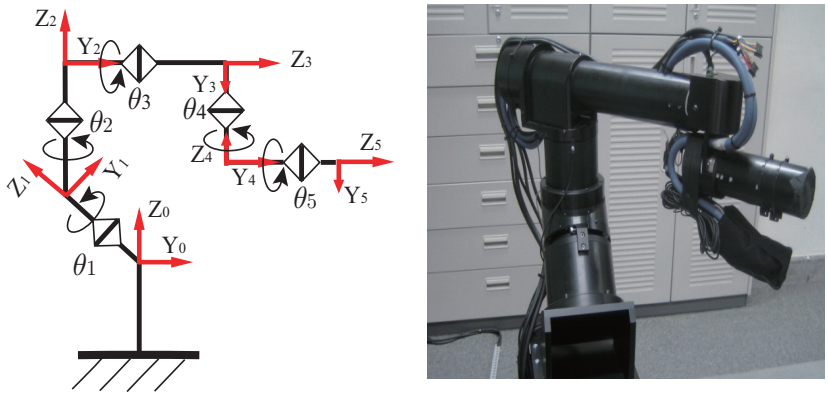

Figure 2.3: High-speed robot arm

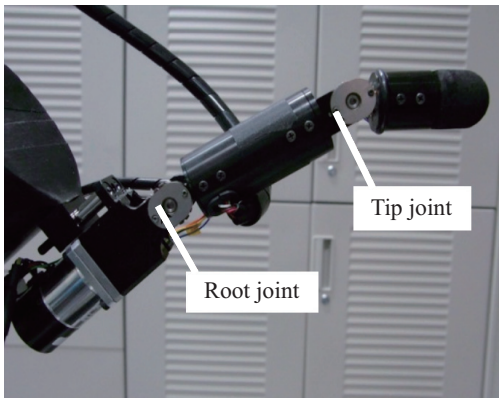

Figure 2.4: High-speed finger module

1-DOF linear slider

1-DOF linear slider (GLM10-075-M-EP-C-NN-K-A-N-N) made by THK is adopted as the main robot to realize high-speed coarse positioning. It has a motion range of 0.75 m, with the maximum motion speed of 2.0 m/s and the maximum load of 12 Kg. The photo of the slider is shown in Figure 2.5.

High-speed linear DC-servo motor

QUICKSHAFT Linear DC-Servomotor LM 1247 (Figure 2.6) made by FAULHABER [3] is adopted in this research as the compensation actuator. It can reach the maximum speed of 2.9 m/s, with the maximum acceleration of 148.5 m/s^2.

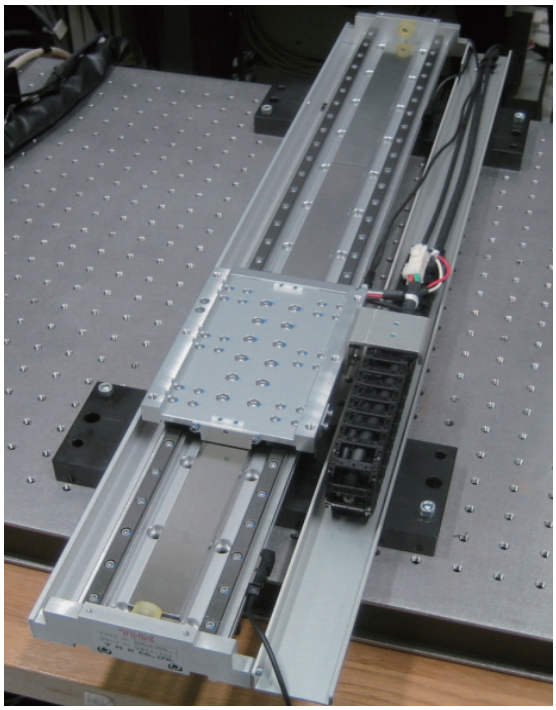

Figure 2.5: 1-DOF linear slider [2]

2.2.2 High-speed visual feedback

High-speed vision sensors

In this research, two EoSens MC1362 high-speed cameras (Figure 2.7) made by Mikrotron [4] and one IDP-Express R2000 high-speed camera (Figure 2.8) made by Photron [5] are adopted. Specifications for these cameras are listed in Table 2.4.

Image processing

Since the research has been focused on the visual servoing, light reflecting markers are adopted to simplify the image processing algorithms. At first, binarization based on a calibrated threshold for targets is implemented on the gray scale input images. For each target, we apply the queue-linear flood fill algorithm [43] to calculate the center of mass in image coordinates with the following method [44]. For the binary image $B(x, y)$, the image position for the target's center of mass $(\bar{x}, \bar{y})$ is calculated by

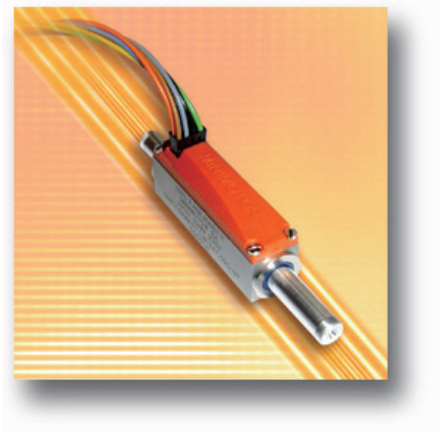

Figure 2.6: High-speed Linear DC-Servomotor LM 1247 [3]

Table 2.4: Specification for the High-speed cameras.

	EoSens MC1362	Photron IDP-Express R2000
Resolution	720×720	512×512
Frame rate	1000	1000
Sensor size	$14\mu m \times 14\mu m$	$10\mu m \times 10\mu m$
Output (bit)	8bit/10bit	8bit/24bit

$$\begin{bmatrix} \bar{x} \\ \bar{y} \end{bmatrix} = \begin{bmatrix} m_{10}/m_{00} \\ m_{01}/m_{00} \end{bmatrix} = \begin{bmatrix} \frac{\sum_x \sum_y xB(x,y)}{\sum_x \sum_y B(x,y)} \\ \frac{\sum_x \sum_y yB(x,y)}{\sum_x \sum_y B(x,y)} \end{bmatrix} \tag{2.9}$$

where, m_{00} represents the zeroth moment of the target, m_{10} and m_{01} represents the first moment about x-axis and y-axis respectively.

In order to implement the queue-linear flood fill algorithm for each target in every image frame, the seed point for growing should be detected first. Since high-speed frame rate is provided here (1000 fps), there will be little change among two continuous image frames, and it is reasonable to use the historical information based detection as shown in Figure 2.9. The whole image is divided into several search grids, with a sample point (refereed as global search point) for each grid. For the first image frame, it will be scanned in terms of global search until meet with the point within each of the target. After each target's center of mass has

Figure 2.7: High-speed camera EoSens MC1362 [4]

Figure 2.8: High-speed camera Photron IDP-Express R2000 [5]

been calculated, it is possible to implement the historical search method for the coming images.

2.2.3 Real-time computation system

In order to responds to the environment that changes dynamically through the feedback information of the sensors, it is necessary to implement the computations such as sensing, planning, servoing in terms of real-time. In our approach, we intend to realize the feedback loop system with a cycle time of 1 ms, it is rather important to adopt a control system that has a strong calculation capability as well as the variable interfaces to accommodate with the high-speed robots and sensors. We adopt the dSPACE flexible hardware systems, which are in widespread use in the automotive industry and are also employed in drives, aerospace, and industrial automation. The dSPACE system has high processor power, fast access to I/O hardware as well as variety of I/O interfaces. The adopted dSPACE system is of 1.0 GHz PowerPC-750GX, with 32ch 16bit-A/D inputs, 32ch 14bit-D/A inputs, 15ch encoder counter as well as 192ch digital I/O interfaces. The host computer (Intel Xeon: 2.33 GHz, memory: 3.0 GB) communicates with the dSPACE system through Ethernet, thus we can send experimental commands and

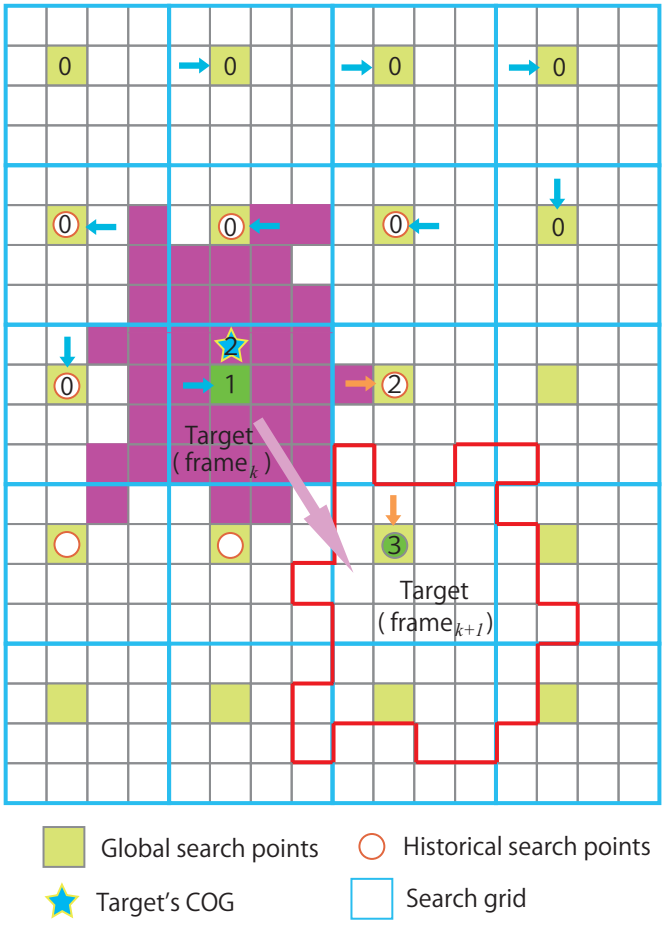

Figure 2.9: Image processing based on flood fill method

supervise the experimental results in real-time. Matlab Real-Time Workshop is adopted to develop the control software, and kinds of simulation applications can be incorporated within the experimental environment.

Based on all of the basic elements described above, the overall configuration of the experimental system is shown in Figure 2.10. As for the communication delay from sensing side (high-speed camera) to control side (dSPACE system), to our testing, it has been around 2 to 3 ms. Thus there is no need to worry about the issue that the communication delay will hinder the real-time feedback of the high-speed vision sensor.

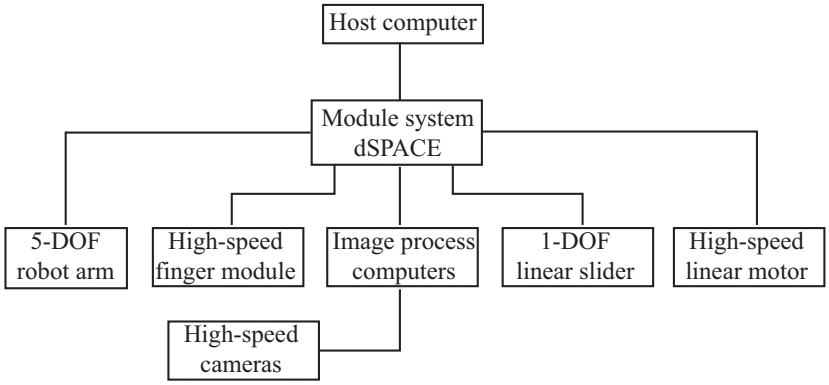

Figure 2.10: Overall configuration of experimental system

2.3 Experimental evaluations of the concept

Dynamic compensations for the high-speed robot arm under point-to-point regulation and vibration motion were studied [45]. The point-to-point regulation of a robot arm reflects its dynamic performance apparently, especially under rapid motions, while compensation for vibration motion has been conducted to check the compensation performance due to different working frequency. In order to simplify the quantitative analysis, only the vertical motion realized by one joint of the robot arm was conducted.

2.3.1 Compensation for point-to-point motion

The experimental setup of the 1-DOF prototype is shown in Figure 2.11. The compensation actuator was realized by one link of the high-speed finger [40]. Two light-reflecting markers, M_d represented the position controlled by robot arm and compensation actuator, while M_p referred to the position controlled only by the robot arm. The high-speed camera was configured as 720×720 pixels with a highest feedback rate of 1000 Hz.

Hereafter, the vertical component of $\boldsymbol{\xi}_d$: v_d, representing the dynamic performance under compensation, was compared with the vertical component of $\boldsymbol{\xi}_p$: v_p, representing the dynamic performance without compensation. Suppose the vertical component of target image position for M_d and M_p was v'_d and v'_p respectively (see Figure 2.11). For point-to-point regulation with compensation, firstly the robot arm was controlled to move from v_p to v'_p while the compensation actuator was kept motionlessly, and consequently it would be moved from v_d to v_{dp}. From v_{dp} to v'_d (assume within the motion range of the compensation actuator),

a simple PD control law was applied to the compensation actuator as

$$\tau = -K_v \cdot \dot{q} - K_p \cdot (v_d - v'_d) \tag{2.10}$$

where τ was the input torque for the actuator, K_v and K_p were positive-definite gain factors, $\dot{q}$ was the joint velocity.

As for the robot arm, since we only wanted to trace its dynamic performance, it was controlled to converge to the joint angle that recorded once it was moved to v'_p from v_p. Different visual feedback rate ranging from 80 fps to 1000 fps was examined to reveal the merits of high-speed visual feedback.

As shown in Figure 2.12, for simplification, suppose the target vertical position v'_d and v'_p had the same value 400, the real-time response of v_d and v_p represented the dynamic performance of the point-to-point regulation under compensation and without compensation respectively. It could be seen that the dynamic performance for the point-to-point regulation was improved greatly thanks to the dynamic compensation. It also shows that the visual feedback rate had a great effect on the quality of compensation. Within the limit of the compensation actuator's response speed, a higher visual feedback gave the better performance. For the case of 1000 Hz visual feedback, not only the settling time was reduced greatly (by setting the error band to be 15%, the settling time was reduced to t_{sc}= 73 ms from t_{so} = 221 ms), but also the vibration amplitude (overshoot) was compressed greatly.

2.3.2 Compensation for vibration motion

In the vibration compensation, the robot arm was controlled to follow a *sin(·)* pattern motion in the vertical direction. In order to realize compensation by the compensation actuator during the whole motion, the amplitude of the robot arm's motion was kept within the work range of the compensation actuator. Consequently, the robot arm was controlled by the following motion

$$q = \frac{\pi}{40} sin(2\pi f \sum_{i=1}^{n} \Delta t_i) \tag{2.11}$$

where q was the reference joint angle, f defined the frequency (the speed), and Δt_i = 1 ms was the control cycle time. The compensation actuator was controlled to keep M_d in the image position v'_d with the same PD control law as Equation (2.10) while it was affected by the robot arm's vibration motion (see Figure 2.11).

The robot arm was controlled to vibrate with a frequency ranging from 1 Hz to 6 Hz, and the compensation actuator was controlled with different visual feedback rate ranging from 80 fps to 1000 fps. The average image error was calculated for

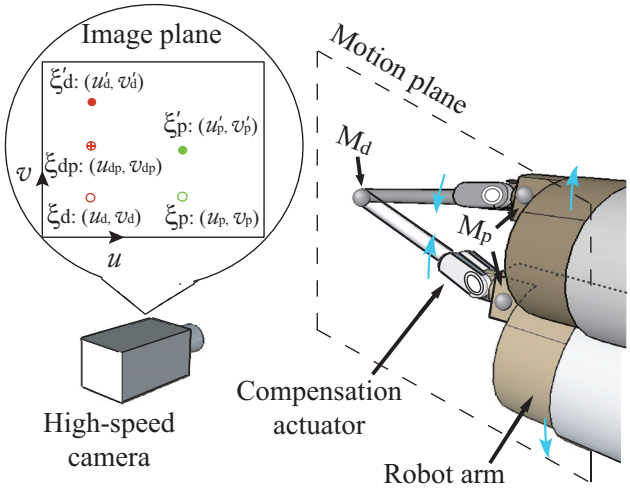

Figure 2.11: Experimental setup for dynamic compensation evaluation (with only vertical motion). The marker point M_d (with its image position $\boldsymbol{\xi}_d$) represents the check point under compensation, while marker point M_p (with its image position $\boldsymbol{\xi}_p$) represents the check point without compensation.

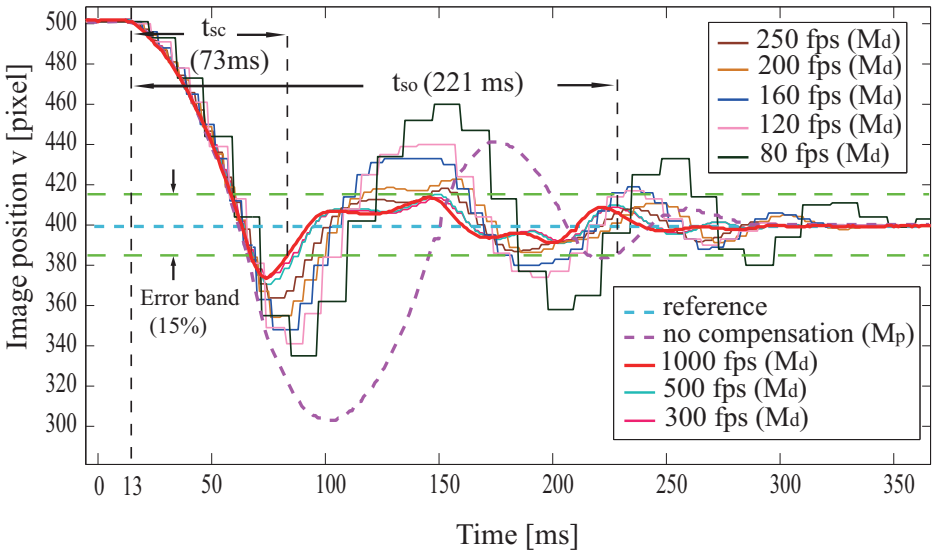

Figure 2.12: Comparison of the dynamic performances for point-to-point compensation.

Table 2.5: Comparison of the dynamic performances P_c (%) under different motion speed of robot arm and different visual feedback rate.

Speed of robot arm (Hz)	Visual feedback rate (fps)							
	80	120	160	200	250	300	500	1000
2	79.16	83.3	85.83	86.55	87.34	87.67	87.26	87.37
4	65.34	70.59	72.15	74.29	75.68	78.78	78.22	78.85
5	54.74	65.85	67.9	69.25	74.43	77.69	77.82	77.74
6	50.43	59.1	71.68	73.81	74.07	75.86	75.21	75.84

each trial, and then the compensation performance was evaluated by P_c as

$$P_c = [1 - \frac{\frac{1}{n}\sum(\mid v_d - v'_d \mid)}{\frac{1}{n}\sum(\mid v_p - v'_p \mid)}] \cdot 100\% \tag{2.12}$$

where n was the amount of sampled data. A larger P_c would represent the better compensation performance.

Figure 2.13 shows the comparison between the dynamic response of the check point with dynamic compensation and without compensation under the vibration motion of the robot arm with 6 Hz. Figure 2.14 shows the dynamic response of the check point with different motion speed of robot arm under the visual feedback rate of 500 fps. Both show that with the dynamic compensation the vibration was compressed greatly. Table 2.5 shows the compensation performance P_c with different moving speed of robot arm and different visual feedback rate for the compensation actuator. From Figure 2.13, Figure 2.14 and Table 2.5, we can see that although with the speeding up of the robot arm's motion speed, the compensation performance became poor, the degrading rate under a higher visual feedback rate was smaller than that under a lower visual feedback rate. For the same motion of the robot arm, a higher visual feedback rate gave a better compensation performance within a certain range, and here the boundary to the stable compensation was at about 300 fps.

Table 2.6 shows the quantitative analysis for the compensation with different motion speed of robot arm under a same visual feedback rate in accordance with Figure 2.14. It shows that with the speeding up of the robot arm, the amplitude of the check point became larger while no compensation was implemented. Really three quarters of the vibration was reduced and the average error after compensation was kept within a small range in the Cartesian space even for the fastest motion.

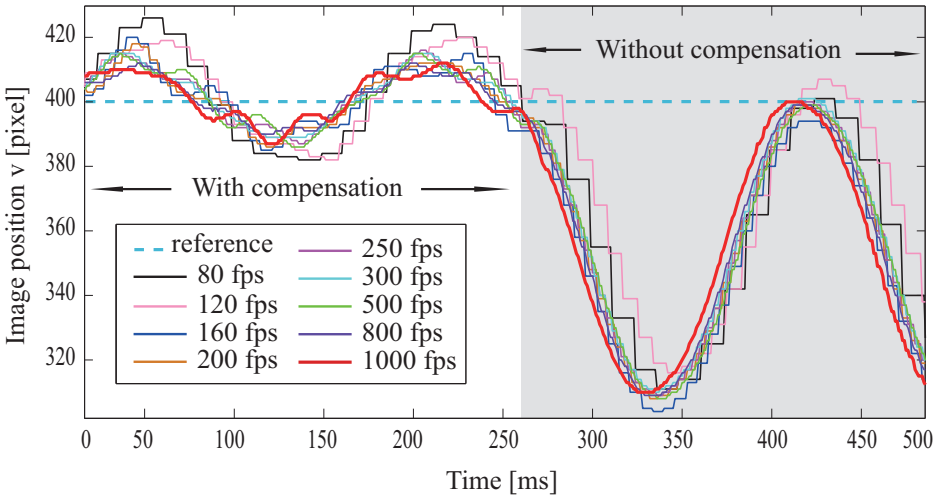

Figure 2.13: Comparison of the dynamic performances for vibration compensation.

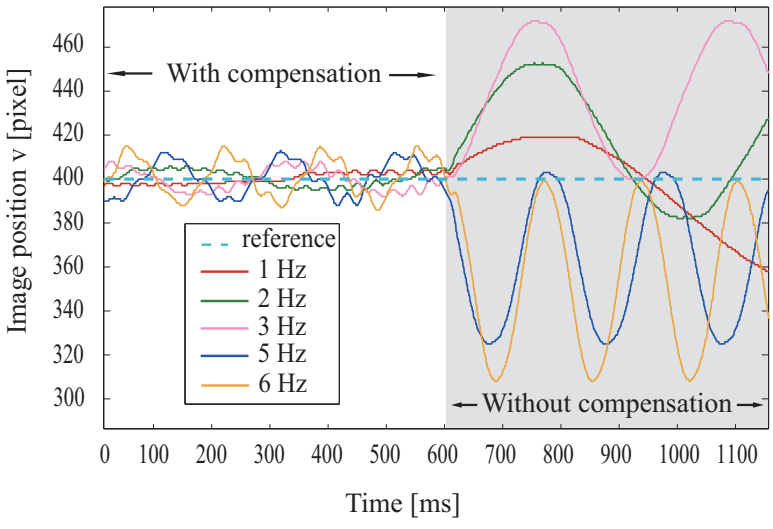

Figure 2.14: Comparison of the dynamic compensation for different speed of robot arm with a same visual feedback rate (500 fps) and the same amplitude.

Table 2.6: Compensation performance with different speed of robot arm.

Speed of robot arm (Hz)	Average error in image (pixel)	Average error in Cartesian (mm)	Amplitude without compensation (pixel)	P_c (%)
1	± 2.15	± 0.792	68	91.28
2	± 3.259	± 1.201	70	87.26
3	± 4.485	± 1.652	72	82.59
5	± 6.149	± 2.265	78	77.82
6	± 7.258	± 2.674	91	75.21

2.3.3 Discussion

From the experimental analysis of the dynamic compensation described above, the following conclusions can be drawn

1. With the high-speed dynamic compensation, the dynamic defects of robot arm can be improved greatly, and the dynamic coupling issue between robot arm and compensation actuator can be relieved;

2. Within the response limit of the compensation actuator, a higher visual feedback rate could result to a better compensation performance;

3. The bigger difference between the response order of robot arm and compensation actuator, the better compensation performance can be obtained.

As a matter of fact, based on the experimental analysis, we can give such a hypothesis as shown in Figure 2.15, and accordingly, in order to make full use of high-speed visual feedback or to further accelerate the moving speed of the robot arm, a compensation actuator with much higher response speed can obtain better dynamic performance.

The same analysis can be applied for the case with more DOFs (or saying dynamic compensation of a robot arm in more than one dimension), as long as the compensation actuator has enough DOFs for compensating different direction's motion.

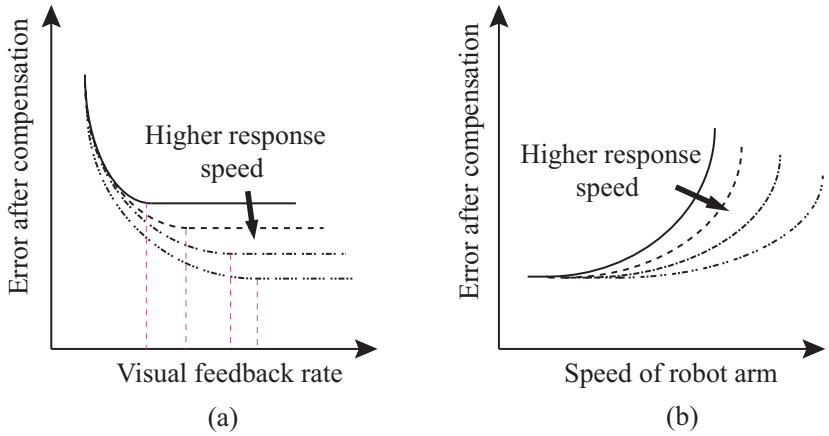

Figure 2.15: Hypothesis of the compensation performance respected to the compensation actuator's response speed. For (a), suppose the robot arm's motion speed is constant. For (b), suppose the visual feedback rate is constant.

2.4 Extensibility of the proposed concept

Since the proposed dynamic compensation concept is independent on the system's dynamics, it is reasonable to extend this concept into multiple dimensions to realize a much complex DCRS rather than 1-DOF. For instance, in order to form a 3-DOF DCRS for positioning, we basically assemble it by three 1-DOF DCRSs, and the same control method (whether simple or sophisticated) can be applied in each dimension.

2.5 Summary of this chapter

In this chapter, the dynamic compensation concept as well as the resulted dynamic compensation robotic system (DCRS) have been introduced with quantitative experimental evaluations. The methodology of the proposed concept is that: the high-speed vision sensing in terms of task-space can inspect the uncertain target as well as the dynamic uncertainties brought by the main robot (the main plant) under high-speed motions, and by the compensation actuator (the compensation plant), which is capable of high-speed response, the uncertainties can be compensated based on the relative coordinate visual information between target, main plant and compensation plant.

Experimental systems including robots, vision systems as well as computation systems have been also addressed. Evaluations based on the 1-DOF prototype have been conducted and the merits of the proposed dynamic compensation con-

cept such as independence of system models, good flexibility as well as compensation capability under high-speed motion have been revealed. Through the evaluations, the high-speed visual feedback rate and the high-speed response order of the lightweight compensation actuator have shown great effect on the compensation results. If we look back at the Figure 1.5 and 1.6 that have been illustrated as the motivation of this research, basically the proposed dynamic compensation concept has shown the good performance or the potential capability in the expected properties of robotic interactive manipulations.

Since the evaluations have been conducted with the simple PD control, there may be a much better compensation performance by developing some sophisticated control algorithms, and this issue will be addressed in the next chapter.

Chapter 3

Improved algorithms based on relative coordinate high-speed visual feedback

As has been described in the last chapter, the high-speed visual feedback based on relative coordinate is one important aspect in the proposed dynamic compensation concept. In this Chapter, we want to introduce some improved visual servo algorithms based on the relative coordinate high-speed visual feedback. These algorithms have been developed with such objectives: robust to coarse kinematics, less camera calibration, system dynamics independent and easy implementation under the case of high-speed position regulation. Generally speaking, the main robot in our DCRS mostly refers to the serial industrial robot arm, which has been widely adopted in manufacturing. A simplified IBVS approach for robot arm, which is depth-independent and easy for implementation, will be introduced in section 3.1. Concerning with the better compensation performance by the compensation actuator, a pre-compensated PD control approach will be addressed in section 3.2. Simulation and experimental evaluations will show the effectiveness of these algorithms.

3.1 Simplified IBVS approach for robot arm

As described in section 1.1.1, from the perspective of feedback hierarchy, vision-based robotic control can be categorized into two main types : the *dynamic look-and-move* and *direct visual servo* approach, and the later one is supposed to have better performance in dealing with non-linear dynamic forces while performing high-speed manipulations with sufficiently high visual feedback frequency. Traditionally, due to the low sampling rate of the vision sensor, few systems have

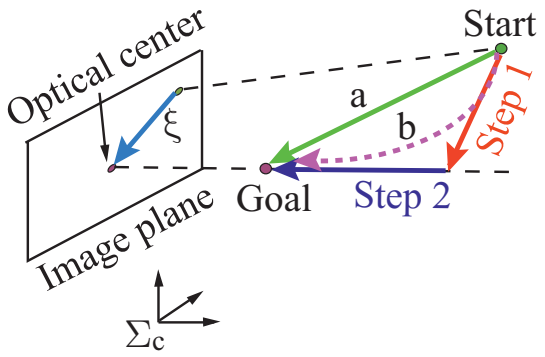

Figure 3.1: Image based position regulation (a represents the optimal trajectory, and b represents the non-optimal trajectory under the two-step method).

adopted the direct visual servo approach [8, 9, 46, 47]. However, with the developing of the hardware system, the visual feedback frequency already reached 1 kHz several years ago [1], and it is no longer difficult to employ a high-speed vision sensor for ordinary applications. With the high-speed visual feedback, we propose a simplified IBVS approach that is suitable for the DCRS. Note that in this research, we have mainly focused on the eye-in-hand configuration of the camera relating to the IBVS approach.

3.1.1 IBVS approach

For the position regulation of one feature point based on the IBVS approach, the classical IBVS approach has been greatly dependent on the optical-motion model. As shown in Figure 3.1, the accurate optical-motion model provides the optimal solution to regulate the point from the start position to the goal position, as it will follow the line trajectory a in Cartesian. However, the accurate optical-motion model is always difficult to obtain.

Suppose that an arbitrary point $Pi \in \mathbb{R}^3$ with camera coordinates $[x, y, z]$ projects onto the image plane at the image position $\boldsymbol{\xi} \in \mathbb{Z}^2$: (u, v), and let $\dot{\boldsymbol{r}} = [T_x, T_y, T_z, \omega_x, \omega_y, \omega_z]^T$ represents the velocity screw of the camera coordinates (along with the end-effector). Then, we have the classical formulation [8]:

$$\begin{bmatrix} \dot{u} \\ \dot{v} \end{bmatrix} = \boldsymbol{J}_{img} \cdot \dot{\boldsymbol{r}} \tag{3.1}$$

$$\boldsymbol{J}_{img} = \begin{bmatrix} -\frac{f}{z} & 0 & \frac{u}{z} & \frac{uv}{f} & -\frac{(f^2+u^2)}{f} & v \\ 0 & -\frac{f}{z} & \frac{v}{z} & \frac{f^2+v^2}{f} & -\frac{uv}{f} & -u \end{bmatrix}, \tag{3.2}$$

where the interaction matrix $\boldsymbol{J}_{img}$ is dependent on the current feature value $\boldsymbol{\xi}$ and the depth information z, f is the focal length. Note that the depth z cannot be obtained directly. From the kinematics of the robot, we have

$$\dot{\boldsymbol{r}} = \boldsymbol{J}_r \cdot \dot{\boldsymbol{\theta}} \tag{3.3}$$

where $\dot{\boldsymbol{\theta}}$ is the vector of the joint velocities. With Equation 3.2 and 3.3, we can get the optical-motion model of the classical IBVS approach as

$$\dot{\boldsymbol{\xi}} = \boldsymbol{J}_{img} \cdot \boldsymbol{J}_r \cdot \dot{\boldsymbol{\theta}} \tag{3.4}$$

In order to realize the optimal trajectory regulation as shown in Figure 3.1, it is necessary to calculate the depth z on-line for $\boldsymbol{J}_{img}$ and the kinematic Jacobian $\boldsymbol{J}_r$ in real-time. Several methods adopted the depth estimation approach [48] to roughly build the interaction matrix $\boldsymbol{J}_{img}$.

As a matter of fact, $\boldsymbol{J}_{img}$ can be divided into the translation component $\boldsymbol{J}^t_{img}$ and the rotation component $\boldsymbol{J}^r_{img}$ [49] as follows:

$$\boldsymbol{J}^t_{img} = \begin{bmatrix} -\frac{f}{z} & 0 & \frac{u}{z} \\ 0 & -\frac{f}{z} & \frac{v}{z} \end{bmatrix}, \boldsymbol{J}^r_{img} = \begin{bmatrix} \frac{uv}{f} & -\frac{(f^2+u^2)}{f} & v \\ \frac{f^2+v^2}{f} & -\frac{uv}{f} & -u \end{bmatrix}$$

It is obvious that the translation part $\boldsymbol{J}^t_{img}$ is dependent on the current image feature and the depth information, whereas the rotation part $\boldsymbol{J}^r_{img}$ has no relationship with the depth information. On basis of this property, several partitioned approaches have been proposed [49, 50, 51, 52]. Partitioning the degrees of freedom offers some advantages for these methods: they can reach global convergence, and they do not need to perform depth estimation as a separate task for realizing the interaction matrix [49, 50]. Malis *et al.* [50] developed so-called 2-1/2-D visual servoing by incorporating information of the homography matrix into the control law. This achieved global stability, and in addition, depth information for the interaction matrix could be obtained while solving the homography matrix. Deguchi [49] also adopted the homography matrix solving method to realize partitioned control of translation and rotation motions. However, because these methods need a homography transformation calculation, they have the drawbacks that the calculation is complex and they are not robust to noise [50, 52]. Corke and Hutchinson [51] proposed a partitioned approach by decoupling the translation and rotation components towards the optical axis from the interaction matrix, with the aim of tackling the *camera retreat* problem. In addition, several depth-independent approaches have also been proposed [46, 47]. Wang *et al.* [47] adopted a depth-independent interaction matrix with point and line features to

linearly parameterize the interaction matrix, as well as the closed-loop dynamics of the system.

As for the other aspect of the optical-motion model: the kinematic Jacobian $\boldsymbol{J}_r$, usually it is calculated by calibrating the kinematic parameters. Besides, there is another on-line Jacobian estimation approach that needs no calibration of the system kinematics. In [53], a modified discrete-time Jacobian estimator and a Jacobian estimator based on extended least squares algorithm was proposed. In [54], the same on-line Jacobian estimation method was adopted to realize the 3D ball catching task. In [55], an estimation method based on fuzzy adaptive kalman filtering was proposed. Besides, Broyden's method [56] as well as dynamic quasi-Newton method with a recursive least squares (RLS) [57] estimation method have been proposed.

Here in this research for the optical-model, we shall mainly focus on two issues: one is to avoid the estimation of the depth information, the other is to decouple the relation between T_x and T_z, as well as between T_y and T_z within the velocity vector $\dot{\boldsymbol{r}} = [T_x, T_y, T_z, \omega_x, \omega_y, \omega_z]^T$ as the coupling is raised due to the third column of $\boldsymbol{J}^t_{img}$. A bad estimation of the depth z with the coupling issue may result in bad dynamic performance, especially under noisy estimation of image features $\boldsymbol{\xi}$. Therefore, we want to improve the classical optical-motion model to realize a depth-independent approach in which T_x and T_z are decoupled and T_y and T_z are decoupled. Since these two issues involve only the translation component of the interaction matrix, in this study we only focus on translational control and ignore pose control.

3.1.2 Simplified IBVS

In the following contents, we propose a direct visual servoing scheme based on a simplified interaction matrix [58]. The motivation for simplifying the traditional IBVS approach is not only for easy calculation to enable a high-speed visual servoing, but also for easy implementation by adopting a coarse as well as depth-independent interaction matrix, especially the absolute depth is difficult to obtain. Note that for the kinematic Jacobian $\boldsymbol{J}_r$, we will adopt the calibration approach rather than on-line estimation, as it is too complex to calculate and may be unstable.

3.1.2.1 Convergence issue

In this section, we will try to analyze the problem such as whether the regulation can still realize convergence if there are some uncertainties involved for the interaction relationship brought by the simplification. The analysis will basically follow the same method as illustrated in section 2.1. Suppose the uncertainty for

the interaction matrix is $-\boldsymbol{J}_{img}^{e}$, then we have

$$\begin{aligned}\dot{\boldsymbol{\xi}}_r^{'} &= \boldsymbol{J}_{img} \cdot \boldsymbol{J}_r \cdot \dot{\boldsymbol{\theta}} - \boldsymbol{J}_{img}^{e} \cdot \boldsymbol{J}_r \cdot \dot{\boldsymbol{\theta}} \\ &= \boldsymbol{J}_{img} \cdot \boldsymbol{J}_r \cdot \dot{\boldsymbol{\theta}} - \boldsymbol{\delta}_{img} = \dot{\boldsymbol{\xi}}_r - \boldsymbol{\delta}_{img}\end{aligned} \tag{3.5}$$

where $\boldsymbol{J}_{img}^{e} \cdot \boldsymbol{J}_r \cdot \dot{\boldsymbol{\theta}}$ is replaced by the notation $\boldsymbol{\delta}_{img}$.

The regulation error at time of k is

$$\begin{aligned}\boldsymbol{E}^k &= \boldsymbol{\xi}_r^k + (\boldsymbol{\delta}^k - \boldsymbol{\delta}_{img}^k) - \boldsymbol{\xi}_T \\ &= \boldsymbol{\xi}_r^k + \boldsymbol{\Delta}^k - \boldsymbol{\xi}_T\end{aligned} \tag{3.6}$$

where we have replaced $\boldsymbol{\delta}^k - \boldsymbol{\delta}_{img}^k$ by the notation $\boldsymbol{\Delta}^k$.

Hereafter, we will conduct the same analysis for the compensation as

$$\boldsymbol{E}^{k+1} = \boldsymbol{\xi}_r^{k+1} + \boldsymbol{\Delta}^{k+1} + \boldsymbol{\xi}_c^{k+1} - \boldsymbol{\xi}_T \tag{3.7}$$

With the estimation for the compensation part to be

$$\boldsymbol{\xi}_c^{k+1} = -\widehat{\boldsymbol{E}}^k \Rightarrow -\widehat{\boldsymbol{\Delta}}^k \tag{3.8}$$

And the approximation to be

$$\widehat{\boldsymbol{\Delta}}^k \doteq \boldsymbol{\Delta}^{k+1} \tag{3.9}$$

Then we can see that the regulation can still realize convergence as

$$\boldsymbol{E}^{k+1} = \boldsymbol{\xi}_r^{k+1} - \boldsymbol{\xi}_T \Rightarrow 0 \tag{3.10}$$

As the analysis described above, the uncertainties brought by the simplification of the interaction relationship will not affect the convergence of the regulation. As a matter of fact, the same analysis above can also be applied to the case where the robot's kinematic model has some uncertainties, as the resulted uncertainties will also be compensated by the compensation actuator based on the high-speed visual feedback of the relative information between the two plants and target. It means that the proposed dynamic compensation concept fits for the coarse kinematics of the robot manipulator, thus we can still apply the simplified IBVS approach addressed later even there is no accurate kinematic model for the main robot.

3.1.2.2 Methodology

Considering to regulate Pi's image position to be in the center of the image plane with the desired relative distance between the target position and camera in Cartesian. Let $\dot{D}_{dep}$ be the rates of change of the image feature due to the translation motion along the optical axis. This image feature could be set to be the square root of the image area for the regulating target [51], and a linear relation: $\dot{D}_{dep} = \gamma \cdot T_z$ (as we have adopted) or a nonlinear relation: $\dot{D}_{dep} = \gamma \cdot e^{T_z}$ [52] could be assigned (γ is the scalar gain coefficient). With the camera's focal length f, the interaction relationship could be inherited from the traditional IBVS as:

$$\begin{bmatrix} \dot{u} \\ \dot{v} \\ \dot{D}_{dep} \end{bmatrix} = \begin{bmatrix} f/z & 0 & -u/z \\ 0 & f/z & -v/z \\ 0 & 0 & \gamma \end{bmatrix} \begin{bmatrix} T_x \\ T_y \\ T_z \end{bmatrix} \tag{3.11}$$

Suppose this regulation is realized with a two-step method as shown in Figure 3.1: firstly to center Pi while maintaining the initial depth; then to regulate the depth to be the desired value. Let the velocity vectors for these two steps be: $[T_{x1}, T_{y1}, T_{z1}]^T$ and $[T_{x2}, T_{y2}, T_{z2}]^T$ respectively, with $T_{z1} = 0$, $T_{x2} = 0, T_{y2} = 0$. Then we will have:

$$\begin{bmatrix} \dot{u} \\ \dot{v} \\ \dot{D}_{dep} \end{bmatrix} = \begin{cases} \begin{bmatrix} \frac{f}{z} & 0 & -\frac{u}{z} \\ 0 & \frac{f}{z} & -\frac{v}{z} \\ 0 & 0 & \gamma \end{bmatrix} \begin{bmatrix} T_{x1} \\ T_{y1} \\ T_{z1} \end{bmatrix} & (step1) \\ \begin{bmatrix} \frac{f}{z} & 0 & -\frac{u}{z} \\ 0 & \frac{f}{z} & -\frac{v}{z} \\ 0 & 0 & \gamma \end{bmatrix} \begin{bmatrix} T_{x2} \\ T_{y2} \\ T_{z2} \end{bmatrix} & (step2) \end{cases} \tag{3.12}$$

Since $T_{z1} = 0$, $T_{x2} = 0, T_{y2} = 0$ is defined under the two-step method in default, and in the second step, the image coordinates $(\dot{u}, \dot{v})$ would be $(0, 0)$ as the target has been regulated to be in the image center, then we can change the interaction relationship to be an equivalent form:

$$\begin{bmatrix} \dot{u} \\ \dot{v} \\ \dot{D}_{dep} \end{bmatrix} = \begin{cases} G_1 \begin{bmatrix} \frac{1}{z} & 0 & 0 \\ 0 & \frac{1}{z} & 0 \\ 0 & 0 & \frac{1}{z} \end{bmatrix} \begin{bmatrix} T_{x1} \\ T_{y1} \\ T_{z1} \end{bmatrix} & (step1) \\ G_2 \begin{bmatrix} \gamma & 0 & 0 \\ 0 & \gamma & 0 \\ 0 & 0 & \gamma \end{bmatrix} \begin{bmatrix} T_{x2} \\ T_{y2} \\ T_{z2} \end{bmatrix} & (step2) \end{cases} \tag{3.13}$$

where G_1, G_2 are constant gain coefficient matrices.

With high-speed cameras, it is reasonable to think that this two-step regulation is equivalent to such a situation, that the centering regulation has the priority over the depth regulation, and this could be achieved by choosing large gain coefficients for centering regulation and relatively small gain factors for depth regulation. The control formulation (the inverted form of the interaction relationship) could be chosen as:

$$\begin{bmatrix} T_x \\ T_y \\ T_z \end{bmatrix} = C \begin{bmatrix} k_u & 0 & 0 \\ 0 & k_v & 0 \\ 0 & 0 & k_d \end{bmatrix} \begin{bmatrix} \dot{u} \\ \dot{v} \\ \dot{D}_{dep} \end{bmatrix} \tag{3.14}$$

where $k_u = e^{|u/u^*-1|}$, $k_v = e^{|v/v^*-1|}$, $k_d = e^{-(k_u^2 \cdot k_v^2)}$ with the current image coordinates $\boldsymbol{\xi} = (u, v)$ and the goal $\boldsymbol{\xi}_{ref} = (u^*, v^*)$, C is the constant gain coefficient matrix including the scale function as the camera's focal length f. Equation (3.14) shows a depth-independent and decoupled property, and the priority of centering is maintained due to the elements of the interaction matrix (as shown in Fig. 3.2, the element corresponding to the depth regulation k_d becomes larger, starting from zero, as the image position moves to the center). As a matter of fact, we can go further by simply making the priority adjusting factors to be constant values such as: $k_1 = k_2 >> k_3$. Then we would have:

$$\begin{bmatrix} T_x \\ T_y \\ T_z \end{bmatrix} = C \begin{bmatrix} k_1 & 0 & 0 \\ 0 & k_2 & 0 \\ 0 & 0 & k_3 \end{bmatrix} \begin{bmatrix} \dot{u} \\ \dot{v} \\ \dot{D}_{dep} \end{bmatrix} \tag{3.15}$$

Now, the interaction relation has been approximated to be a linearized form. Both Equation (3.14) and Equation (3.15) approaches hold such merits as: free of inverse calculation, depth independent and motion decoupled. Through simulation conducted later, we will see that with the motion decoupling, the simplified approach could have better dynamic performance than the traditional approach, especially under noisy estimation of image features or with the camera's parameters uncalibrated. Besides, we can simply suppress the depth regulation while the target is at the edges of the image plane to keep the visibility of the target for the eye-in-hand camera.

The analysis above is based on the regulation of centering the one target point with translation control. As a matter of fact, for a general case of image-based set point position regulation, we can also apply this simplified approach as long as we keep the priority of the 2D image plane regulation over the depth regulation, and we will show this in the simulation later by regulating the target point to a goal position that is not the image center. On the other hand, the simplified approach

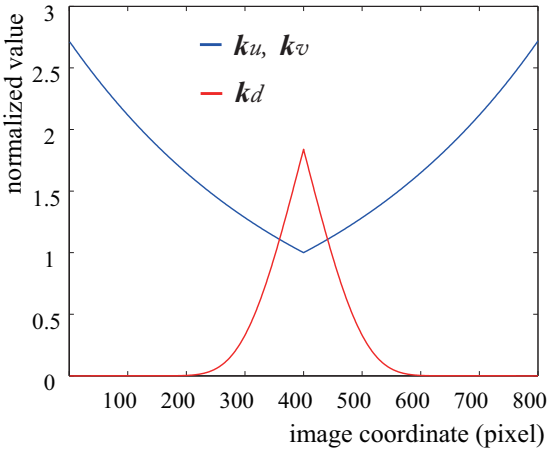

Figure 3.2: Cross-sectional view (u=v) of the variation of the inverse interaction matrix elements (image center [400,400]).

is nothing more than a simple trajectory planning method for one target point's regulation under high-speed visual feedback, and the regulation trajectory may hardly be the optimal solution (as shown in Figure 3.1 and Figure 3.4). We adopt it as the trade-off between the easy calculation as well as easy implementation for the high-speed regulation and the optimal control. Moreover, it is difficult to accurately estimate depth with one camera without good calibration. Equation (3.14) and (3.15) give two alternatives with different simplifying levels. For convenience, we will refer to Equation (3.14) as the half simplified (HS) method and Equation (3.15) as the full simplified (FS) method. We will examine the performance of these two methods in comparison with the conventional method through simulations.

Note that the control for keeping the image features within the camera field of view becomes much easier with FS. Since the depth regulation is the only cause of the lose of image features, we can simply suppress the depth regulation if the image features reach the edges of the image plane.

We built a direct visual servo controller based on the HS and FS methods. Since there is a singularity problem originating from the kinematics of the robot arm, we adopt the damped least squares (DLS) [59] technique to realize a singularity-robust inverse (SRI). DLS involves a compromise between accuracy and feasibility of the inverse kinematic solution. Let $\boldsymbol{J}_r$ and $\boldsymbol{J}_{int}$ be the kinematic Jacobian matrix and the simplified interaction matrix, respectively, and let $\boldsymbol{J}_t = \boldsymbol{J}_{int}\boldsymbol{J}_r$ be the overall Jacobian. For joints $\boldsymbol{q}$, the DLS gives

$$\begin{aligned} \boldsymbol{J}^* &= (\boldsymbol{J}_t)^T(\boldsymbol{J}_t(\boldsymbol{J}_t)^T + \alpha I)^{-1} \\ \dot{\boldsymbol{q}} &= \boldsymbol{J}^* \cdot [\boldsymbol{err}^{\xi}, err^d]^T, \end{aligned} \tag{3.16}$$

where α is the damping factor, and $\boldsymbol{err}^{\xi}$ and err^{d} are the image feature errors for the image plane position and the depth, respectively.

The control laws for the HS and FS methods are

$$\boldsymbol{\tau} = k_p \cdot \boldsymbol{J}(\boldsymbol{q}, \boldsymbol{\xi})^* \cdot [\boldsymbol{err}^{\xi}, err^{d}]^T - k_d \cdot \dot{\boldsymbol{q}} + \boldsymbol{g}(\boldsymbol{q}) \tag{3.17}$$

$$\boldsymbol{\tau} = k_p \cdot \boldsymbol{J}(\boldsymbol{q})^* \cdot [\boldsymbol{err}^{\xi}, err^{d}]^T - k_d \cdot \dot{\boldsymbol{q}} + \boldsymbol{g}(\boldsymbol{q}), \tag{3.18}$$

where $\boldsymbol{\tau}$ is the torque added to each joint, k_p and k_d are two gain coefficient matrices, and $\boldsymbol{g}(\boldsymbol{q})$ is the gravity compensation vector.

3.1.2.3 Simulation study

Simulations were conducted with the Robotics Toolbox and Machine Vision Toolbox [60]. We compared the conventional method, the HS method, and the FS method using the same conditions.

A six-joint PUMA560 robot was modeled, and the initial joint angles were set to be [0, -pi/4, pi/4, 0, 0, 0]. The image plane was projected by a simulated Pulnix camera with focal length $f = 0.0078$ m, and image center $(u, v) = (274, 210)$. The image range was set to be (0–548, 0–420). We chose a static target point with the initial image position (452, 373) to be regulated to the goal position (120, 140) (*note that this is not the center of the image plane*), and the relative distance between the target point and the camera was initialized to be 0.7 m. These parameters basically were chosen randomly within the robot arm's workspace. However, for better understanding and to give more convincing results, we chose the initial and goal coordinates of the target point so as to be slightly far away from each other. For each method, we chose the gain coefficients that allowed the robot to reach the convergence point quickly with stable and smooth movement. In order to examine the performance of the three methods with different depth regulations, two settings were defined: small regulation with the goal depth set to be 0.5 m, and large regulation with the goal depth set to be 0.2 m. For both settings, four rounds of simulation with the same conditions were carried out for the three methods. As for the noise added to both the image position and the depth estimation, we added two zero-mean Gaussian random variables ranging from -2.5 to 2.5 pixels for u and v, respectively, and a zero-mean Gaussian random variable ranging from -0.05 to 0.05 m for the depth information. For judging convergence, we set accuracies of $\pm$ 3 pixels and $\pm$ 0.005 m for the image position error and depth error, respectively.

We used a parameter called *sum of feature distance* (SFD) to evaluate the global concentration during the convergence process. The SFD is calculated as: $\sum (\mid \boldsymbol{err}^{\xi} \mid + \mid err^{d} \mid)$. Convergence iterations and SFD were compared for the two settings, as shown in Table 3.1 and Table 3.2.

Table 3.1: Comparison results with small depth regulation.

Simulation round		Traditional Method	HS Method	FS Method
1	*iteration*	50	176	59
	SFD	4.4697e+003	2.1655e+003	2.1510e+003
2	*iteration*	342	46	52
	SFD	6.0408e+003	1.4112e+003	2.2360e+003
3	*iteration*	107	39	97
	SFD	4.6377e+003	1.4292e+003	2.6390e+003
4	*iteration*	112	43	74
	SFD	5.1475e+003	1.2532e+003	2.2772e+003
ave.	*iteration*	152.7	76	70.5
	SFD	5.0740e+003	1.5647e+003	2.3258e+003

Table 3.2: Comparison results with large depth regulation.

Simulation round		Traditional Method	HS Method	FS Method
1	*iteration*	205	44	33
	SFD	1.5637e+004	1.7710e+003	1.8066e+003
2	*iteration*	384	97	89
	SFD	1.7449e+004	1.9504e+003	2.5003e+003
3	*iteration*	408	145	223
	SFD	1.7530e+004	1.9912e+003	3.1532e+003
4	*iteration*	200	212	31
	SFD	1.6239e+004	2.2913e+003	1.8507e+003
ave.	*iteration*	299.2	124.5	94
	SFD	1.6714e+004	2.0001e+003	2.3276e+003

Both the HS and FS methods had a smaller SFD than the traditional method in the two regulations, which shows that they had better performance in global concentration during the convergence process. On average, the traditional method needed more iterations for convergence, especially with large depth regulation, as shown in Table 3.2.

Fig. 3.3 shows the contrast performance of the three methods for large depth regulation (goal depth: 0.2 m). From the velocity vector, we could see that T_x and T_y in the HS and FS methods had large values at the start of regulation and then varied slightly around zero due to the depth regulation. In contrast, with the traditional method, T_x and T_y started with small values and then varied greatly. We think this was the reason for its larger SFD value, and has been resulted from the coupling between T_x and T_z as well as the coupling between T_y and T_z in the interaction matrix. With the HS method, the feature point moved to the goal

position very quickly right at the start of regulation, and T_z kept a small value at the start, whereas T_y showed an overshoot. Comparing the HS and FS methods, HS showed a small SFD value, whereas FS had a relatively stable convergence speed for the two regulations. Considering all of these issues, we adopted the FS method in the experiments for ball tracking described in the following section 3.1.2.4.

As a summary, the proposed simplified approach has the following properties:

- There is no need to estimate the depth information in building the interaction relation;
- It is easy for calculation of the inverse matrix, since the simplified "interaction matrix" is a diagonal matrix;
- The motion between T_x and T_z, as well as the motion between T_y and T_z in the velocity screw realize decoupling;
- It is based on the high-speed visual feedback and fits for high-speed regulation for its simple calculation (it has much faster convergence speed than the classic IBVS model-based approach);
- As shown in Figure 3.4, the regulation trajectory for simplified approach can hardly be the optimal one, yet it has a better dynamic performance during the convergence process than the classic IBVS model-based approach under noisy estimation of image features or depth as shown in simulation (the classic IBVS model-based approach has a much bigger SFD). Although in the ideal case, the classic IBVS model-based approach is supposed to follow the optimal trajectory in most of the time, it is easily affected by the estimation noise due to its depth-dependent feature and the coupling issue within the optical-motion model.

3.1.2.4 High-speed tracking experiment

Experimental Setup

We adopted the high-speed robot arm and one Eosens vision system (refer to section 2.2) with an image resolution of 800×800 and a sampling rate of 1000 fps. A ball with a diameter of 0.05 m was used for tracking. The robot was controlled to keep the ball's geometric center in the center of the image with a constant distance between the ball and the camera.

When the robot reached the ready position, we moved the ball manually to follow a circle-like trajectory with a radius of about 0.3 m, and we also tried to

change the distance between the ball and the camera. First, we moved the ball with a moderate speed (about 0.8 rad/s), and then much faster (about 2.2 rad/s).

In order to prevent a sudden impact at the beginning of tracking (resulting from the large image error when the target was first moved into the field of view), we set a damping factor β ($0 < \beta \leq 1$) in the controller to avoid a starting shock. We gradually increased β to 1 as the target moved to the center of the image:

$$\beta = \begin{cases} 1(if \mid merr^{\xi} \mid \leq S) \\ 1/(\mid merr^{\xi} \mid -S)(if \mid merr^{\xi} \mid > S) \end{cases} \tag{3.19}$$

where $\mid merr^{\xi} \mid = max(\mid err^{u} \mid, \mid err^{v} \mid)$, and S is the threshold. Then, the control law for FS can be written as

$$\boldsymbol{\tau} = k_p \cdot \beta \cdot \boldsymbol{J(q)}^{*} \cdot [\boldsymbol{err}^{\xi}, err^{d}]^{T} - k_d \cdot \dot{\boldsymbol{q}} + \boldsymbol{g(q)}. \tag{3.20}$$

Experimental Result

The tracking was controlled to start at 5 s and end at 15 s. Fig. 3.6 shows the process of ball tracking. With the high-speed visual servoing, the robot moved the end-effector rapidly while attempting to keep the target in the center of the image.

Fig. 3.5 shows the time response of image features of the target and the robot arm's joints while tracking. Fig. 3.5 (a) and (b) show the u and v coordinate responses, respectively, and (c) shows dynamic regulation of the depth. From 5 s to 8 s, the gain factor β reduced the image error, and the camera moved gradually to place the target in the center of the image. From 8 to 15 s, the robot quickly tracked the moving ball in terms of position and distance.

Also, the image features of the target showed obvious oscillation during the reciprocating motion, and did not ideally keep in a line. This may have been partially due to the robot arm's dynamics and the fact that we moved the ball outside of the workspace of the robot arm, and the robot could not reach the goal position as we moved the ball too far away.

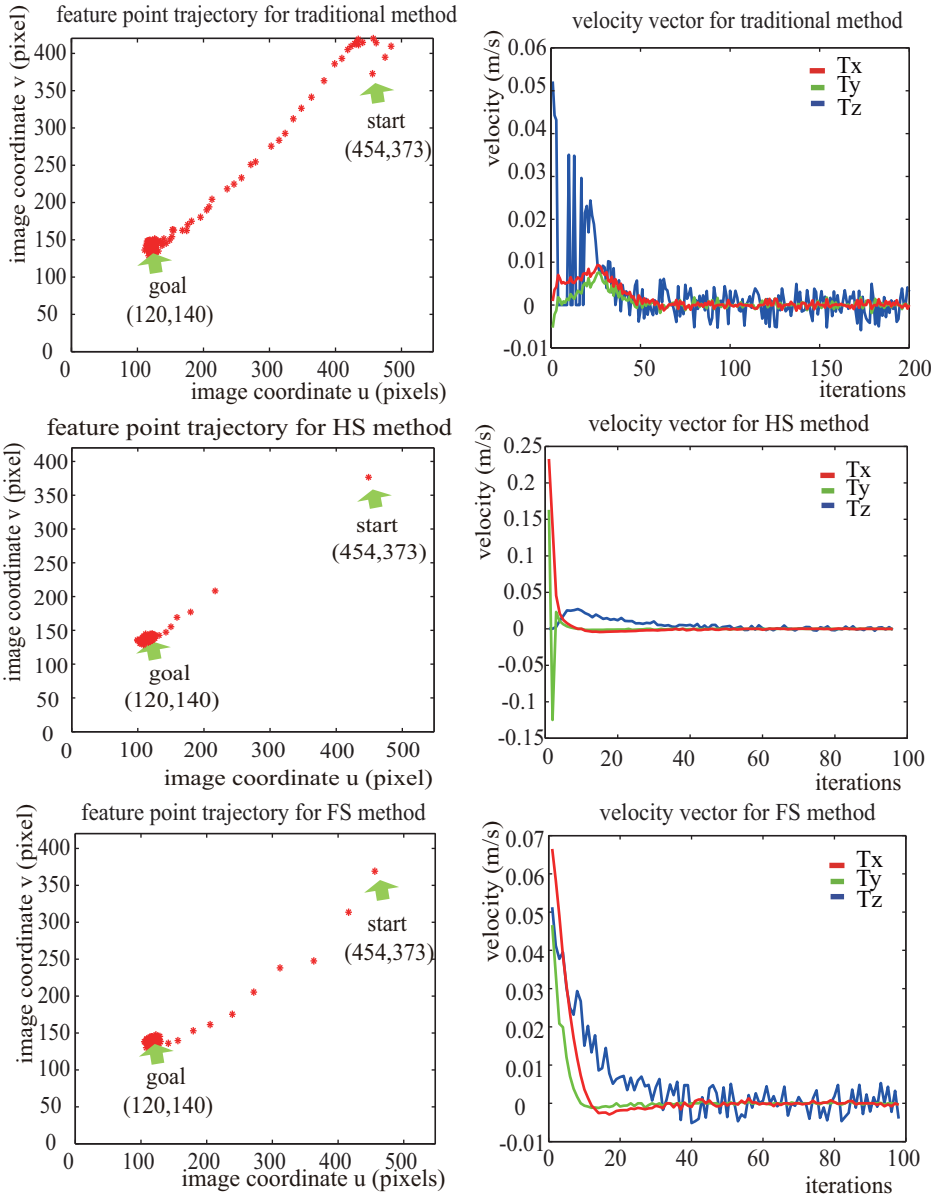

Figure 3.3: Contrast performance of three methods for large depth regulation.

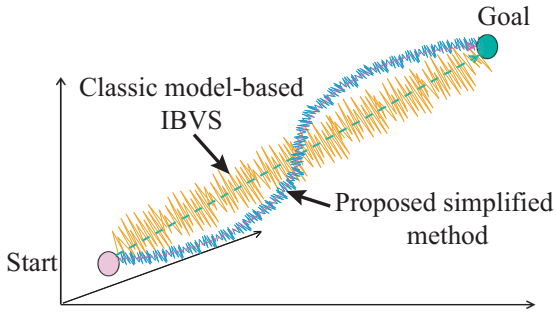

Figure 3.4: Possible trajectories for classical IBVS approach and simplified approach in set-point regulation.

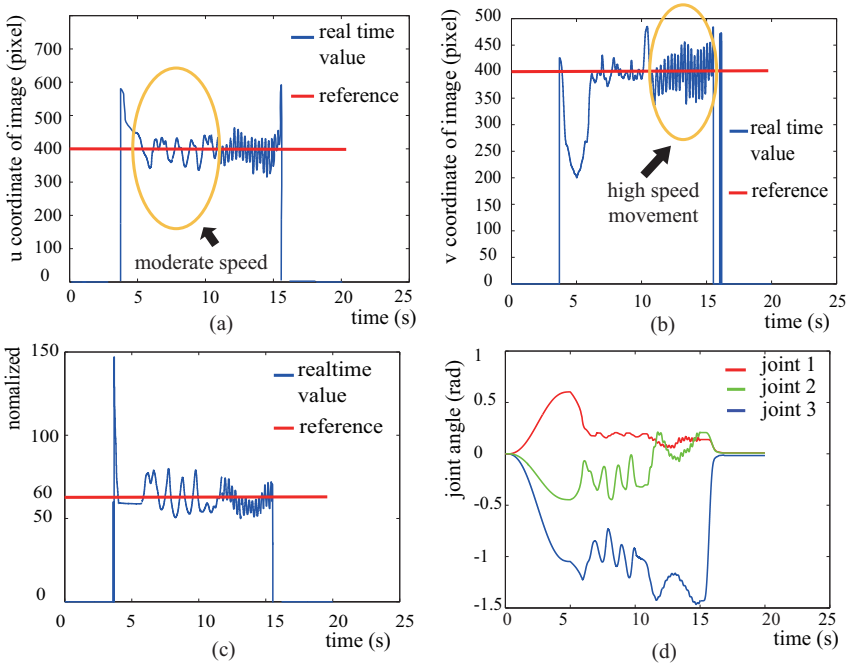

Figure 3.5: Time response of joint angle and image features of target

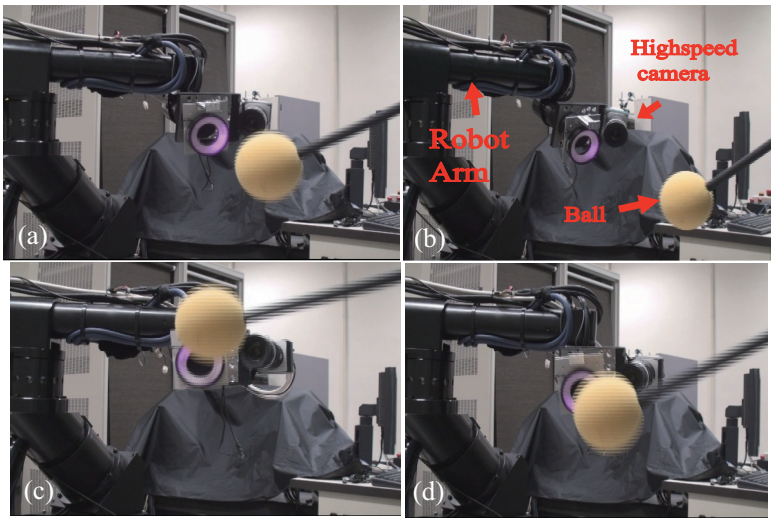

Figure 3.6: Continuous images of ball tracking process.

3.2 Pre-compensated PD control for compensation actuator

In this section, concerning with the control issue of the compensation actuator, a pre-compensated PD approach is proposed under the context of DCRS.

3.2.1 The problem

As the analysis for the dynamic compensation concept has shown, the approximation in Equation 2.7 and 3.9 is supported with the high-speed visual feedback. As a matter of fact, we can make the approximation much more reliable by developing some pre-compensation algorithm for the compensation actuator.

As shown in Figure 3.7, it is reasonable to take the interaction force from the compensation actuator to the main robot τ_m^i to be negligible, since the compensation actuator is lightweight and its applied force τ_m is much smaller than the applied force τ_M on the main robot. However, the interaction force τ_M^i would bring great impact on the compensation actuator, and it may make the approximation in Equation 2.7 and 3.9 not reliable. Although the simple PD control can realize dynamic compensation to some extent as have described in section 2.3, advanced control algorithms that can resist the non-linear interaction force τ_M^i should be developed.

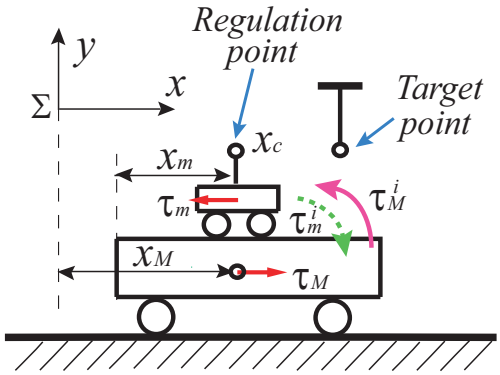

Figure 3.7: The problem for compensation actuator

3.2.2 A simple cart model

A simplified cart model consisting the lower main plant and the upper compensation plant is shown in Figure 3.8. The system only conducts horizontal motion. Assume the compensation plant could not move off from the main plant, and the

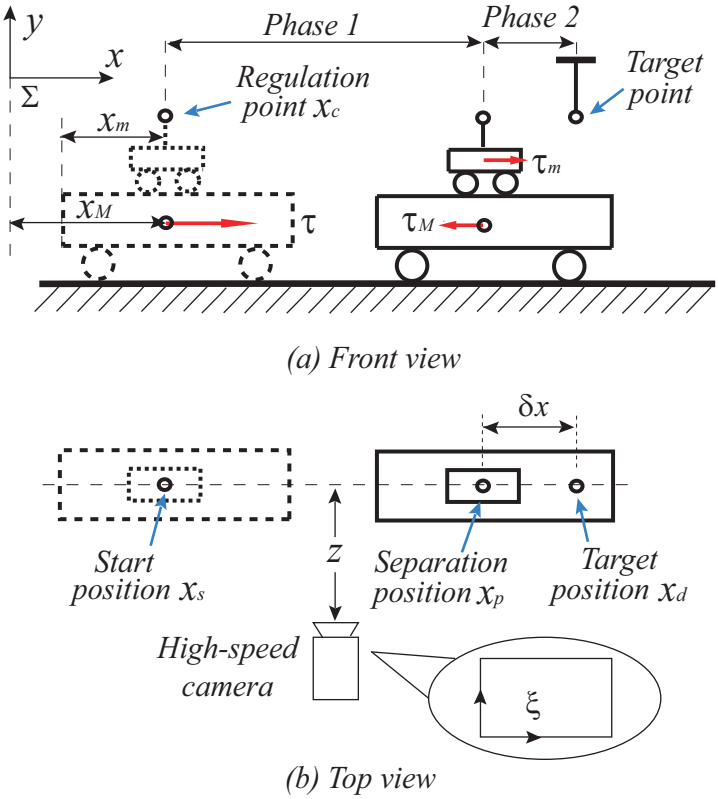

Figure 3.8: A simplified cart model for the 1-DOF DCRS.

compensation plant's mass is m_2, which is far more lighter than the main plant's mass m_1 ($m_2 \ll m_1$). The camera's focal length and scaling factor (pixel/meter) is f and α respectively, and the constant distance between the camera and robotic system is z ($z > 0$). Hereafter, we will refer to the regulation point's position as x_c, and the main plant's position as x_M in the world coordinate Σ. The regulation point is initialized at x_s, and the target position is at x_d. Assume during the whole motion range, both of the regulation point and the target point are within the field of view of the high-speed camera. Since the system only conducts horizontal motion, we can make the projection from world position x to the image position ξ by

$$\xi = \frac{f\alpha}{z}x = \lambda x \tag{3.21}$$

Dividing the regulation of x_c from x_s to x_d into two phases, firstly to regulate the system to move as a whole from x_s to x_p, and secondly, to regulate the compensation plant from x_p to x_d. x_p is the separation position for dividing these two phases. Assume the constant distance from x_p to x_d to be δx ($\delta x \geq 0$),

and it is smaller than the stroke of the compensation plant. Let $e_c = \xi_c - \xi_d$ represents the image error between the regulation point and the target, and $e_p = \xi_c - \xi_p$ represents the image error between the regulation point and the separation position.

For the general case, suppose the control law for the first phase is the simple proportional-derivative (PD) control as

$$\tau' = -K_v \cdot \dot{e}_p - K_p \cdot e_p \tag{3.22}$$

where K_v, K_p are the positive gain factors, and τ' is the force applied on the main plant to drive the whole system. While the image error e_p firstly reaches zero, the system's control moves into the second phase. As for the dynamics of the system, we have:

$$m_1 \cdot \ddot{x}_M + m_2 \cdot \ddot{x}_c = \tau_M + \tau_m \tag{3.23}$$

Where τ_M, τ_m are applied forces for main plant and compensation plant respectively.

For the robot's main plant that is supposed to stop around ξ_p, in order to keep the flexibility of the proposed approach, we keep the PD control law for the main plant as

$$\tau_M = -K_v \cdot \dot{e}_M - K_p \cdot e_M \tag{3.24}$$

where $e_M = \xi_M - \xi_p$.

Note that during the second phase, e_c is the projection of the combination of several motions, including the main plant's motion, the relative motion between the main plant and the compensation plant, and the target's motion if for a general case.

3.2.3 Pre-compensated PD approach

As have been described in section 2.3, a naive PD control law can be applied for the compensation actuator to realize the dynamic compensation. However, it is rather difficult for the linear PD controller to accommodate with the nonlinear dynamic impact brought from the lower main plant. Taking into the consideration of the main plant's motion impact, we develop the pre-compensated control law based on the conventional PD control. The block diagram of the dynamic compensation controller is shown in Fig.3.9.

The control law is as follows:

$$\tau_m = u_m - \tau_M + m_1 \cdot \ddot{x}_M \tag{3.25}$$

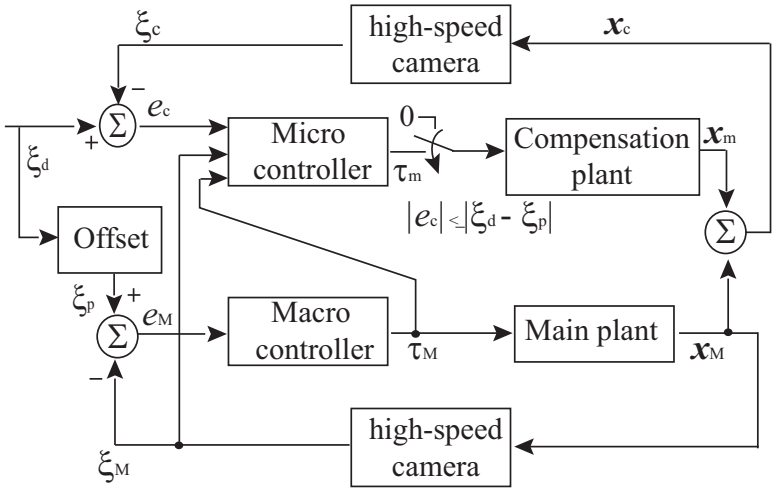

Figure 3.9: Block diagram of the pre-compensated PD control

Where u_m is:

$$u_m = -K_v^m \cdot \dot{e}_c - K_p^m \cdot e_c \tag{3.26}$$

where, K_v^m, K_p^m are positive-definite gain factors, $e_c = \xi_c - \xi_d$, and $\ddot{x}_M$ is the second order information of the main plant, which is obtained from the high-speed camera's images. With Equation (3.23), Equation (3.24) and Equation (3.25), the closed-loop system is:

$$\begin{aligned} \ddot{x}_M \cdot m_1 + (\ddot{x}_m + \ddot{x}_M) \cdot m_2 &= u_m + m_1 \cdot \ddot{x}_M \\ &= -K_v^m \cdot \dot{e}_c - K_p^m \cdot e_c + m_1 \cdot \ddot{x}_M \end{aligned} \tag{3.27}$$

In order to proof the stability of the control law by Equation (3.25), a positive-definite Lyapunov function candidate can be defined as:

$$V(e, \dot{e}) = \frac{1}{2} m_2 \cdot \dot{e}^2 + \frac{1}{2} K_p^m \cdot \lambda \cdot e^2 \tag{3.28}$$

where $e = e_c = \xi_c - \xi_d$. Evaluating the derivative of V: $\dot{V}$ with the closed-loop system, we have

$$\begin{aligned} \dot{V}(e, \dot{e}) &= m_2 \cdot \dot{e} \cdot \ddot{e} + K_p^m \cdot \lambda e \cdot \dot{e} \\ &= -K_v^m \cdot \lambda \cdot \dot{e}^2 \end{aligned} \tag{3.29}$$

Since K_v^m, λ are all positive-definite, hence $\dot{V}$ is globally negative semi-definite, and $\xi = \xi_d, \dot{e} = 0$ is a stable equilibrium point. It is not difficult to conclude that the point $\xi = \xi_d, \dot{e} = 0$ is also asymptotic stable with the Lasalle's theorem [61].

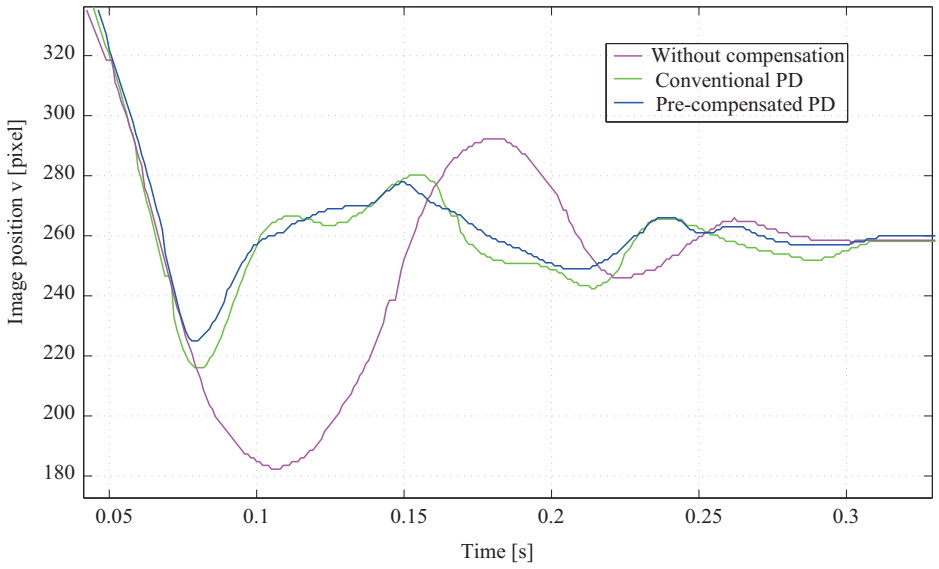

Figure 3.10: Transient compensation performance

The advantage of the control law by Equation (3.25) is that the main plant's motion pattern is always taken into the consideration for generating the output force for the compensation plant, and thus the dynamic impact from the main plant to the compensation plant can be suppressed. However, it is not the best way to incorporate the acceleration information that obtained by differentiating from the image frames. Besides, it is a trivial work to tuning the gain coefficients in Equation (3.25) in order to realize the perfect regulation. As the experimental evaluation for transient compensation (same experimental settings as that in section 2.3) shown in Fig.3.10, comparing with the conventional PD approach, the proposed pre-compensated PD approach shows a slightly improved dynamic performance in terms of the compressed overshot. In Fig.3.11, it can be seen that the pre-compensated PD has a better compensation performance since the compensated error has been smaller than that of the simple PD control.

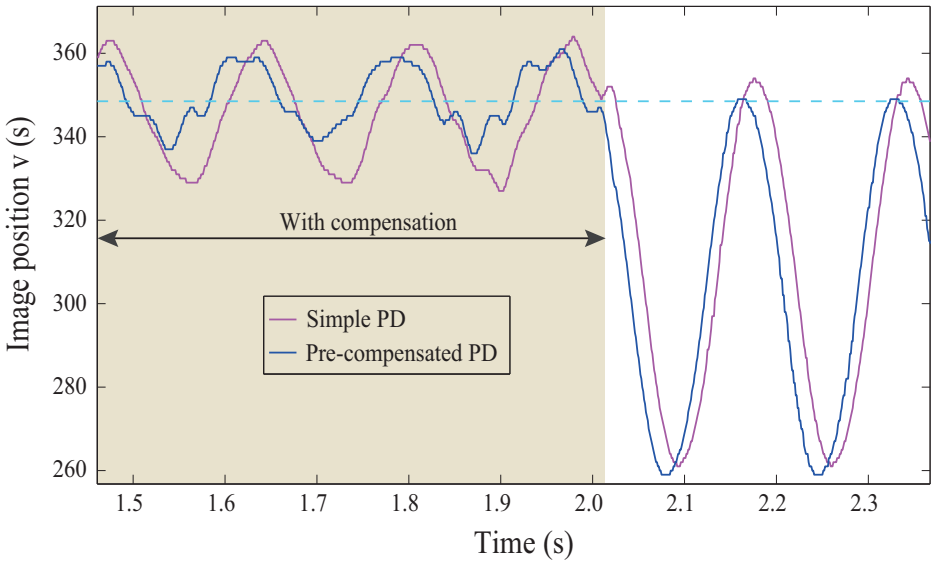

Figure 3.11: Vibration compensation (6 Hz) performance

3.3 Summary of this chapter

In this chapter, under the high-speed visual feedback based on relative coordinate, a simplified IBVS approach that is depth-independent for robot arm's regulation as well as a pre-compensated PD approach for compensation actuator have been proposed. The proposed algorithms fit for the situation of many uncertainties in controlling the main plant as well as the compensation plant and make the proposed dynamic compensation approach much more flexible in realizing accurate and high-speed manipulations.

Although the simplified IBVS approach can hardly be the optimal solution for position regulation, it is easy for implementation, robust to noise and flexible for application. As will be addressed in Chapter 5, the simplified IBVS approach is adopted to realize the set point regulation of the robot arm in doing the 3D peg-and-hole alignment task. The pre-compensated PD approach has a better compensation performance than the simple PD control as it takes into consideration of the dynamic impact brought by the main robot. Although there are some trivial tuning task involved in this approach, the methodology of pre-compensating the compensation actuator with the supervised motion pattern of the main robot is instructive to the much more sophisticated approach applied in the 1D dynamic super picking task which will be addressed in the next chapter.

Chapter 4

1D positioning: dynamic super picking

In this chapter, the proposed dynamic compensation concept will be applied to 1D positioning, which is the basic form of the DCRS's applications. In order to realize the better compensation performance by the compensation actuator, a pre-compensation fuzzy logic control (PFLC) method is proposed by further exploiting the properties of the 1-DOF DCRS. Simulation and experimental evaluations for the PFLC method show its effectiveness in counteracting the dynamic impact from the main plant. Since the effective cooperation between the big range coarse motion by main plant and the accurate motion by compensation plant within small range is very important, an efficient cooperation algorithm based on gain adjusting is proposed. Finally, dynamic super picking task is realized with good performance based on the PFLC approach as well as the cooperation algorithm.

4.1 Background

Robots capable of catching dynamic flying objects have been investigated previously. The flying object catching task requires high-speed and high accuracy for image processing, as well as motion control within the very short time. It has been adopted as a challenging benchmark task for almost 20 years to develop and test robotics technologies.

Among the related works, most of the approaches have employed the stereo vision systems to realize the 3D position reconstruction and prediction for catching targets [62, 63, 64, 65, 66, 67], and then with the motion planning algorithms, the robot is guided to the catch configuration, where the catch point has been determined based on the predicted trajectory of the target. In [64], the target

position was tracked and predicted by using an Extended Kalman Filter (EKF), with the consideration of the air drag. Since the target's trajectories may cover large workspace, the calibration of the stereo cameras needs samples (3D position and the corresponding image positions) of the target covering the whole workspace. In order to get the high precision calibration, "Calibration by Doing" procedure has been adopted to get the samples. As for the results, it is said that about 2/3 of the 100 trials was successful in catching the ball, with the clearance of 4.5 cm (the picking net has the diameter of 16 cm, and the ball with the diameter 7 cm). In their later work [66], a robotic ball-catching system built from a multipurpose 7-DOF lightweight arm (DLR-LWR-III) and a 12-DOF four-fingered hand (DLR-Hand-II) was developed. The grasping of the ball was realized by formulating the decision of where, when and how to catch the ball as an unified nonlinear optimization problem with nonlinear constraints. With the same experimental settings and EKF method, the success rate of catching was about 80% and the main failures had been resulted from the prediction errors and lose of ball tracks by the vision systems [66]. As the further work in [67], they extended the ball catching task to the wheeled humanoid robot *Rollin's Justin* and instead of using the static stereo cameras, two cameras have been mounted on the robot's shaking head. In order to compensate for the shaking of the cameras along with the robot head while the robot moves, a 6-DOF inertial measurement unit (IMU) has been adopted. Multi-Hypothesis Tracker (MHT) with an Unscented Kalman Filter (UKF) is applied for predicting the target's trajectories. The catch-rate of about 80% was realized with a ball (8.5 cm diameter) thrown from about 5-7 m away towards the robot.

Besides, there are also several approaches that employ no information to reconstruct 3D space from the 2D images. In [68], a GAG (Gaining Angle of Gaze) motion strategy was proposed to realize the trajectory control method for catching a ball flying in 3D space. In their approach, hand-eye configured monocular vision system was adopted and it didn't need for the 3D reconstruction for the target. Only the vertical optical angle was required to be observed for the GAG model. By keeping the value of the vertical optical angle gaining in a finite rate of change, it was resultantly possible for the hand to track and catch the target. In [69], a novel concept called the goal-oriented just-in-time visual servoing was proposed to realize the ball catching task by robot arm. In their approach, the Jacobian was estimated on-line to combine the image motion and 3D motion of the robot arm without the prior knowledge of the arm and camera structures for hand-eye and camera calibrations. Rather than one camera, two or more cameras with different viewing points were adopted to interpret the 3D space catching in 2D images by the following way: the ball should reach the catch point on the robot arm's end-effector at the same time from different cameras' images, and it did not necessarily mean the success of the catching if only in one image the

ball met the catch point. However, as pointed by the authors, the weakness of their approach was that they cannot guarantee the fulfillment of the given task completely in time. The most important reason was that the low sampling rate of the cameras (30 fps) can hardly satisfy the control frequency of the image-based estimation and regulation.

Unlike the prediction approach described above, perceptions of targets during dynamic catching manipulations [15, 70, 71, 72, 73] conducted in our laboratory have been mainly relied on the high-speed visual feedback. Since the tracking or prediction through algorithms based on the past states of the target would inevitably involve much larger errors than the errors brought by the sensor noise. Besides, with the high-speed visual feedback, not only the computation time can be saved (no need for complex filtering algorithms), but also the image processing algorithms become easier for implementation and the target detection can be much more accurate. Instead of realizing catching based on the 3D information reconstruction from the high-speed vision sensors, this study will focus on the high-speed visual feedback based on relative coordinate information, which means that the calibration works for camera will be greatly reduced. And we intend to realize a much better performance in catching accuracy either in space or in time. In order to simplify the problem of dynamic catching task, here the simplest form: 1D dynamic picking (catching) is to be conducted.

4.2 System design

In accordance with the dynamic compensation concept, a 1-DOF DCRS is designed as shown in Figure 4.1. The system includes a main robot (refer to Figure 2.5) that has a large work space and has been originally designed for slow & accurate motion. It has a bad dynamic performance while adopted for high-speed motion. The compensation actuator (refer to Figure 2.6) is capable of high-speed motion with a small work range. Hereafter, we will refer to the main robot as the main plant, and the compensation actuator as the compensation plant. Specifications for the testbed is shown in Table 4.1. A 1000 Hz high-speed camera (refer to Figure 2.8) observes both the target point and the regulation point. The position of picking net (the net has a inner diameter of 15 mm) is detected in images by a LED light fixed in the center position of the net, and the target is a light-reflective plastic ball with a diameter of 12 mm. Thus the clearance for catching (picking) is 1.5 mm. In order to limit the target's drop position within the workspace of the picking net (with only 1-DOF), a narrow space for passing through the target is formed by two transparent plastic boards.

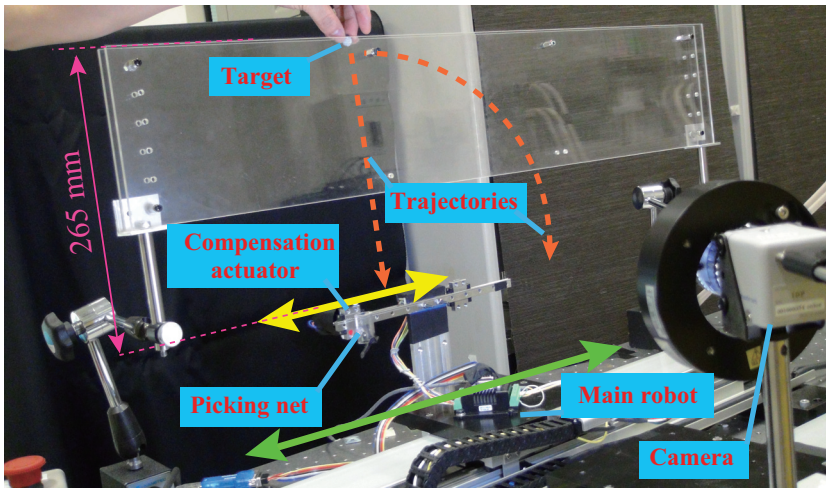

Figure 4.1: System designed for dynamic picking task in 1-DOF

Table 4.1: System specification for the testbed.

	Main plant	Compensation plant
Max velocity (m/s)	2.0	2.9
Max acceleration (m/s^2)	3.0	148.5
Stroke (mm)	80	750

4.3 Algorithms for realizing dynamic super picking

In order to realize the accurate picking of the target under dynamical flying motions, the effective control for the compensation plant that will be constantly affected by the dynamic impact of the main plant is quite important. Besides, the cooperation between these two plants is also critical for picking a target that is flying within a big range. A pre-compensation fuzzy logic control (PFLC) algorithm [74] is proposed for the compensation plant. After that, a cooperation algorithm based on simple gain adjusting will be addressed.

4.3.1 Pre-compensation fuzzy logic control (PFLC) for compensation actuator

4.3.1.1 Methodology

Although the pre-compensated PD control approach shows better compensation performance than the simple PD control as has been described in section 3.2, it involves trivial tuning task for implementation. Here, based on the pre-compensated PD approach's methodology of taking into consideration of the main plant's motion impact, we further propose a pre-compensation approach based on the fuzzy logic control.

Fuzzy logic method is able to simultaneously handle numerical data and linguistic knowledge. It differs from classical logic in that statements are no longer black or white, true or false, on or off. In traditional logic an object takes on a value of either zero or one. In fuzzy logic, a statement can assume any real value between 0 and 1, representing the degree to which an element belongs to a given set. Comparing with the classical model-based approach, it needs no intricate mathematical models, only a practical understanding of the overall system behavior. The Fuzzy logic control method have been successfully applied in fields such as automatic control, data classification, decision analysis, expert systems, and computer vision [75, 76].

Back to the motion analysis based on the simple cart model (refer to the Section 3.2.2), let's check the differential of e_c ($\dot{e}_c$) at a particular time, saying for the time of $k+1$,

$$\dot{e}_c^{k+1} = \lambda(v_c^{k+1} - v_d^{k+1}) \tag{4.1}$$

where v_c^{k+1}, v_d^{k+1} refers to the velocity of the regulation point and the target point at time of $k+1$ respectively. Suppose at time of k, the output force for the compensation plant and main plant to be τ_m^k, τ_M^k respectively, for the velocity of the regulation point, we have

$$v_c^{k+1} = v_c^k + (\frac{\tau_m^k}{m_1} + \frac{\tau_M^k}{m_1 + m_2})\Delta t \tag{4.2}$$

where, Δt is the control cycle time. Similarly, we have the velocity of the main plant at time of $k+1$ as

$$v_M^{k+1} = v_M^k + \frac{\tau_M^k}{m_1 + m_2}\Delta t \tag{4.3}$$

Combine Equation (4.2) and Equation (4.3), we have

$$\dot{e}_c^{k+1} = \lambda[(v_M^{k+1} - v_d^{k+1}) + (v_c^k - v_M^k) + \frac{\tau_m^k}{m_1}\Delta t] \tag{4.4}$$

Change Equation (4.4) to be

$$\dot{e}_c^{k+1} = \dot{e}_M^{k+1} + (\dot{e}_c^k - \dot{e}_M^k) + \lambda\frac{\tau_m^k}{m_1}\Delta t \tag{4.5}$$

Equation (4.5) shows that at the time of $k+1$, the change of the error e_c has relations to three aspects, namely the change of the error e_M at time $k+1$, the difference between $\dot{e}_c$ and $\dot{e}_M$ at time k, as well as the force for the compensation plant at time k.

If we apply the simple PD control for the compensation plant as

$$\tau_m = -K_{v2}\dot{e}_c - K_{p2}e_c \tag{4.6}$$

where K_{v2}, K_{p2} are positive gain factors. Note that in the PD approach, the input force τ_m at time of k is a function of $\dot{e}_c^k$ and e_c^k. For the reason $\dot{e}_c$ is not only affected by the compensation plant's regulation as illustrated above, the simple PD control law above can hardly be a good approach, since the regulation of the compensation plant by Equation (4.6) would be greatly affected by the dynamics of the main plant, such as the part $\dot{e}_c^k - \dot{e}_M^k$ in Equation (4.5) while performing high-speed motions.

Combining the feature of the fuzzy logic method and the concrete task of regulating the compensation plant under the high-speed visual feedback, a conventional fuzzy logic control system that takes $\dot{e}_c^k$ and e_c^k as the input and τ_m^k as the output at the time of k can be developed. Comparing with the simple PD control illustrated above that basically fit for the linear system, the conventional fuzzy logic approach may be a suitable approach to handle the nonlinear behavior of high-speed motion compensation system. But the same problem as have illustrated for the PD method also exists for the conventional fuzzy logic approach since it will be dynamically affected by the main plant's motion.

Back to the Equation (4.5), we could see that at the time of k, $\dot{e}_c^k - \dot{e}_M^k$ is of known. And in order to have a better control of $\dot{e}_c$ at the coming time of $k+1$, we can actually take the factor $\dot{e}_c^k - \dot{e}_M^k$ into consideration for generating the output force τ_m at the time of k rather than only a function of $\dot{e}_c^k$ and e_c^k. In another word, we can realize pre-compensation for the compensation plant by using $\dot{e}_c^k - \dot{e}_M^k$ to counteract the dynamic impact from the main plant. On base of the conventional fuzzy logic method, the pre-compensation fuzzy logic control

(PFLC) approach is proposed. The block diagram of the proposed PFLC is shown in Figure 4.2. Comparing with conventional fuzzy logic control, the innovation point of the proposed method is that it also takes into consideration of the main plant's motion in a cascade fuzzy logic model. Through the feedback information of the main plant's motion, nonlinear dynamic effect on the compensation plant can be compensated simultaneously while the compensation plant is regulated to the target position. The proposed PFLC method is a direct regulator to the plant rather than a gain tuner that has to be combined with some other control laws as in [77, 78], thus it is much more easier for implementation.

The PFLC includes two cascade fuzzy inference systems (FIS), one is for pre-compensation (referred as FIS_1 hereafter) and the other is for error regulation (referred as FIS_2). The FIS_1 is actually to combine the velocity information of the main plant and compensation plant through high-speed visual feedback. The output of FIS_1 then be taken as one input to the FIS_2 to generate the output force for driving.

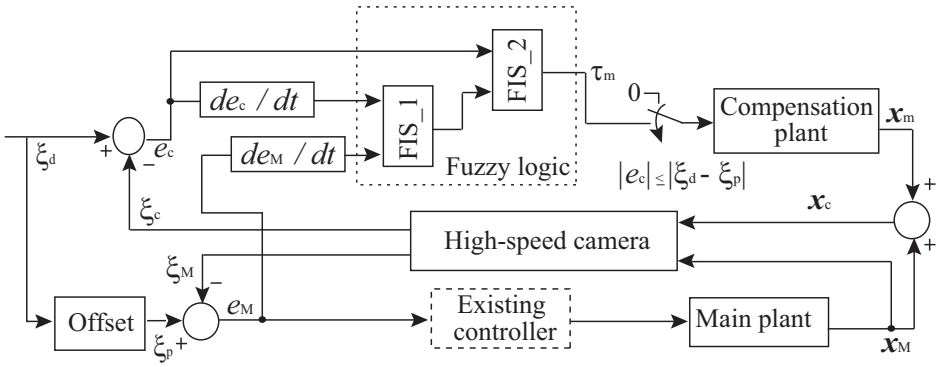

Figure 4.2: Block diagram of the proposed pre-compensation fuzzy logic control (PFLC) method.

4.3.1.2 Implementation of PFLC

The implementation of a fuzzy logic control system basically includes the steps of fuzzification, rule evaluation and defuzzification. For both FIS_1 and FIS_2, the universe of discourse for each input is partitioned into seven fuzzy sets as *NL* ('negative large'), *NM* ('negative medium'), *NS* ('negative small'), *ZE* ('zero'), *PS* ('positive small'), *PM* ('positive medium') and *PL* ('positive large'). Both FIS_1 and FIS_2 has two input variables and one output variable. For FIS_1, the two input variables are $\dot{e}_M$ and $\dot{e}_c$, representing for the image error's velocity information relating to the main plant and the compensation plant respectively, the output is referred as $\dot{e}_{com}$. For FIS_2, the input variables are the image error

e_c and the output of FIS_1. The fuzzification is to map each crisp input over all the qualifying membership functions required by the fuzzy rules. In order for the easy implementation, the simplest triangular membership function is adopted for the input $\dot{e}_M$, $\dot{e}_c$ and e_c as shown in Figure 4.3. The universe of discourse for each input variable has been roughly calibrated.

After the step of fuzzification, the fuzzy rules are designed for FIS_1 and FIS_2. Under the 'zedeh AND' fuzzy combination operator, the designed fuzzy associate memory matrix (FAMM) for FIS_1 and FIS_2 are shown in Table 4.2 and Table 4.3 respectively. Each element of the FAMM refers to one If-Then rule statement. For instance, for the element FAMM-1(1,1): *NL*, it means that:

'If $\dot{e}_M$ is *NL* AND $\dot{e}_c$ is *NL* Then output is *NL*'

As for the output variables in FIS_1 and FIS_2, the universe of discourse is partitioned into seven fuzzy sets with each attribute being described by the singleton membership functions as shown in Figure 4.4. The seven fuzzy sets are same as the input fuzzy sets. Thus the developed fuzzy system falls into the so-called Sugeno-type fuzzy inference [76]. Because of the linear dependence of each rule on the input variables of FIS_1 and FIS_2, it is fairly proper and easy for implementation to adopt the Sugeno fuzzy inference system here as it smoothly interpolate the linear gains that would be applied across the inputs space.

The firing strength of the *(i,j)*-th element in FAMM-1 of FIS_1 is computed as

$$\mu_{\beta_{ij}}(\dot{e}_{com}) = \mu_i(\dot{e}_M) \cdot \mu_j(\dot{e}_c) \tag{4.7}$$

where $\mu_{\beta_{ij}}(\dot{e}_{com})$ means that the degree of the fuzzy set $\beta(\dot{e}_{com})$ fired by $\mu_i(\dot{e}_M)$ and $\mu_j(\dot{e}_c)$. β is among the output fuzzy sets {*NL, NM, NS, ZE, PS, PM, PL*}. Evaluation of all the rules leads to

$$\mu_\beta(\dot{e}_{com}) = sqrt(\Sigma\mu^2_{\beta_{ij}}) \tag{4.8}$$

The defuzzification strategy adopted is a simplified version of the 'center of gravity method' as

$$\dot{e}_{com} = \frac{\Sigma C_\beta \cdot \mu_\beta}{\Sigma\mu_\beta} \tag{4.9}$$

where C_β is the constant value for the fuzzy set β defined by the output membership function. The fuzzification, rule evaluation as well as defuzzification process for FIS_2 is the same as FIS_1. The surface view of output for FIS_1 and FIS_2 is shown in Figure 4.5.

Table 4.2: FAMM-1

$\dot{e}_M$ \ $\dot{e}_c$	NL	NM	NS	ZE	PS	PM	PL
NL	NL	NL	NL	NL	NM	NS	ZE
NM	NL	NL	NL	NM	NS	ZE	PS
NS	NL	NL	NM	NS	ZE	PS	PM
ZE	NL	NM	NS	ZE	PS	PM	PL
PS	NM	NS	ZE	PS	PM	PL	PL
PM	NS	ZE	PS	PM	PL	PL	PL
PL	ZE	PS	PM	PL	PL	PL	PL

Table 4.3: FAMM-2

e_c \ $\dot{e}_c$	NL	NM	NS	ZE	PS	PM	PL
NL	PL	PL	PL	PL	PL	PM	PM
NM	PL	PL	PL	PM	PM	PS	PS
NS	PL	PL	PM	PS	ZE	NS	NM
ZE	PL	PM	PS	ZE	NS	NM	NL
PS	PM	PS	ZE	NS	NM	NL	NL
PM	NS	NS	NM	NM	NL	NL	NL
PL	NM	NM	NL	NL	NL	NL	NL

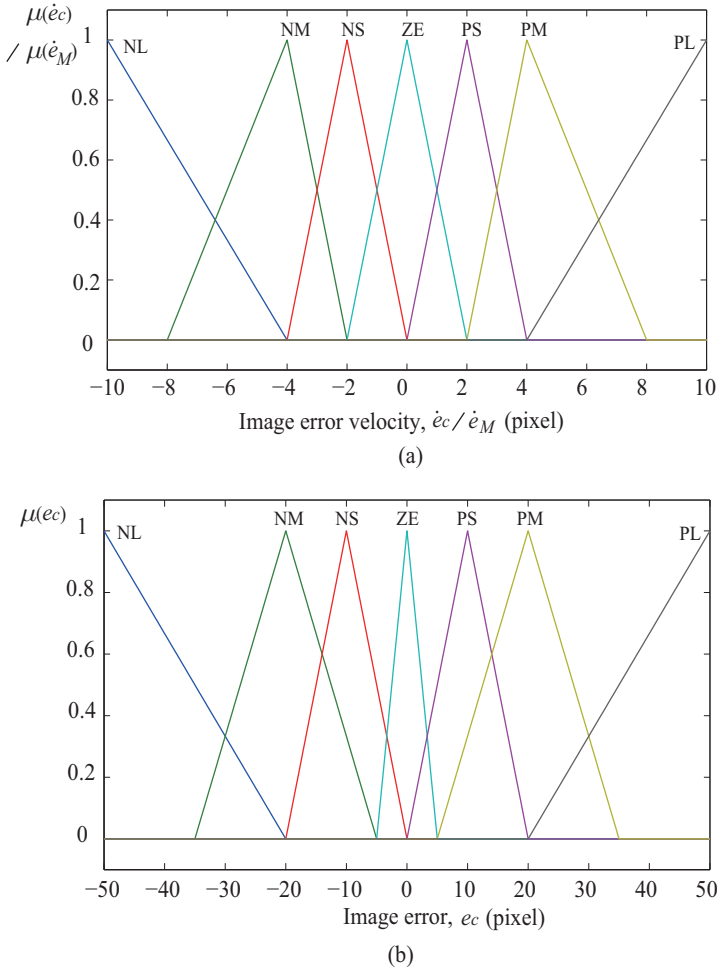

Figure 4.3: Membership functions for the input variables.

4.3.1.3 Simulation study

The simulation is done with the Matlab's fuzzy logic toolbox [79]. In order to exam the dynamic performance of the dynamic compensation algorithm, both point-to-point regulation and high-speed vibration compensation have been conducted by using the simple cart model illustrated above. The mass for main plant and compensation plant is set to be 28 kg and 2 kg respectively. Since we only implement the horizontal motion, the variance of the image position for the system along vertical direction is perceived as zero.

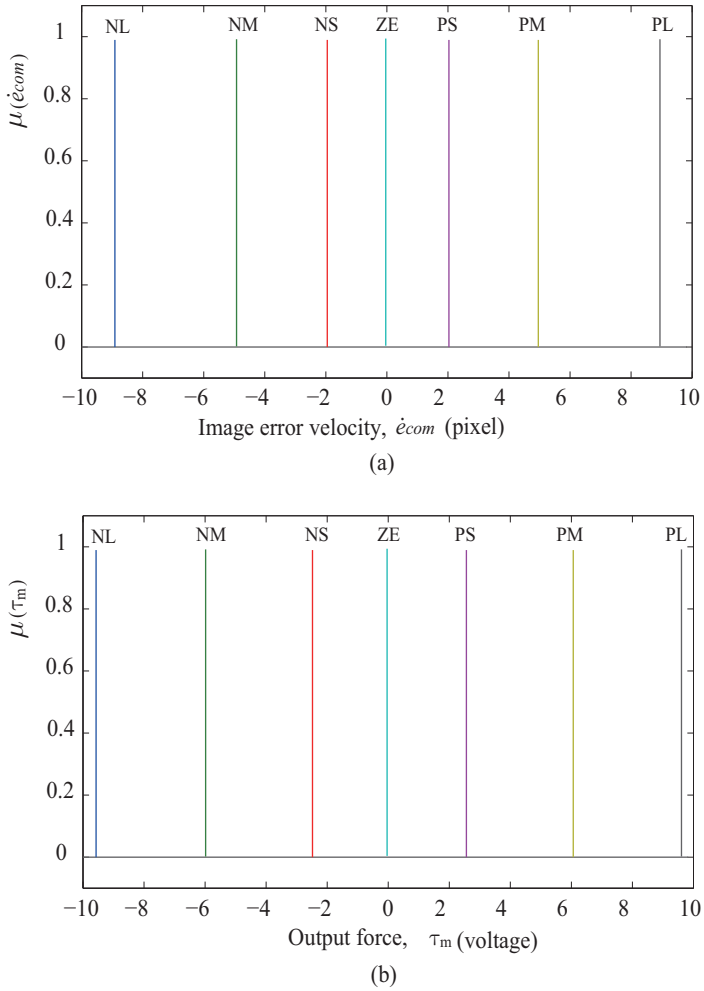

Figure 4.4: Membership functions for the output variables.

Point-to-point regulation

The start position and target position in image is set to be $\xi_s = -200$ and $\xi_d = 0$ respectively. From the start position, the whole system is controlled to move as a whole by the main plant's non-optimal controller, and here suppose it to be a common PD controller. At the image position of $\xi_p = -5$, the compensation plant is activated to perform the relative motion under the conventional fuzzy logic control and the proposed PFLC method. As shown in Figure 4.6, the system shows a longer settling time if there was no compensation motion involved. Comparing with the conventional fuzzy logic control, the proposed PFLC method shows the improvement of compressing the overshot and shorting the settling time.

Vibration compensation

In order to check the system's compensation performance under high-speed motion, we let the target point to follow a *sin(·)* reciprocating motion as follow:

$$\xi_d = 200 + 80sin(2\pi f \sum_{i=1}^{n} \Delta t_i) \tag{4.10}$$

where ξ_d is the reference image position, $f = 8$ Hz defines the frequency, and $\Delta t_i = 1$ ms is the control cycle time. The reason for choosing the frequency $f = 8$ Hz is that as will be shown later in the point-to-point experimental evaluation, the main plant of the testbed has the oscillation frequency of about 8 Hz while performing point-to-point positioning. Thus hereafter, we will choose $f = 8$ Hz as the evaluation frequency for vibration compensation. As shown in Figure 4.7, the system could hardly follow the target point's trajectory without the compensation plant's motion. Both the conventional fuzzy logic method and the proposed PFLC method realized perfect tracking of the target's high-speed vibration motion. The tracking error is shown in Figure 4.8. It clearly shows that the proposed PFLC method had a smaller tracking error than the traditional fuzzy control, and that was exactly the result of the pre-compensation from the feedback information of the main plant's motion. The applied force to the compensation plant is shown in Figure 4.9. It is quite interesting to see that the PFLC method actually applied a smaller force than the conventional fuzzy control method on average during the tracking process, which also tells the better efficiency of the proposed PFLC method.

4.3.1.4 Experimental evaluations

In accordance with the analysis for PFLC approach, several assumptions are set for the experimental system as follows:

- The friction between the main plant and the compensation plant is large enough, and there will be no relative motion between the main plant and the compensation plant if the compensation plant is not activated.
- The interaction force from the compensation plant to the main plant is small enough and is negligible.
- The motion patterns of the main plant and the compensation plant can both be detected.

It is not difficult to realize the assumptions above. A suitable friction force can be obtained between the main plant and the compensation plant by assembling these

two appropriately. By adding some extra weight on the main plant to increase the inertia, the interaction force from the compensation plant can be taken as small disturbance and is negligible. As for the third assumption, the eye-to-hand configured high-speed camera can easily detect the two plants' motion patterns by a fixed marker (here two LEDs were adopted) on each of them.

Point-to-point regulation

The point-to-point regulation for the main plant was conducted to check the compensation performance in terms of transient behavior. Firstly the whole system was regulated towards the target position in images by the main plant's rough PD controller from the start position $\xi_s = -200$ in images. The compensation plant's motion was triggered once the regulation point reached $\xi_p = 0$. During the experiment, for sake of comparison, we simplified the regulation by letting $\xi_d = \xi_d = 0$. Thus once the compensation plant was triggered at the time $t_0 = 2.15$ s when it reached ξ_p, both the main plant and the compensation plant were regulated to stay at ξ_p. The results for three methods applied to the compensation plant are shown in Figure 4.10. It can be seen that the main plant of the testbed exhibited a 8 Hz oscillation before converged to the target position. The results show that comparing with PD control and conventional fuzzy logic control, the proposed PFLC method compressed the image error during the whole regulation process. For the 10% error band, the settling time was reduced gradually from t_{s4} to t_{s3}, t_{s2} and t_{s1}, representing the point-to-point regulation without compensation, compensation under PD control, compensation under conventional fuzzy control and the proposed PFLC method respectively. The PFLC method had the smallest settling time for the same point-to-point regulation.

Vibration compensation

The vibration compensation was conducted to confirm the tracking capability for the compensation plant under different control methods. In another words, we want to check that how well the regulation point could keep aligned with the target point for different control methods while it always dynamically affected by the reciprocating motion of the main plant. Similarly to the simulation settings, we let the main plant to follow a *sin(·)* reciprocating motion as

$$\xi_d = 210 + 40sin(2\pi f \sum_{i=1}^{n} \Delta t_i) \tag{4.11}$$

and let the frequency $f = 8$ Hz, where $\Delta t_i = 1$ ms is the control cycle time. Three methods including the simple constant gain PD control, the conventional fuzzy logic control and the proposed PFLC method were adopted to conduct the

comparison. Note that for the PD method, the gain coefficients have been tuned. For both the conventional fuzzy logic method and the proposed PFLC, there were fewer works concerning parameter tuning, but we have tried several groups of the membership functions, especially for the output membership functions of FIS_1 and FIS_2.

As shown in Figure 4.11, the proposed PFLC method realized perfect tracking of the target's high-speed vibration motion, while the conventional fuzzy logic control had a less good performance and the PD method was the worst. The tracking error is shown in Figure 4.12. It clearly shows that the proposed PFLC method had a smaller tracking error than the other two methods. In another words, the regulation point could keep well aligned with the target point if we take into consideration of the reciprocating motion of the main plant that have been dynamically affecting the regulation process. Figure 4.13 shows the output of the FIS_1 that combined the error changing information between the regulation point and the target point, as well as the velocity information of the main plant. It can be seen that during the 'Active adjusting phase', the compensation plant's motion $\dot{e}_c$ had a major effect on the output of the FIS_1, while during the 'Stable tracking phase', the main plant's motion $\dot{e}_M$ held the major effect on the output $\dot{e}_{com}$. This implies the functioning of the pre-compensation.

The applied force to the compensation plant is shown in Figure 4.14. It also tells the same phenomenon that the PFLC method actually applied a smaller force than the conventional fuzzy control method on average during the tracking process, which also can be perceived as the 'passive advantage' thanks to the pre-compensation from the main plant's motion. As for the PD method, it always tried to drive the compensation plant with the maximum force in order to realize the high-speed tracking, yet a time lag was constantly existed as shown in Figure 4.14 and Figure 4.11. The video for vibration compensation with the proposed PFLC method can be found on the website [80].

We also tried to realize the vibration compensation for several different motion speed of the main plant. The results for a frequency of 4 Hz, 6 Hz and 8 Hz are shown in Figure 4.15 and for a random frequency is shown in Figure 4.16, which tells the image error of different control methods. For the PD method, the image error basically becomes larger along with a higher speed motion of the main plant. The same trend can also be seen for the conventional fuzzy logic method except that the changing rate was small. For the proposed PFLC method, we could see that the image error almost kept the same range for different motion speed of the main plant, all in a quite small quantity.

4.3.2 Cooperation algorithm for two plants

The main plant is scheduled to perform the coarse positioning, and the accurate positioning is realized by the compensation actuator. The motion planning for these two plants with good efficiency is very important, under the constraint that the compensation actuator has a small work range (stroke). A simple cooperation algorithm based on gain adjusting is proposed as shown in Figure 4.17. The methodology is that through adjusting the gain coefficient K_{cM} for the main plant and K_{cm} for the compensation plant, the two plants realize the cooperative motion. Since the main plant is controlled based on simple PD with the output τ_M, and the compensation actuator is controlled by the PFLC method with the output τ_m, the inputs for two plants are τ'_M and τ'_m respectively, with

$$\tau'_M = K_{cM} \cdot \tau_M \tag{4.12}$$

$$\tau'_m = K_{cm} \cdot \tau_m \tag{4.13}$$

As shown in Figure 4.17, K_{cM} and K_{cm} is decided by trapezoid membership functions. If the target is out of the work range of the compensation plant, the compensation plant will be inactive by setting K_{cm} to be zero while the main plant will be controlled to move to the center position ("C") by PD method with $K_{cM} = 1$. If the target goes into the work range of the compensation plant, the motion of the main plant will be suppressed until to stop motion within the "Dead zone" which is between "D1" and "D2", whereas the compensation plant will be active with the PFLC control method.

It should be pointed out that in order to judge the relative position between the target and the two plants, the rough calibrations for the positions of "L, D1, C, D2, R" in terms of offset from the separation point in images should be conducted.

In order to show the better efficiency of the proposed dynamic compensation concept over traditional method, it is reasonable to compare the tracking performance of a random vibration target by main plant (with PD control) and by the proposed compensation approach with two plants (with PFLC algorithm and cooperation algorithm). We checked the performance of tracking under the uncertain dynamics property of the main plant by adding an extra load. The result for tracking a target with random vibration motion from 1 Hz to 4 Hz is shown in Figure 4.18. It is obvious that the tracking error has been greatly dependent on the dynamics property under the main plant's tracking, and that's the reason for tunning the gain coefficients for the PD controller under different dynamics property of the main plant. However, the tracking error under the two plants approach has been greatly reduced and turns out to be less effected by the uncertain dynamics property of the main plant.

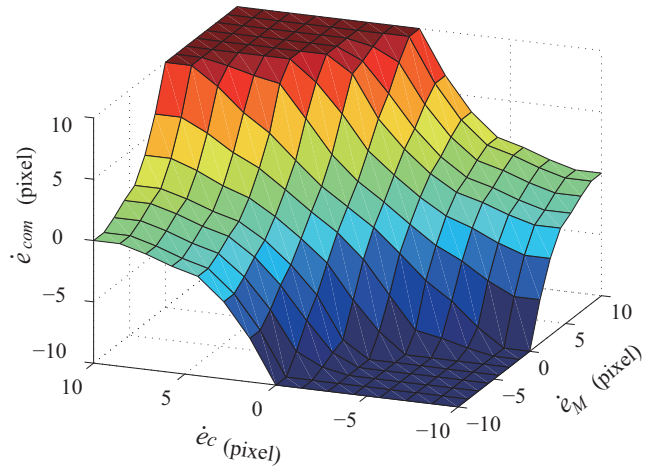

(a)

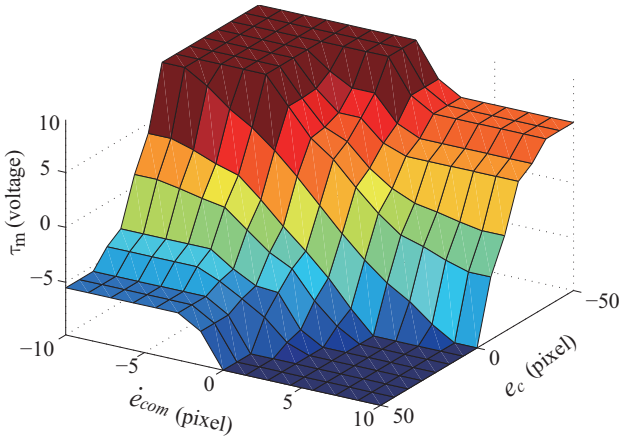

(b)

Figure 4.5: Surface view of the output for fuzzy inference. (a): FIS_1; (b): FIS_2.

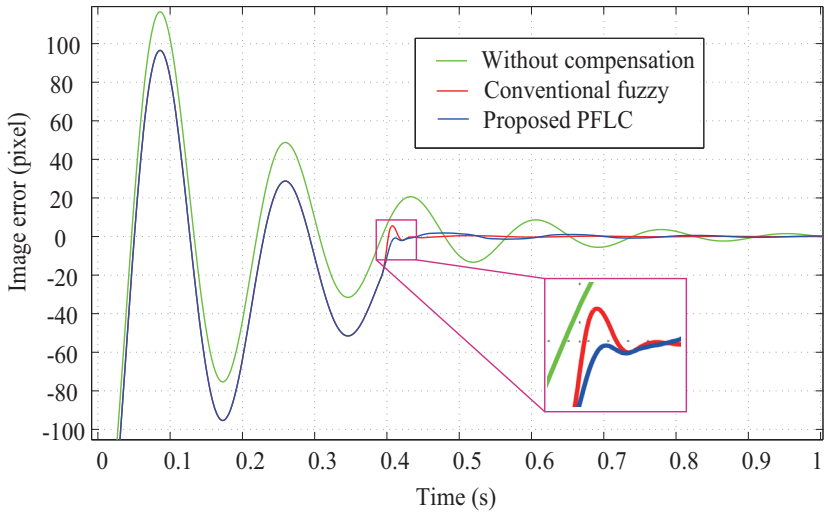

Figure 4.6: Simulation result of image error for point-to-point compensation.

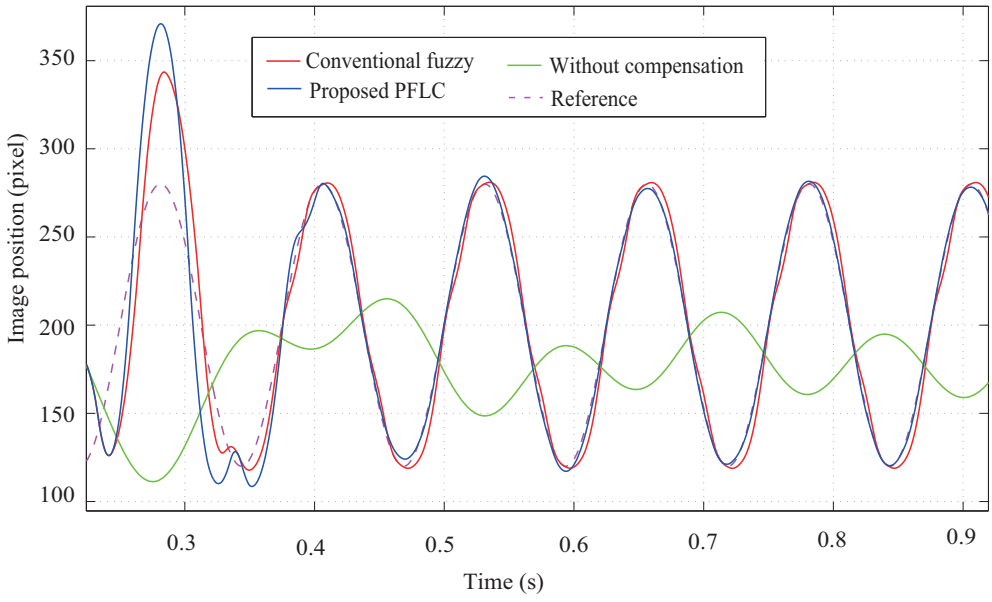

Figure 4.7: Simulation result of image trajectory for vibration (8 Hz) compensation.

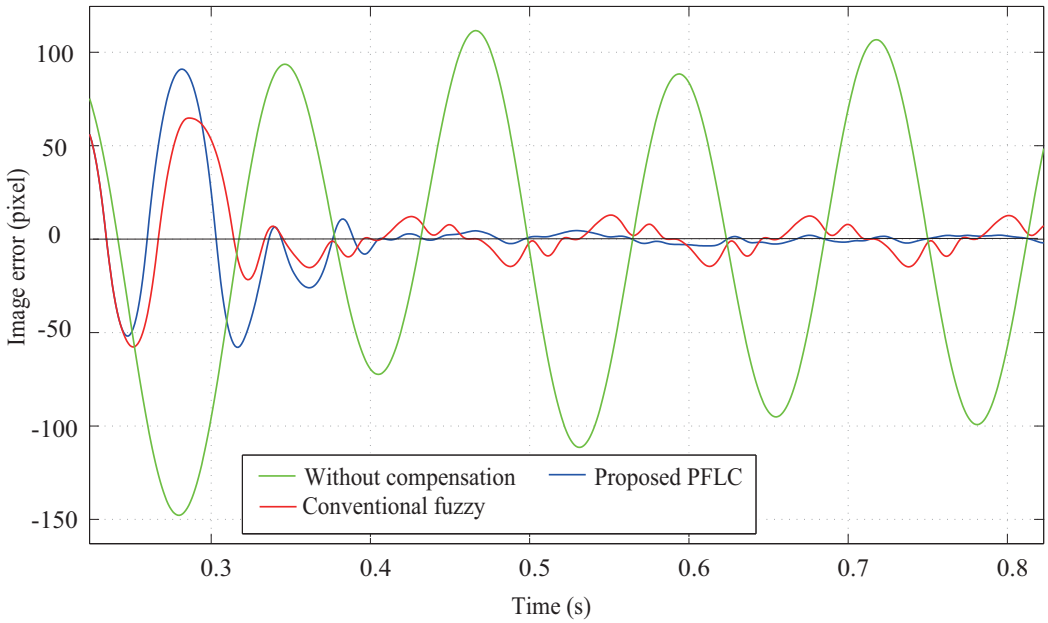

Figure 4.8: Simulation result of image error for vibration (8 Hz) compensation.

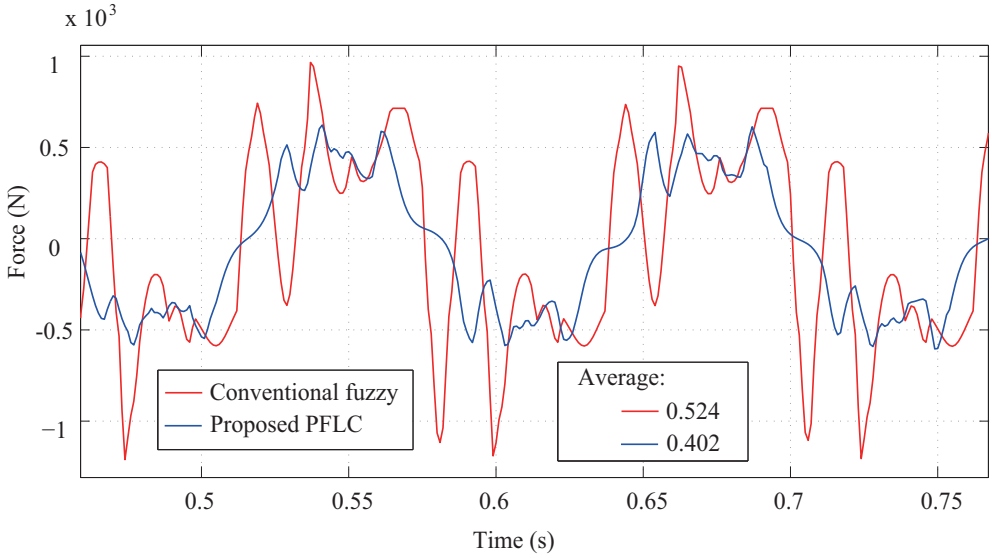

Figure 4.9: Simulation of stimulated force for vibration (8 Hz) compensation.

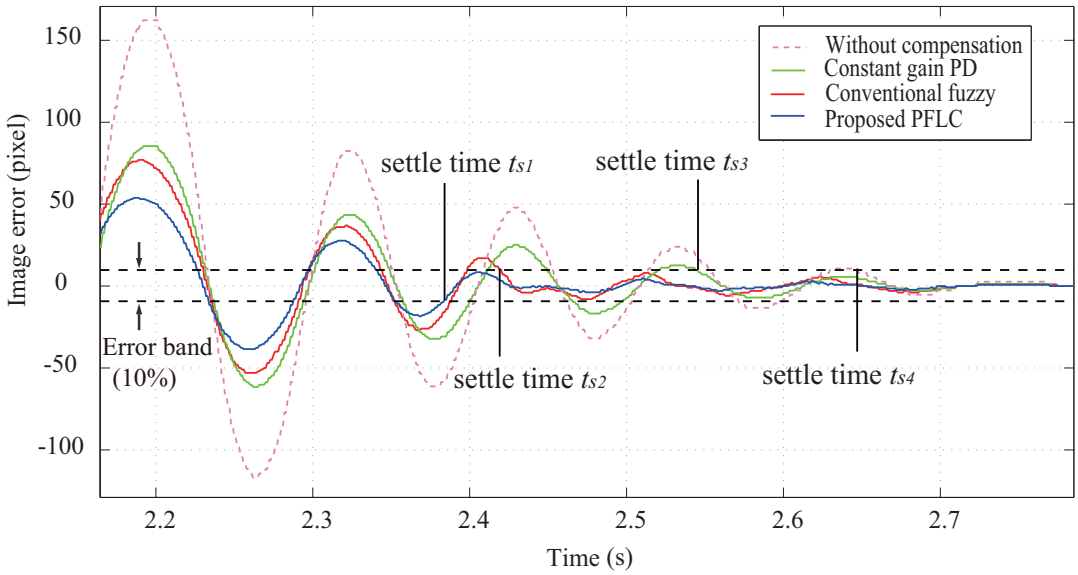

Figure 4.10: Image error for point-to-point compensation.

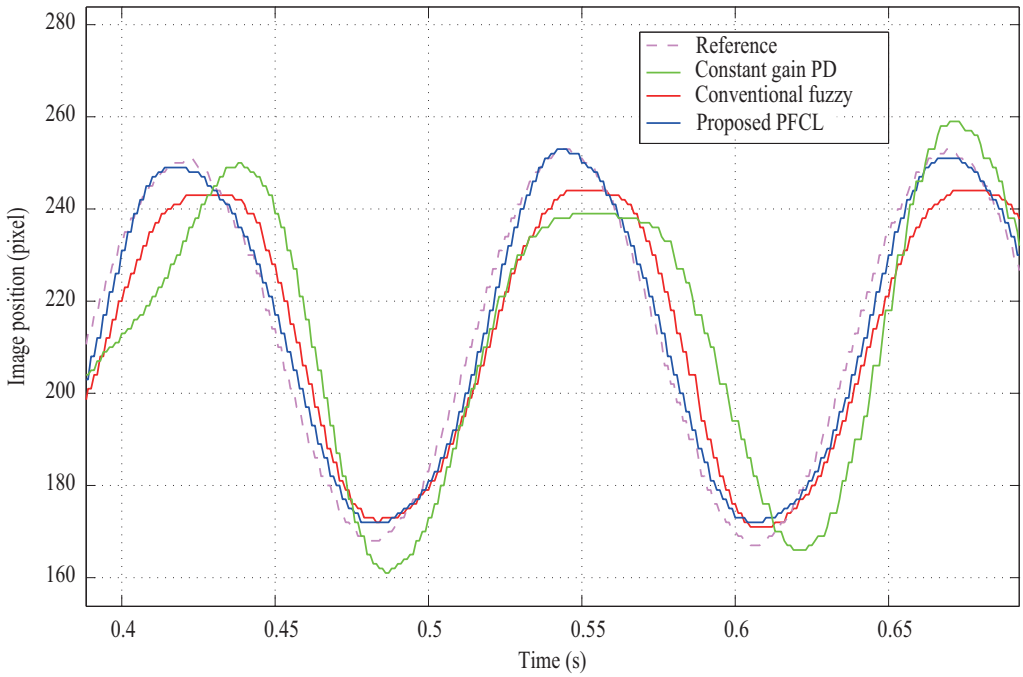

Figure 4.11: Image trajectory for vibration (8 Hz) compensation.

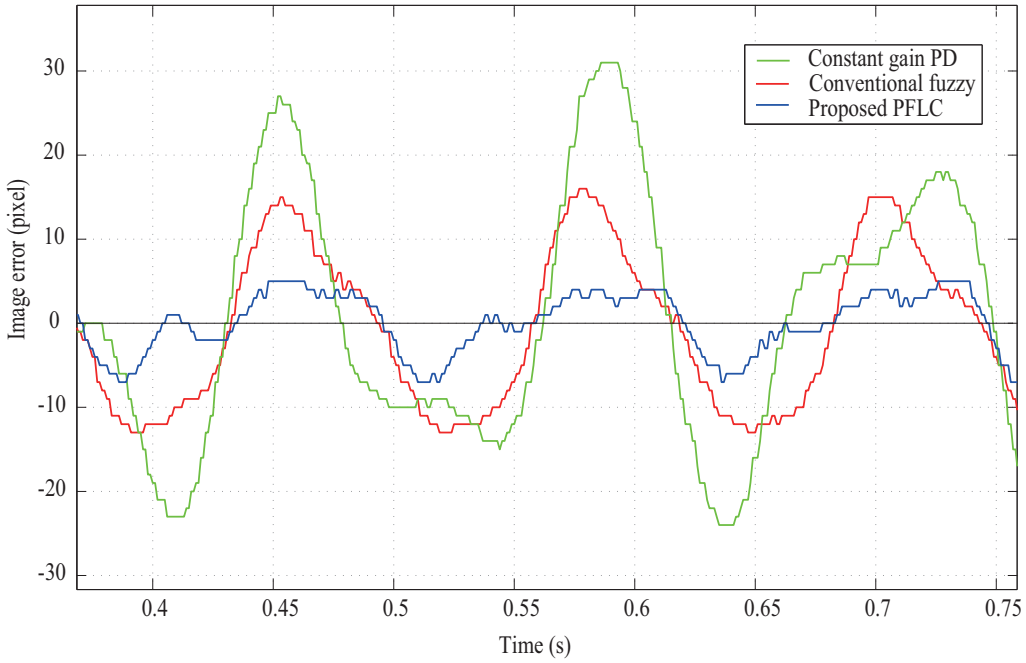

Figure 4.12: Image error for vibration (8 Hz) compensation.

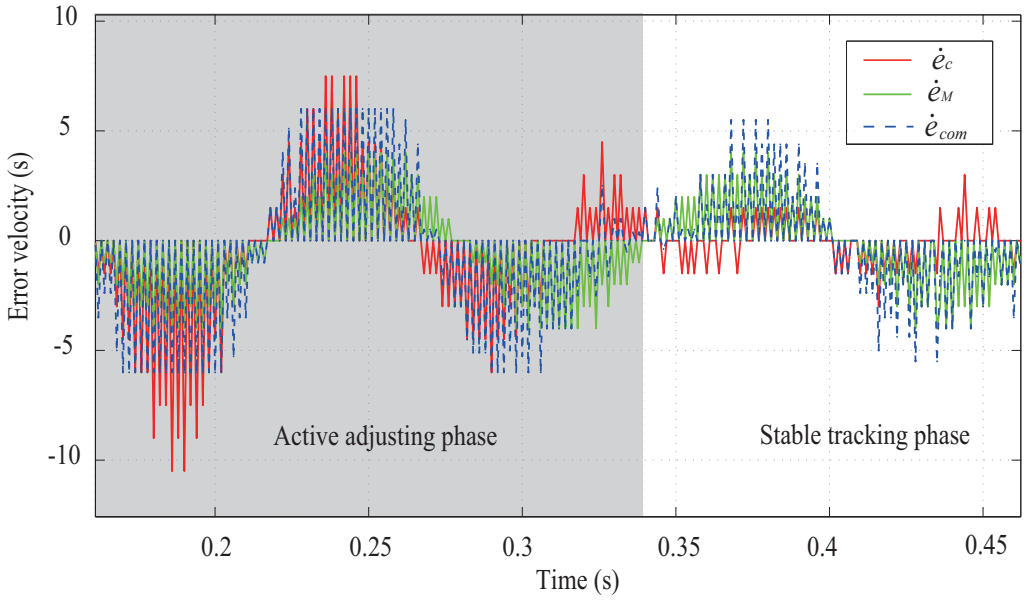

Figure 4.13: Velocity of image error for vibration (8 Hz) compensation.

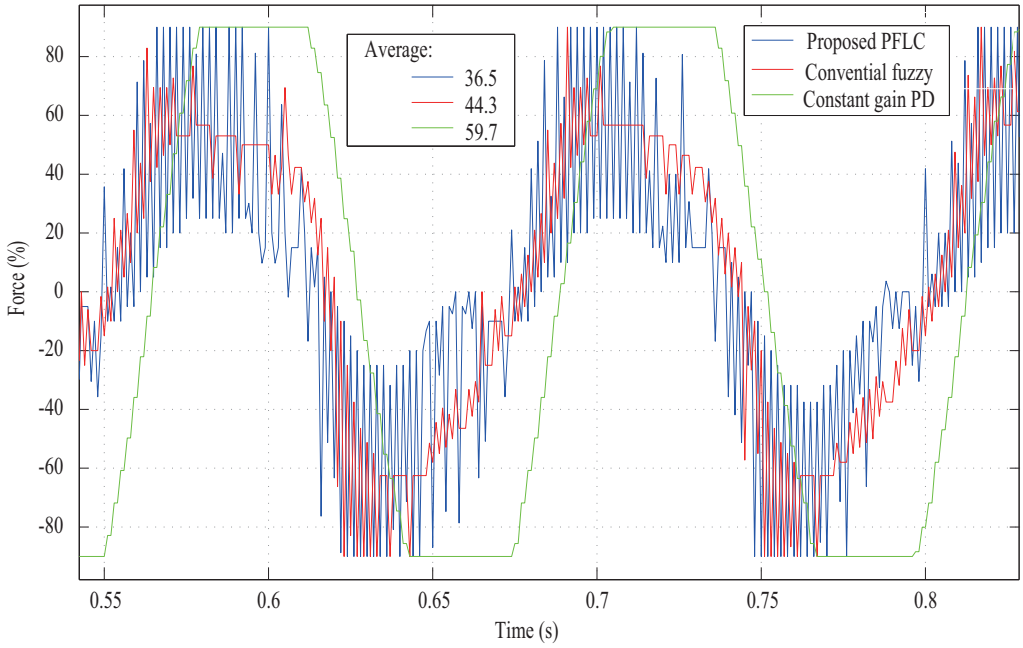

Figure 4.14: Output force for vibration (8 Hz) compensation.

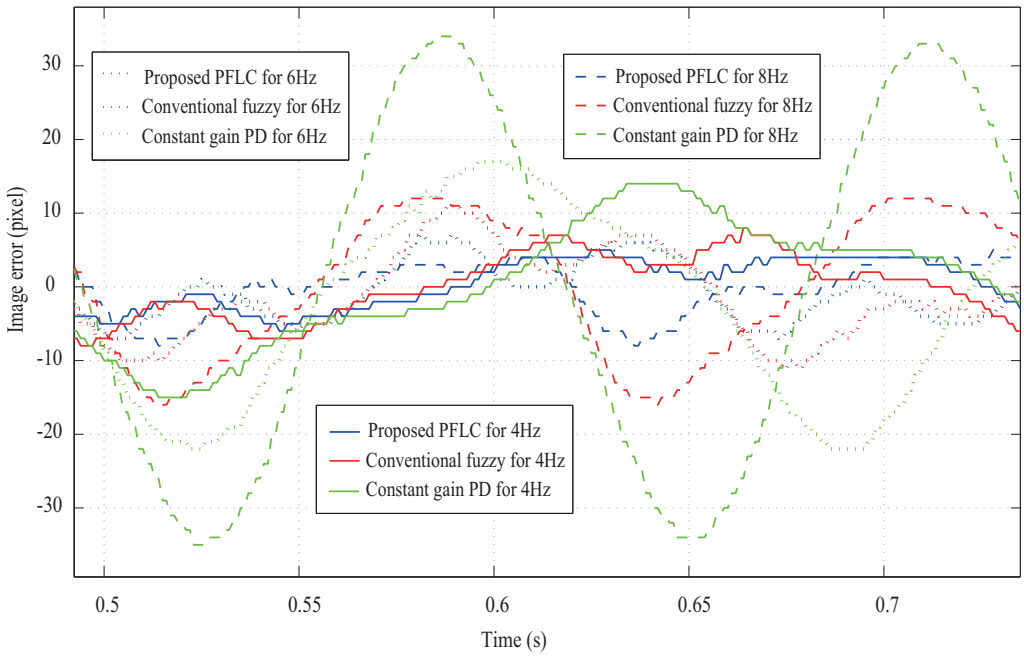

Figure 4.15: Image error for vibration (4 Hz, 6 Hz, 8 Hz) compensation.

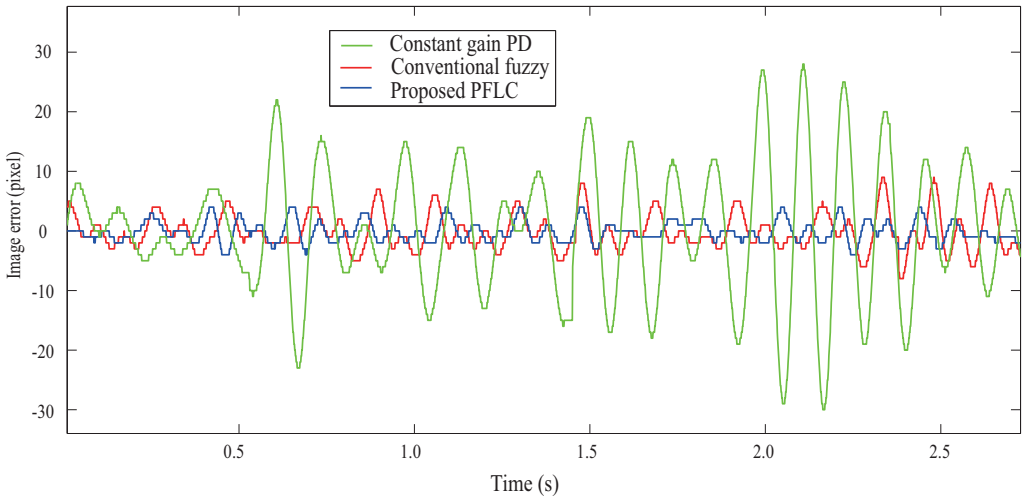

Figure 4.16: Image error for random vibration compensation.

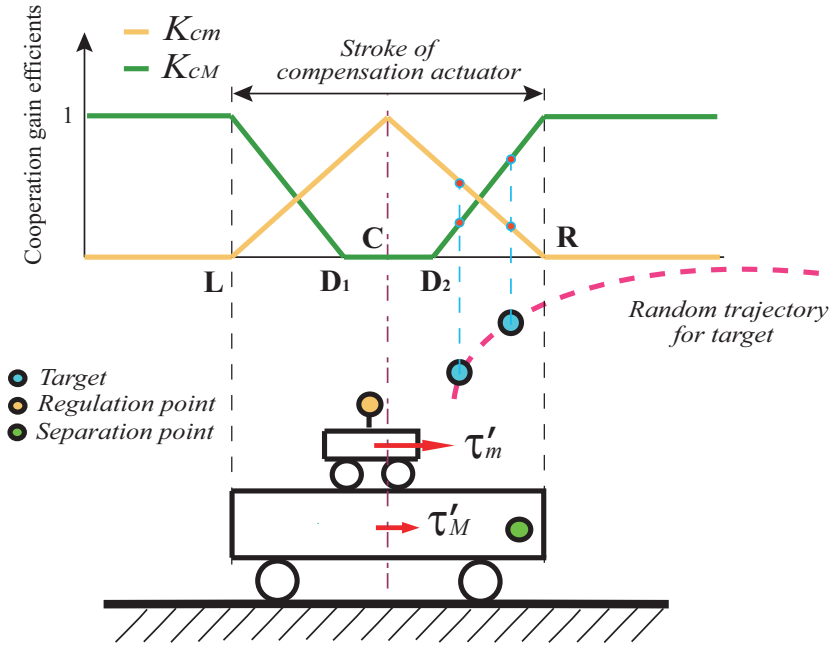

Figure 4.17: Cooperation algorithm for motion planning of the two plants.

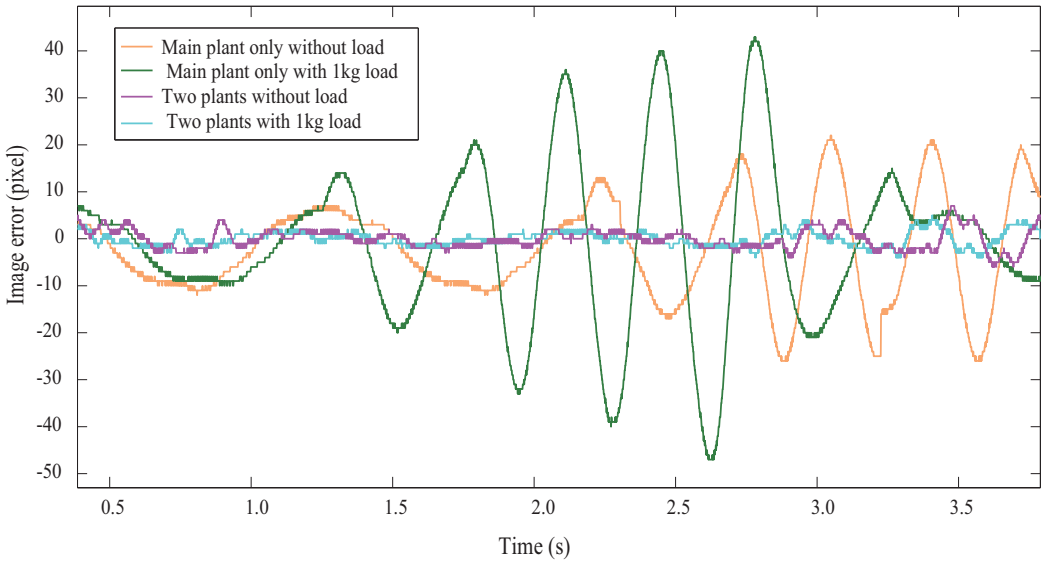

Figure 4.18: Image error for random vibration compensation with extra load.

4.4 Experimental evaluations for dynamic super picking

4.4.1 Experimental settings

Three types of experimental evaluations were conducted to check the performance of the dynamic super picking. Firstly, the main plant was controlled to vibrated with 5 Hz and 8 Hz, with the amplitude smaller than the stroke of the compensation plant, and the target was dropped vertically from a random position that was within the work range of the compensation plant. This was to evaluate the dynamic compensation performance of the compensation plant under the proposed PFLC method. Secondly, the target was dropped vertically from a random position that was out of the compensation plant's work range, and this was to evaluate the picking performance based on the cooperation algorithm and PFLC algorithm. Finally, as a more general case, the target was flying with a initial speed both in horizontal and vertical direction. In order to keep the target flying within the work range of the main plant, a blocking mechanism with the curve shape was configured. Since the initial speed and flying direction was randomly configured, the target would form a random trajectory during flying.

4.4.2 Experimental results

The target can be successfully picked by the compensation plant in most of the time although the main robot was exhibiting high-speed vibrations. Figure 4.19 shows the dynamic picking of two targets (they have been dropped from random positions) with the main plant vibrated under the frequency of 8 Hz.

The target dropped from a random position can be mostly picked by the system, and Figure 4.20 shows the result for one trial. There was only about 190 ms for the system to realize the picking, and thanks to the cooperation motion between the main plant (referred to the curve "u of separation point") and the compensation plant (referred to the curve "u of regulation point"), the target can be caught in time with sufficient accuracy. After evaluations of the free-fall target from different height and different horizontal position (within the camera's field of view), the target can be picked by the system with a success rate of over 90%. Figure 4.24 shows the continuous images of picking the free-fall target from a random height and position.

As shown in Figure 4.22, in order to obtain large field of view by one camera, the camera has been configured in such a way that an angle (about 50°) was formed between its optical axis and the picking net's motion trajectory. A LED marker was adopted to represent the position for the picking net with a small offset from the net center, and the offset would be slightly different in images as

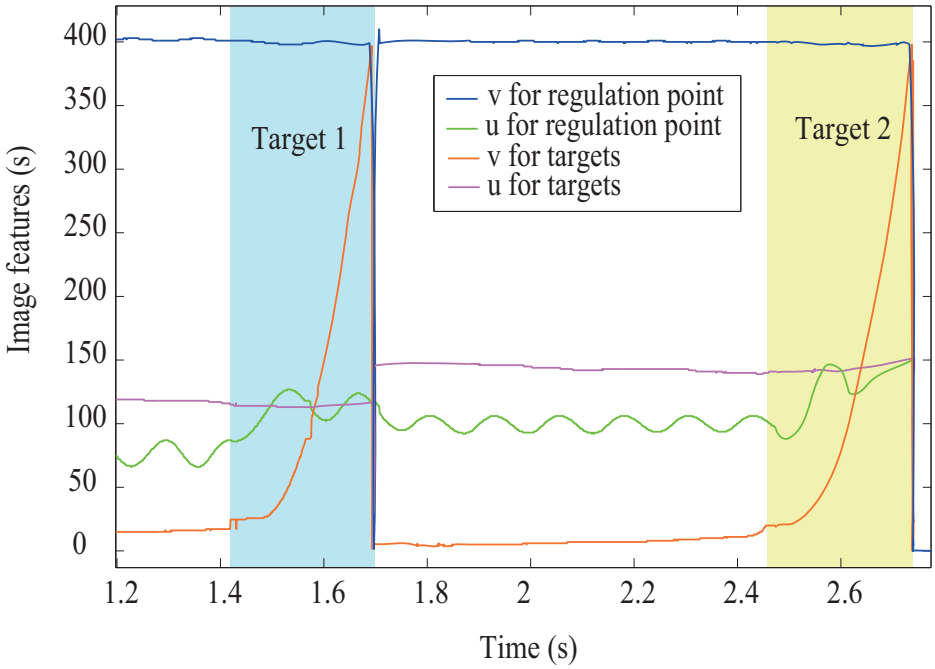

Figure 4.19: Image features for dynamic super picking of two targets (main plant vibrates with 8 Hz).

it was projected from different horizontal positions. Since it is another issue not concerning with the proposed concept for realizing the picking task, we have only conducted a rough calibration for compensating this offset, and obviously this has resulted to the few failure cases of the picking task. A much more accurate calibration or adopting several cameras to enlarge the field of view can solve this problem and further improve the success rate.

As for the evaluations on a flying target, the result for one trial is shown in Figure 4.21. The target was flying with a initial velocity of about 4.3 m/s in horizontal direction, and there was only about 55 ms for the system to realize the picking. After several trials, the success rate for picking a flying object was around 50%, and the failures have been partially resulted from the same reason as above, as well as the reason that the clearance for picking the flying target has become smaller (shown in Figure 4.23). Figure 4.25 shows the continuous images of picking the flying target.

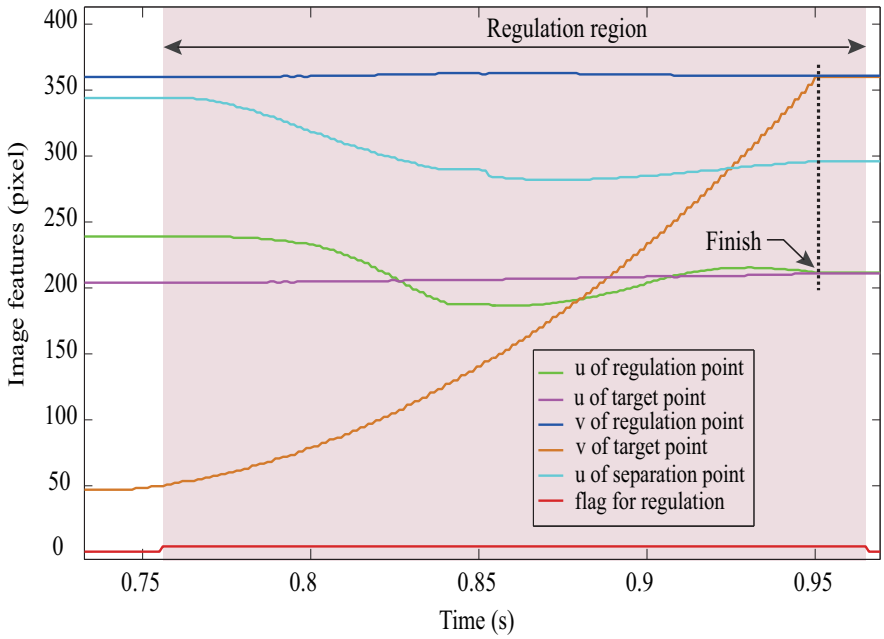

Figure 4.20: Image features for dynamic super picking of a free-fall target.

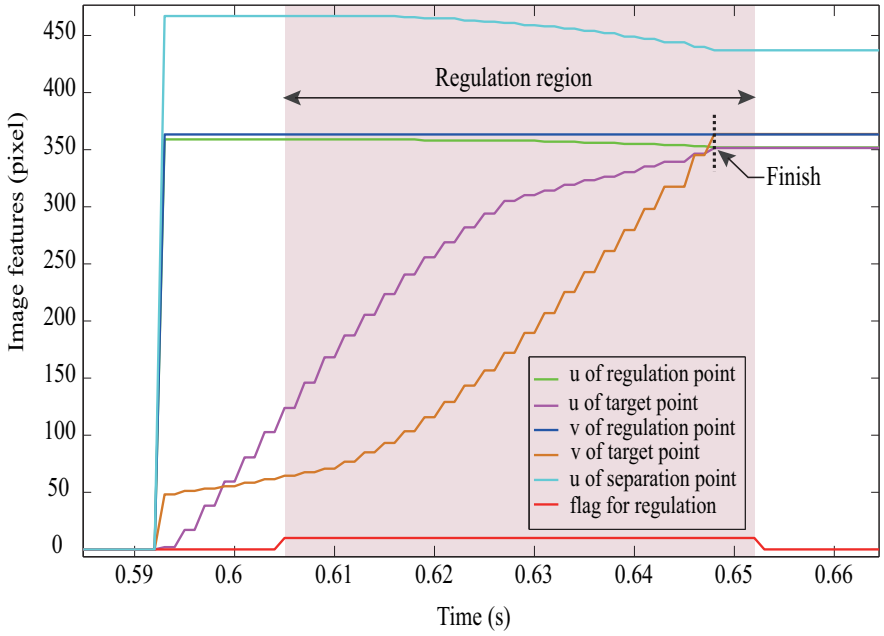

Figure 4.21: Image features for dynamic super picking of a flying target.

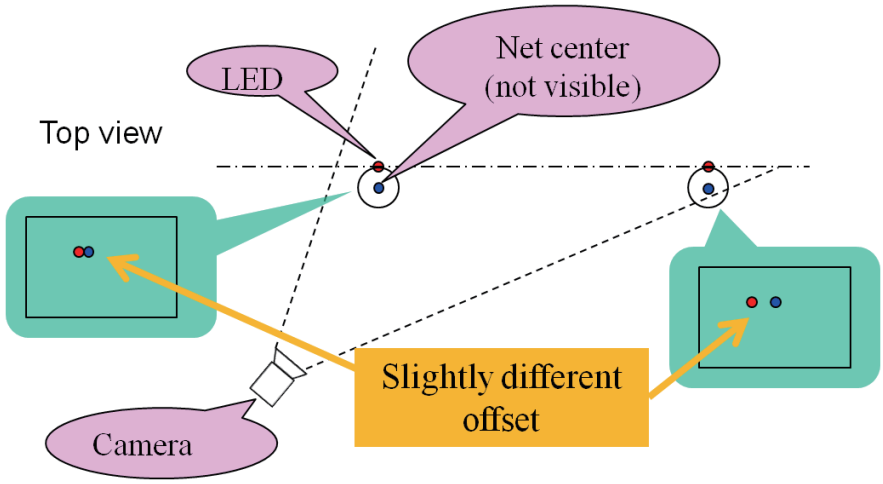

Figure 4.22: Configuration of the camera and the resulting different offset between marker (LED) and net center.

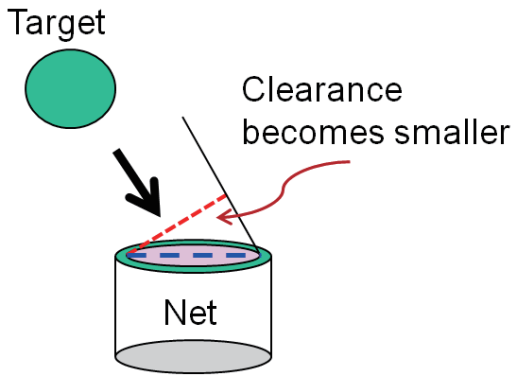

Figure 4.23: Clearance for picking the flying target becomes smaller.

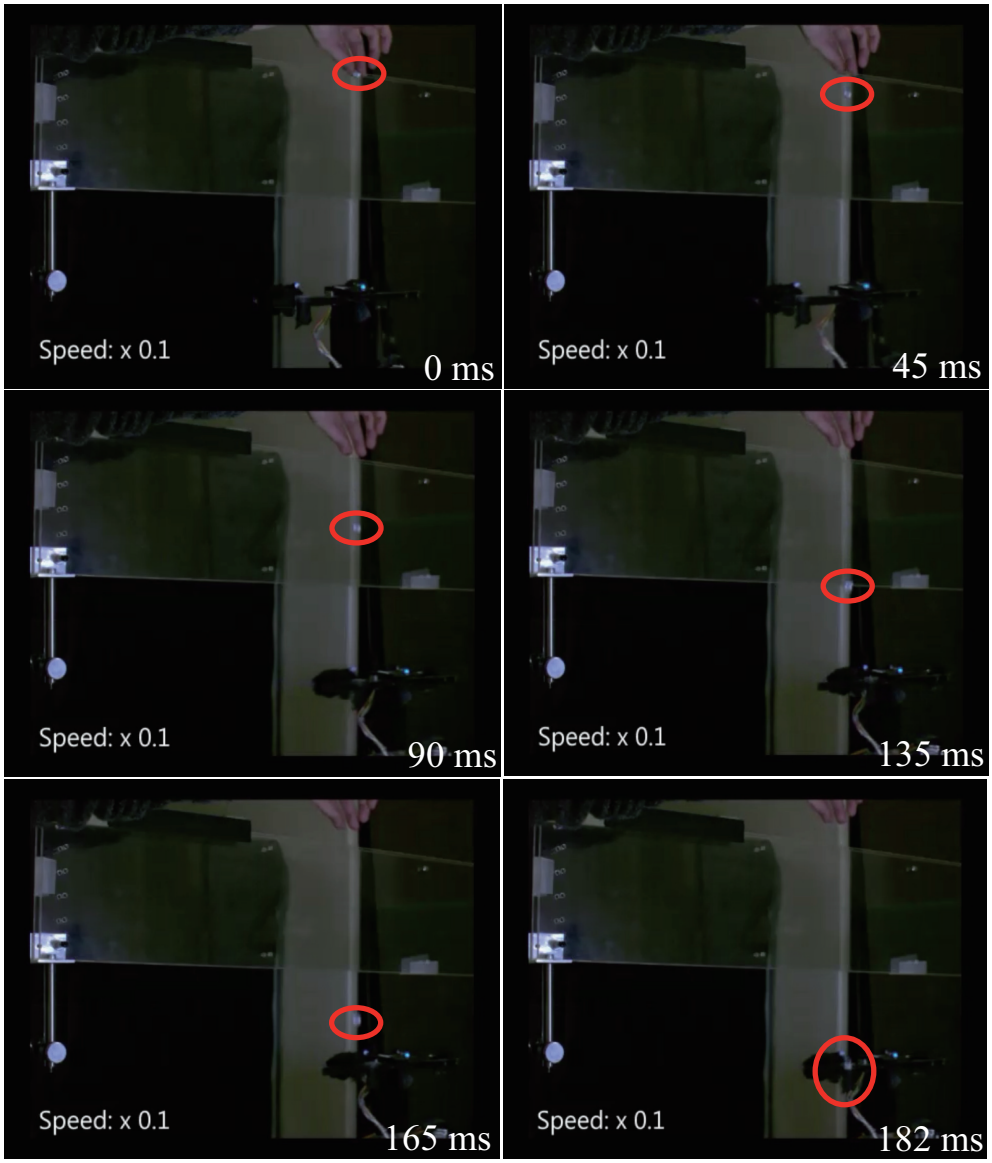

Figure 4.24: Snapshots for dynamic super picking of a free-fall target.

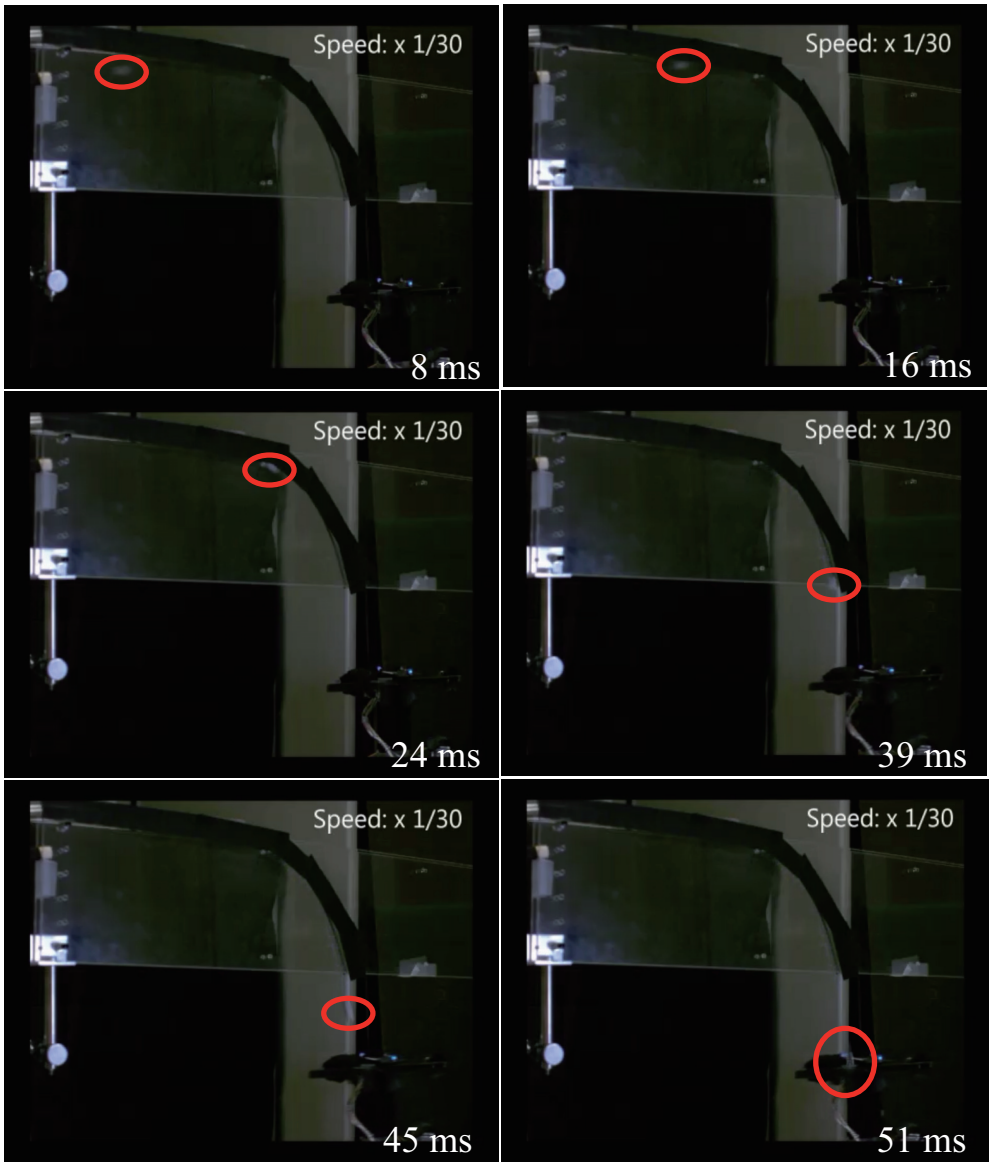

Figure 4.25: Snapshots for dynamic super picking of a flying target.

4.5 Summary of this chapter

In this chapter, the 1D dynamic super picking task realized by the proposed dynamic compensation approach is addressed. The catching or picking a flying target with small clearance is not easy for that not only because of the space accuracy, but also due to the time limitation. With the exploiting of the 1-DOF DCRS, a pre-compensation fuzzy logic control (PFLC) approach has been proposed to realize the better compensation performance by the compensation actuator. With a simple gain adjusting algorithm for two plants, the cooperation between two plants is effectively realized. Through simulation and experimental evaluations, the effectiveness of the PFLC as well as the cooperation algorithm has been verified. It is worthwhile to point out that comparing with the related works based on 3D space information, the proposed approach in this work is all image-based regulation and makes full use of the relative coordinate information between target, compensation plant and main plant. Thus the calibration works for the camera has been greatly reduced, and the performance is much more stable as it is not so dependent on the calibration as the traditional approaches.

Again, if we look back at the Figure 1.5, from the performance of the 1D dynamic super picking task, it is obvious that an excellent score of robotic manipulation has been reached thanks to the dynamic compensation approach.

Here only 1D positioning task has been addressed, in the next chapter we would like to extend the evaluation of the dynamic compensation concept into 3D position as well as attitude regulation. The classical peg-and-hole alignment with large pose uncertainty is a good task for this kind of evaluation.

Chapter 5

3D position and attitude regulation: peg-and-hole alignment

In this chapter, another concrete evaluation task: 3D peg-and-hole alignment with large position and attitude uncertainty will be addressed. In accordance with the dynamic compensation concept, a high-speed active peg will act as the compensation plant to cooperate with the robot arm, which suffers from the dynamics issue under high-speed manipulations. Both the monocular approach and the binocular approach for fast alignment problem will be analyzed.

5.1 Background and problem formulation

Peg-and-hole alignment is a well-addressed topic for autonomous assembly control. There are two issues for realizing a general peg-and-hole alignment, the position alignment and the attitude alignment. Consider a cylindrical peg and a cylindrical hole in the work space $\mathcal{T} = SE(3)$, let φ and ψ represent the heading angle and the pitch angle as shown in Fig.5.1, and if we set the position and attitude of the peg and the hole to be $\boldsymbol{P}(x, y, z), \boldsymbol{H}(x, y, z)$ and $\boldsymbol{P}(\varphi, \psi), \boldsymbol{H}(\varphi, \psi)$ respectively, the alignment problem is the minimization: $\min\{\mid \boldsymbol{P}(x, y, z) - \boldsymbol{H}(x, y, z) \mid + \mid \boldsymbol{P}(\varphi, \psi) - \boldsymbol{H}(\varphi, \psi) \mid\}$. As can be seen, the coupling between the position alignment and attitude alignment exists as a challenging issue for the fast convergence of the alignment process.

Traditionally, peg-and-hole alignment is usually realized by using mechanical compliance (force control) after realizing contact regulation (position control). Force control can be done by passive approaches such as the Remote Center of Compliance (RCC) [81], or active approaches with force/torque sensors [82].

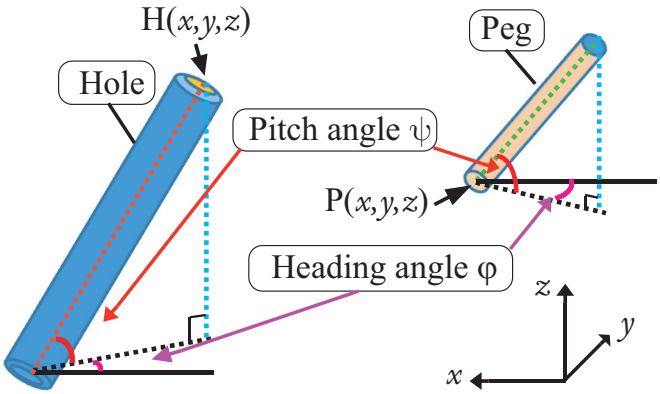

Figure 5.1: Peg-and-hole alignment problem with position and attitude uncertainty

Peg-and-hole alignment realized by visual feedback control also holds many advantages, such as flexibility, compensation for uncertainties of system and workspace, and good tolerance to calibration error. Lately several works addressed the problem of micro peg-and-hole alignment (e.g., [83, 84]). Since micro-assembly requires high accuracy within a small workspace, a globally fixed configuration of cameras is favorable. But in macro assembly with big workspaces and more dynamic uncertainties, the eye-in-hand configuration holds the advantages of higher flexibility, higher accuracy and occlusion avoidance. Yoshimi *et al.* [85] proposed an eye-in-hand approach for peg-and-hole alignment. They showed that rotational invariance could be incorporated into the strategy of peg-and-hole alignment, and an image Jacobian estimation method enables the system to be free of calibration. Their approach holds the drawback that the alignment process was complicated and time consuming. Furthermore, they mainly focused on the position alignment; the attitude alignment between peg and hole was not studied.

Morel *et al.* [86] proposed a strategy for peg-in-hole manipulation with the combination of visual tracking and force compliance control. Their control scheme involves a position based impedance controller with force feedback, and a visual feedback loop to provide the reference trajectory to the impedance controller. The impedance controller and the vision-based controller can be designed separately, and the latter alone can represent the classical image-based visual servoing method for the peg-and-hole alignment problem. However, as the experimental results shown in [86], the modeling error and calibration error would affect the alignment results greatly, and thus the force feedback was needed to compensate for the forces undesirably generated by the 2D visual servoing.

The macro peg-and-hole alignment with position and attitude uncertainty is

a challenging problem not only due to the coupling issue, but also due to the dynamic defects of the robot arm while realizing alignment, especially under high-speed manipulation. In order to tackle this problem, rather than the high accuracy issue as most traditional works have addressed, the issue of convergence speed would be focused in this study. Particularly, the alignment problem to be addressed in this study would only refer to the position control, and we will only adopt the vision sensor to realize it since it won't involve the contact regulation.

As shown in Fig.2.2, the concept of our approach is to compensate for the robot arm's dynamics (or the dynamical effects for interacting with the target) through two aspects. The first aspect is to add a lightweight high-speed actuator to the end of the robot arm. The second aspect is using high-speed cameras to provide with task-space feedback information of the relative pose between robot and target. This concept is useful in cases where the dynamic model of the robot arm is not available while high-speed manipulation is expected.

In the following contents, we try to solve the alignment problem with two approaches: the monocular approach [87], and the binocular approach [45, 88].

5.2 Monocular approach

The purpose of this study is to realize macro peg-and-hole alignment with position and attitude uncertainty through one camera active visual servoing approach. We wish to realize the alignment with easy implementation, less camera calibration and fast convergence. To realize it, we propose a motion separation strategy with adoption of a high-speed active peg as well as a high-speed eye-in-hand camera.

5.2.1 System design

We take the strategy of motion separation and introduce a high-speed 3-DOF active peg. The active peg is controlled to cooperate with the robot arm with the following stipulations:

- The position alignment is realized by the robot arm's image-based set point regulation.
- The accommodating for the attitude in heading direction φ is realized by the robot arm's image-based regulation.
- The active peg is to realize an image-based high-speed attitude adjustment (accommodating for the pitch angle ψ) but with less position change in images.

As noted above, the robot arm's motion is separated into set point position regulation (by robot arm's joint 1 - joint 3 as shown in Fig. 5.2) and attitude regulation for the heading angle (by robot arm's joint 4). The robot arm's set point control is realized by a simplified image-based visual servoing (IBVS) approach, which is depth-independent, easy to calculate and suitable for high-speed regulation. For the control of robot arm's joint 4, a new image feature is introduced for regulation.

In accordance with our concept shown in Fig.2.2, we designed the system for peg-and-hole alignment study as shown in Fig.5.2. The system consists of a 4-DOF high-speed robot arm, an active peg and one high-speed cameras. One high-speed Eosens vision system is configured as eye-in-hand with an image resolution of 720×720 pixels and a feedback rate of 1000 Hz. An angle of about 20° is configured between the heading direction of the peg and the eye-in-hand camera on the horizontal plane. The high-speed camera is configured to observe both the hole and the peg, thus the system falls into the endpoint closed-loop (ECL) category [8]. The lightweight active peg is realized by a high-speed 3-DOF (two rotational and one prismatic joints) finger with the peg attached to it, and with a weight of about 0.17 kg. The two rotational joints are for attitude alignment, and the prismatic joint is for the insertion after alignment.

5.2.2 Motion planning

For the high-speed vision, since the interval time between two image frames is very small, the image features in these two images differ little for a given target. This is useful for image processing and for feedback control.

5.2.2.1 Set point regulation for the robot arm

The set point regulation of the robot arm is realized with the simplified IBVS approach as have described in Chapter 3 (please refer to section 3.1). Note that, in doing position alignment, the depth error should be estimated. We estimate depth error by taking advantage of the scale invariant property of features in images. That is, after the peg and hole alignment finishes, the ratio between peg's length and hole's length in images is almost the same as the physical one. Let the length for peg and hole in images to be ξ_p^l, ξ_h^l respectively. With our active peg (which performs attitude alignment very sensitively) we estimate the depth error err^{dep} (with the reference to be ξ_{ref}^d) as:

$$err^{dep} = \xi_t^d - \xi_{ref}^d = k_m \cdot (\frac{\xi_h^l}{\xi_p^l} - ratio) \tag{5.1}$$

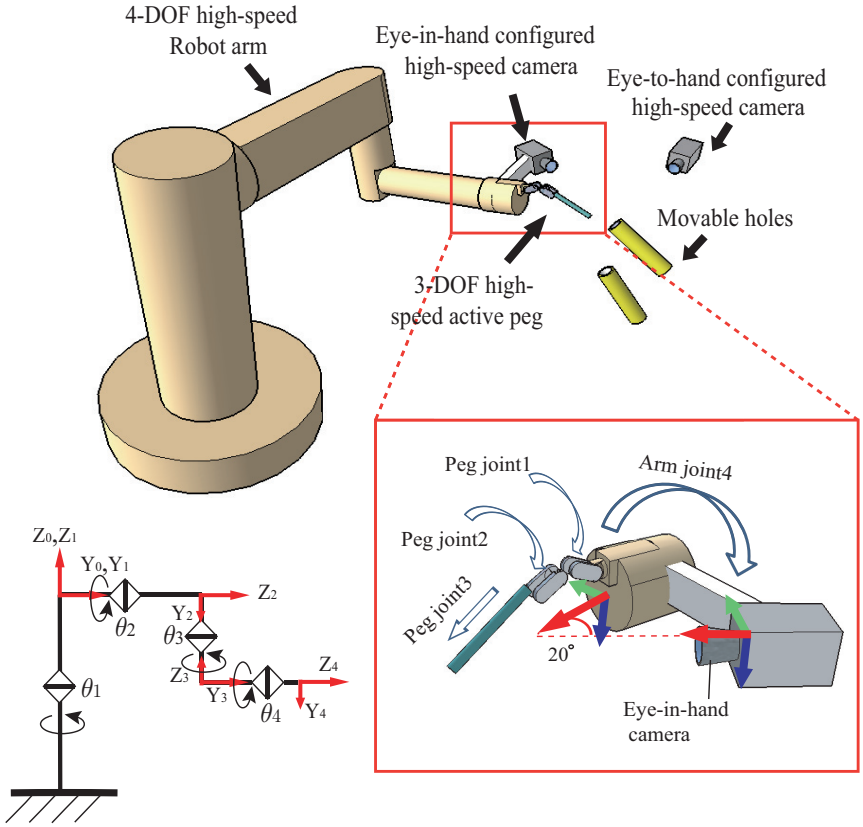

Figure 5.2: System configuration

Where k_m is the normalizing factor and *ratio* is the physical ratio between hole's length and peg's length which are measured ahead of time.

It should be pointed out that in the simplified IBVS approach described above, we only use a coarse kinematic model of the eye-in-hand camera, whereas the depth estimation method of an eye-in-hand camera through motions needs an accurate kinematic model.

5.2.2.2 Regulation of attitude in the heading direction

The robot arm's joint 4 (as shown in Fig. 5.2) is adopted to fit for the arbitrary heading angle of the hole. Let's refer to this joint as the attitude accommodating joint.

In order to regulate the attitude accommodating joint, we introduce a new image feature $\xi_{head} \in \mathbb{Z}^1$, which is defined as the ratio between hole's length

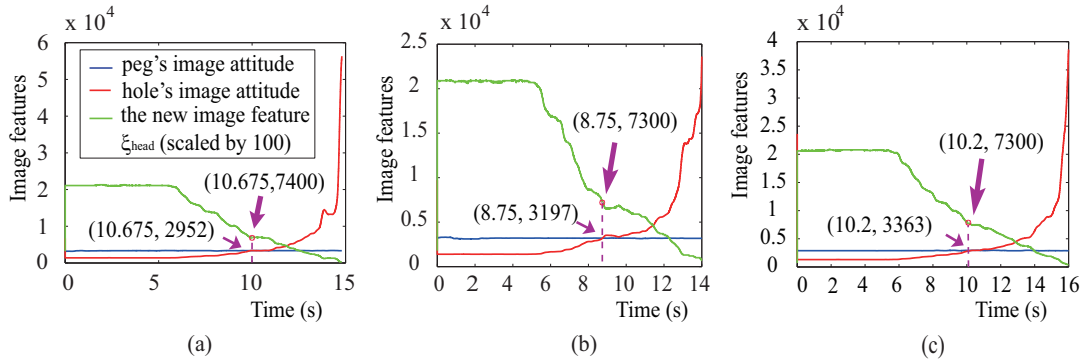

Figure 5.3: Tests of ξ_{head} under different configurations of the hole

$\xi_l^h \in \mathbb{Z}^1$ and its attitude value $\xi_{att}^h \in \mathbb{Z}^1$ in images:

$$\xi_{head} = \xi_l^h / \xi_{att}^h \tag{5.2}$$

where ξ_l^h is defined by the Manhattan distance between the hole's two endpoints in images, and ξ_{att}^h is defined as

$$\xi_{att}^h = \delta v / \delta u \tag{5.3}$$

with $\delta v, \delta u$ the image coordinate differences between the hole's two endpoints in ξ.

Let us check the new image feature ξ_{head} under different pose of the hole. With the condition that the pitch angle as well as 3D position alignment between peg and hole has been calibrated, we rotate the attitude accommodating joint. As Fig. 5.3 shows, with the attitude accommodating joint's rotation, the hole's attitude changes in images and a different pose of the hole will need a different rotation angle for alignment. When the attitude for peg and hole reaches the same value, the corresponding value of the new image feature is recorded. We could see that in three situations, the value of ξ_{head} is 74, 73 and 73 (with normalized unit). As a matter of fact, after we conducted more tests with different heading directions of the hole, we still found that ξ_{head} varied around 73 with small errors. Although here we will omit the strict deviation of this approximately invariant parameter, we adopt ξ_{head} as the image feature for the regulation of the attitude accommodating joint to deal with different heading direction of the hole. However calibration for ξ_{head} is needed.

5.2.2.3 visual servoing for active peg

The peg's attitude alignment is referred to the pitch angle ψ as shown in Fig. 5.1, and the heading angle φ of the hole is accommodated by the arm's joint 4. Due to

the configuration of the camera (Fig. 5.2), as the two rotational joints of the active peg rotate, the horizontal movement of the peg's endpoint would be scaled by $\sin(20°)$ in images. This arrangement is in accordance with the alignment strategy of controlling the peg to adjust the attitude in the pitch direction rapidly and with less position change in images.

The position of peg's endpoint and the peg's attitude on image plane are defined as $\boldsymbol{\xi}_1 = (\xi_x, \xi_y)^T$, $\xi_2 = \xi_{att}$, and the Cartesian position of the peg's endpoint is defined as $\boldsymbol{x} = (x, y, z)^T$, and let $\boldsymbol{\theta}$ be the joint angles. Using the perspective projection function $f(\cdot)$, we have $\boldsymbol{\xi}_1 = f_1(\boldsymbol{x})$ and $\xi_2 = f_2(\boldsymbol{\theta})$. With the kinematics of the finger structure, we write an expression for the tip of peg as $\boldsymbol{x} = g(\boldsymbol{\theta})$.

By differentiating,

$$\dot{\boldsymbol{\xi}}_1 = \frac{\partial f_1}{\partial \boldsymbol{x}} \frac{\partial g}{\partial \boldsymbol{\theta}} \dot{\boldsymbol{\theta}} \equiv \boldsymbol{J} \dot{\boldsymbol{\theta}} \tag{5.4}$$

Here $\boldsymbol{J}$ is the Jacobian matrix. Then the visual servoing control strategy is to solve the problem of $\min\{\mid \xi_{att} - \xi_{att}^{ref} \mid + \mid \xi_y \mid\}$ for the given reference attitude ξ_{att}^{ref}. We solve this problem by applying a gradient step approaching method with inverse kinematics. That is, for a step motion $\delta\xi_x$, the change of the attitude in images with the condition of $\delta\xi_y$ equals zero would be:

$$\dot{\xi}_2 = \frac{\partial f_2}{\partial \boldsymbol{\theta}} \boldsymbol{J}^{-1} [\delta\xi_x, 0]^T \tag{5.5}$$

Since we adopt a recursive step approaching method, we needn't to know the actual model of the perspective projection f_1 or f_2, and instead of the actual Jacobian matrix, we use the kinematic Jacobian $\boldsymbol{J}_k$ for calculation, then the input would be $\boldsymbol{J}_k^{-1}[\delta\xi_x, 0]^T$ for each adjusting step. After adjusting, we compare with the hole's attitude in images to judge whether the attitude adjustment process has converged or not with the set accuracy.

The attitude adjustment procedure above has been realized with an open loop. Taking into account of the dynamics of the mechanism system, we take the error $\Delta\xi_y$ induced by the last step into the next adjustment to form a closed loop. The regulation would be:

$$\dot{\xi}_2 \simeq \boldsymbol{J}_k^{-1} [\alpha \cdot \delta\xi_x, -(1-\alpha) \cdot \Delta\xi_y]^T \tag{5.6}$$

where α is a gain factor which can vary between 0 and 1. The algorithm for visual servoing control of the active peg is summarized in Algorithm1.

Algorithm 1: Visual Servoing For Active Peg

$StepSize \leftarrow \delta\xi_x$;
$\xi_{att} \leftarrow$ getPegImageAngle();
$Initial \leftarrow \mid \xi_{att} - \xi_{att}^{ref} \mid$;
$\boldsymbol{\theta} \leftarrow$ getJointAngle() ;
$\boldsymbol{\theta} \leftarrow \boldsymbol{\theta} + \boldsymbol{J}_k^{-1} \cdot [\alpha \cdot StepSize, 0]^T$;
$\xi_{att} \leftarrow$ getPegImageAngle();
if $\mid \xi_{att} - \xi_{att}^{ref} \mid > Initial$ **then**
  StepSize $\leftarrow -\delta\xi_x$;
end
while $\mid \xi_{att} - \xi_{att}^{ref} \mid > ACCURACY$ **do**
  $\Delta\xi_y \leftarrow$ getPegImagePosition();
  $\boldsymbol{\theta} \leftarrow$ getJointAngle() ; $\boldsymbol{\theta} \leftarrow \boldsymbol{\theta} + \boldsymbol{J}_k^{-1} \cdot [\alpha \cdot StepSize, -(1-\alpha) \cdot \Delta\xi_y]^T$;
  $\xi_{att} \leftarrow$ getPegImageAngle();
end

5.2.2.4 peg-and-hole alignment

A two-step alignment algorithm

On basis of the motion separation strategy, we use a two-step visual servoing procedure for the alignment in order to realize a fast convergence.

As shown in Fig. 5.4, the first step is to control the arm to center the hole in images. Meanwhile, the peg adjusts the attitude to be aligned with the hole's pitch angle for the initial phase. We start with peg's endpoint (in a ready position) in the upper side of images, which enables the next step of position and attitude alignment to be done within a relatively small range.

Also, since the peg's regulation for the attitude alignment will change the peg's length in images, we will limit the peg's adjustment during the depth regulation to avoid unnecessary oscillations. We adopt a threshold value H_d for the depth error err^{dep}. After the peg and the hole have realized attitude alignment for the initial phase, the peg's regulation will be disabled until err^{dep} becomes smaller than H_d, and this will also trigger the alignment process to enter into the next step.

In the next step, the hole's position is regulated to reach the peg's endpoint. Note that during this step, the attitude regulation by the active peg and the regulation of the 3D position due to the robot arm will operate simultaneously, and the active peg is more sensitive than the arm. As for the 3D position regulation, in order to avoid the overlaid between peg's marker and hole's marker in images before converge, we take a balance between depth regulation and image plane

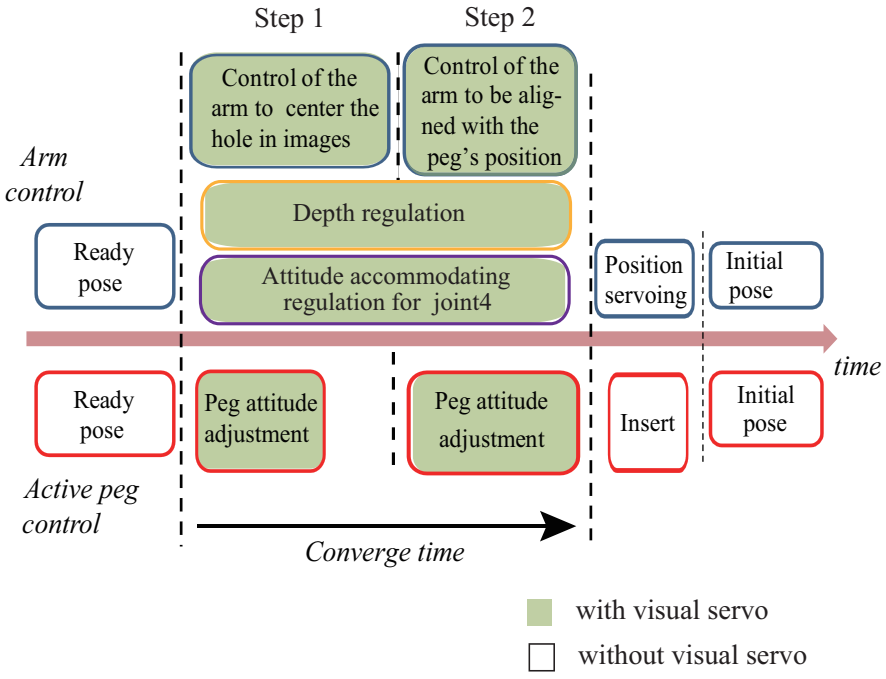

Figure 5.4: The two-step peg-and-hole alignment algorithm

regulation with the following constraint:

$$\boldsymbol{err}^{posi} = \boldsymbol{\xi} - (\boldsymbol{\xi}_1 + k_e \cdot \mid err^{dep} \mid) \tag{5.7}$$

where, $\boldsymbol{err}^{posi}$ is the position error, $\boldsymbol{\xi}$ is the hole's image position, $\boldsymbol{\xi}_1$ is the peg's image position, and k_e is a gain factor (ranging from 0 to 1) to control the static error. With this constraint, the depth regulation and image plane regulation realize convergence at the same time.

Convergence criterion

In summary, we use four image features to judge whether the alignment between peg and hole can converge. These are: the image position error $\boldsymbol{err}^{posi}$, the depth error err^{dep}, the attitude error of the pitch angle err^{att}, and the attitude error of the heading angle err^{head} regulated by the attitude accommodating joint. All of these image feature errors are regulated with PD control. When all of these four image feature errors enter the convergence range, the active peg's insertion into the hole will be triggered.

5.2.3 Experimental evaluations

The active peg's outside diameter was 10 mm, and the hole's inner diameter was 14 mm. We set the stroke of the insertion for the peg into the hole to be 20 mm. For both peg and hole, two markers made of light-reflecting material were fixed on the end part, and the image processing algorithm calculated the moment feature for each marker to generate peg's and hole's image position, tilt angle, and the length information in image coordinates. We set the length for hole and peg to be 40 mm and 24 mm respectively; the ratio of the two was about 1.67. We fixed the hole's pitch angle ψ without knowing its physical value and then put the hole to be an arbitrary heading angle and position within the robot arm's workspace.

As Fig. 5.4 shows, the converge time for alignment is defined from the ready pose to alignment realized. The preparation time to reach the ready pose from the initial pose was set to be 5 s and the insertion time was 1 s.

Fig. 5.6 shows the process of the peg-and-hole alignment for one configuration of the hole with two different point of view. The position and attitude alignment was realized at 1.75 s (excluding the preparation time), and the insertion realized at 1.81 s.

As shown in Fig. 5.5(a), the peg's position realized alignment with the hole's position in image coordinates, and as Fig. 5.5(d) shows, the depth control was also converged to the reference value that we have set to be the ratio between the hole's length and the peg's length. Fig. 5.5(b) shows the attitude regulation for the pitch angle realized convergence. Fig. 5.5(c) shows the regulation of the heading attitude, it also reached the reference value.

Fig. 5.5(e) shows the trajectory of both peg and hole during the alignment process in images. Both in Fig. 5.5(a) and Fig. 5.5(e) show that with the active peg's regulation, the peg's attitude could realize alignment with its position changing within a small range, which contributed to the position alignment's convergence.

In the experiment, for the unknown configured hole, the success rate of the alignment (insertion of the peg into the hole successfully conducted) was about 65%, with an average time within 2 s.

5.2.4 Discussion

During the experiment, we found that the depth regulation for the robot arm was a key aspect for resulting. The depth information represented by the ratio between hole's length and peg's length in images is relatively vulnerable to the noise, as could be seen in Fig. 5.5(d), and most of the failed cases were due to the misalignment of robot arm's set point control in the depth regulation. As a matter of fact, the simple ratio we have adopted would be an invariant under the

affine transformation, whereas in our case, the camera model could hardly fit for the affine model. Since during the experiment, we didn't change the pitch angle of the hole too much, we still can make use of it to get a relatively stable result. In order to improve the success rate, we can take the method of modifying the ratio value through the off-line calibration, or combine with another sensor to make the accurate inspection of the depth error.

From the experiment, we also found that during the alignment process, the regulation step1 always took a longer time than step2. For example, as for the alignment in Fig. 5.6, the first step was finished at about 1.25 s, and step2 only consumed 0.5 s. We think this may be partially attributed to the set point regulation algorithm for the robot arm, since it did not follow an optimal trajectory.

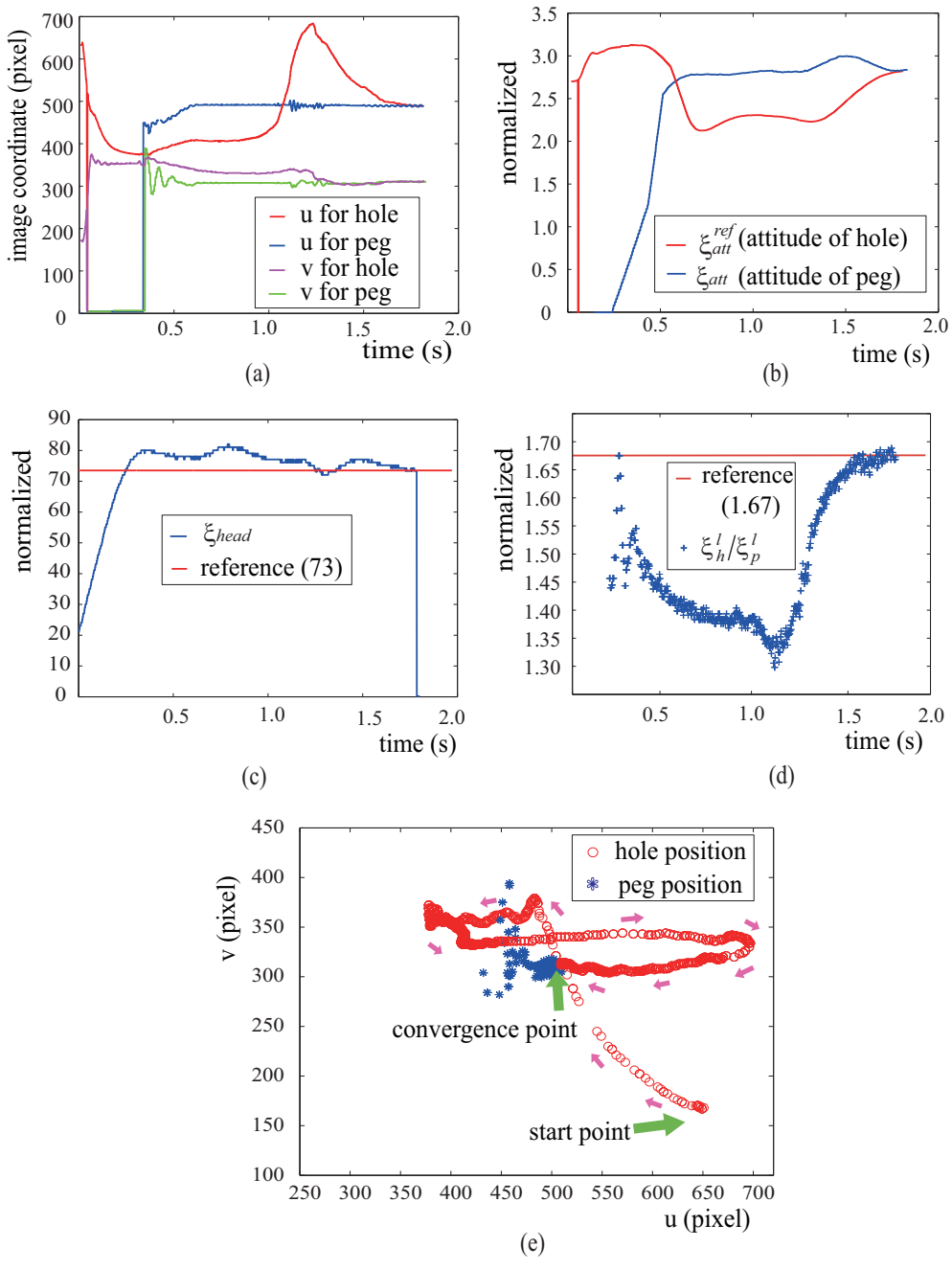

Figure 5.5: Image features of alignment process

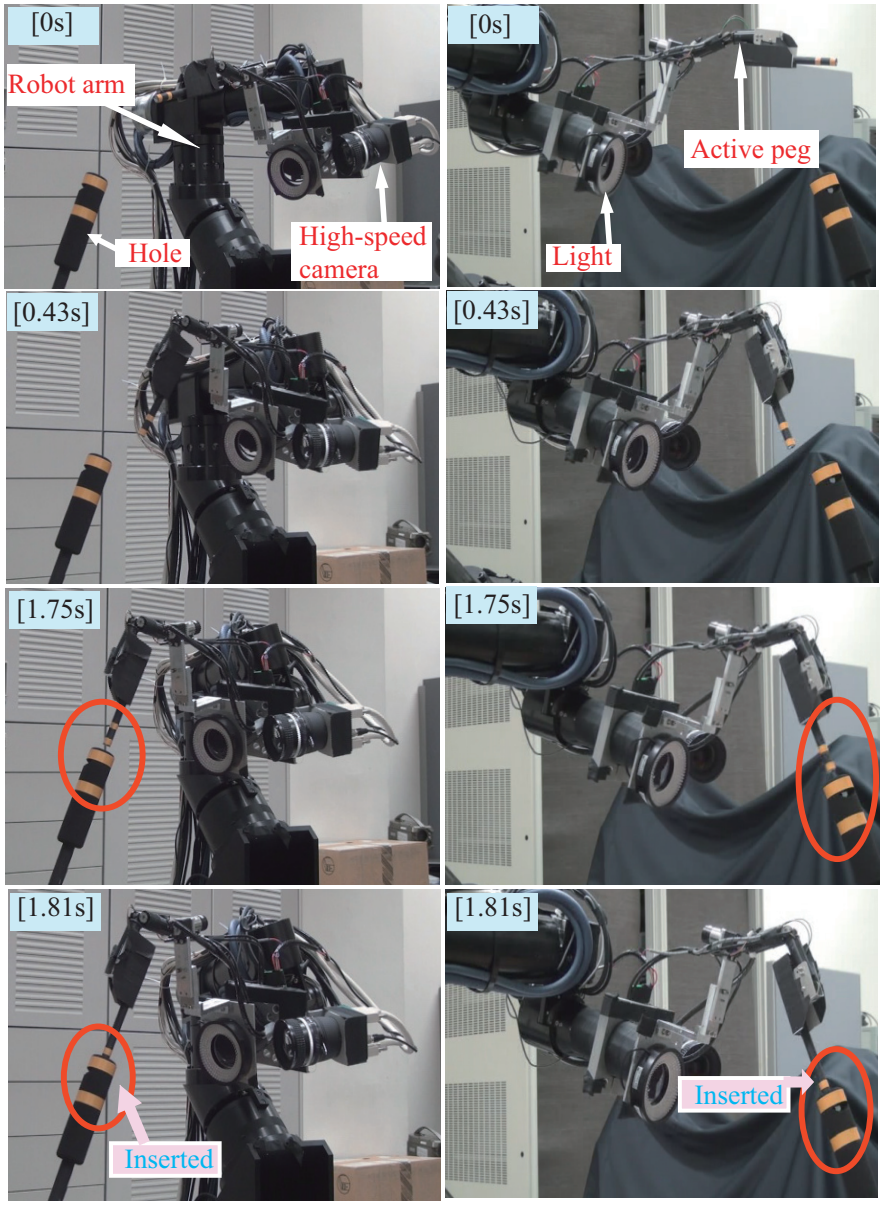

Figure 5.6: Continuous snapshots of alignment process

5.3 Binocular approach

Compared to the monocular approach described above, we propose a much more compact binocular approach by exploiting a visual compliant motion strategy for the fast peg-and-hole alignment problem (with large initial errors). Of course, we follow the dynamic compensation concept by adopting of a high-speed 3-DOF active peg cooperating with the robot arm, which is the same as the monocular approach.

Inspired by the so-called visual compliance control [89], this approach focus on the realization of fast macro peg-and-hole alignment with position and attitude uncertainty through visual feedback only, without the position compensation from force-feedback control, and of course without the computation of the insertion trajectory in advance. Castano *et al.* [89] proposed the task-level visual compliance control with a hybrid vision/position control structure. Visual compliance is analogous to physical compliance, as the robot's end-effector maintains contact with a visual constraint surface, and visual compliant motion moves the end-effector along a projection ray that passes through the focal center of the camera.

5.3.1 System design

The designed system for binocular approach is almost the same as the monocular as shown in Fig.5.2, except that one more eye-to-hand high-speed camera is configured to provide more information between the peg and the hole. For the better clarify, hereafter we will refer to the eye-in-hand camera's frame as Σ_{ci} with its image plane ξ, and the eye-to-hand camera's frame as Σ_{ct} with the image plane ζ.

5.3.2 Alignment methodology

Consider a static hole with position and attitude uncertainty, the robot should guide the peg to realize the alignment with the hole's position and attitude. As for the conventional methods of peg-and-hole alignment, since the peg is a fixed tool on the robot arm, it's not easy to realize a fast and accurate alignment. Not only do the dynamics of the robot arm cause unwanted effects, but also, the adjustment of the position and attitude are coupled, which is not good for fast convergence.

In this study, we present a visual compliance strategy with adoption of a 3-DOF high-speed active peg to deal with this problem, and we intend to realize a fast peg-and-hole alignment manipulation. There are three visual constraints to effect the corresponding visual compliant motions:

- Co-point constraint in images (eye-in/to-hand camera) for the peg and the hole. This visual compliant motion is effected on the robot arm. Hereafter we define the word "Co-point" as: two points located on the same image plane with a sufficiently small distance. As shown in Fig.5.7(a), the hole's endpoint $\boldsymbol{H}(x, y, z)$ and the peg's endpoint $\boldsymbol{P}(x, y, z)$ should be controlled to be aligned on $\boldsymbol{\xi}_{end} \in \mathbb{Z}^2$ in image plane ξ. Since during the first stage of the alignment, the peg will be motionless, and this constraint is actually to effect the visual compliant motion for the robot arm along the projection ray formed by $\boldsymbol{H}(x, y, z)$ and $\boldsymbol{\xi}_{end}$.
- Line-parallel constraint in images (eye-in-hand camera) for the peg and the hole, which corresponds to the plane parallel constraint in Cartesian space. This visual compliant motion is effected on the robot arm. As shown in Fig.5.7(a), the active peg moves within the plane of σ. The center line of the hole in Cartesian and in image form the plane of π, and the center line of the peg in Cartesian and in image form the plane of μ. In order to keep μ and π to be parallel, the center line of the hole and the peg should be parallel in the image plane. This constraint actually realizes the alignment in the direction of the heading angle φ as illustrated in Fig.5.1. The robot arm's joint4 (Fig.5.2) will be controlled by this visual constraint to effect the visual compliant rotational motion.
- Co-point constraint in images (eye-to-hand camera) for the peg and the hole. This visual compliant motion is effected on the active peg. As shown in Fig.5.7(b), once the hole's endpoint $\boldsymbol{H}(x, y, z)$ and the peg's endpoint $\boldsymbol{P}(x, y, z)$ reach the same position $\boldsymbol{\zeta}_{end} \in \mathbb{Z}^2$ in the eye-to-hand camera's image plane ζ, the active peg should be controlled to keep on the position $\boldsymbol{\zeta}_{end}$ and looks like "motionless" while the robot arm is still moving under the other two visual constraints. This is to accommodate for the hole's pitch angle ψ (Fig.5.1).

5.3.3 Visual compliant motion control

For clarifying how the visual compliant motion control is realized for the robot arm and the active peg, we will look into them one by one in the order illustrated above. Finally, the alignment algorithm for combining all of these motions will be addressed.

Co-point constraint (eye-in/to-hand camera)

In [89], a hybrid Jacobian matrix $\boldsymbol{\mathcal{J}}_{vc}$ is adopted, with the first two rows corresponding to vision-based control, and the third row corresponding to position

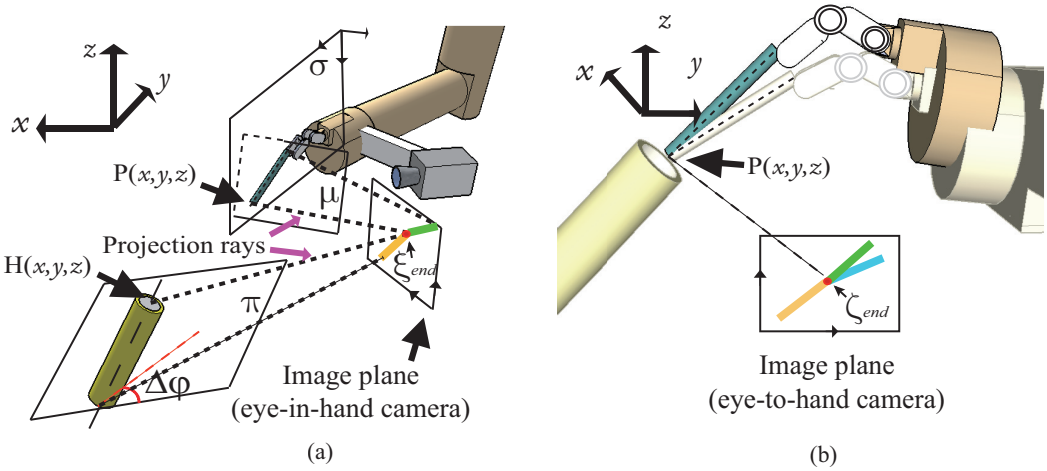

Figure 5.7: Visual constraints for effecting visual compliant motion

based control. In this study, we adopt vision-based control only.

Let $\dot{\boldsymbol{r}}_e$ represent the velocity screw of the end-effector relative to the end-effector's frame Σ_e, and $\dot{\boldsymbol{r}}_{ci}$ be the velocity screw of the eye-in-hand camera respected to the camera's frame Σ_{ci}. ${}^e\boldsymbol{W}_{ci}$ is the transformation matrix between $\dot{\boldsymbol{r}}_e$ and $\dot{\boldsymbol{r}}_{ci}$. From the differential motion relationship between two frames [90], we have

$$\dot{\boldsymbol{r}}_e = {}^e\boldsymbol{W}_{ci}\dot{\boldsymbol{r}}_{ci} \tag{5.8}$$

with

$${}^e\boldsymbol{W}_{ci} = \begin{bmatrix} {}^e\boldsymbol{R}_c & S({}^e\boldsymbol{t}_c)\,{}^e\boldsymbol{R}_c \\ 0 & {}^e\boldsymbol{R}_c \end{bmatrix} \tag{5.9}$$

where ${}^e\boldsymbol{R}_c, {}^e\boldsymbol{t}_c$ are the rotational matrix and translational vector between the end-effector frame and the camera frame Σ_{ci}, and suppose they have been calibrated ahead. $S({}^e\boldsymbol{t}_c)$ represents the skew-symmetric matrix associated with ${}^e\boldsymbol{t}_c$.

Let $\boldsymbol{\xi} = (u, v)^T$ be a point in image plane ξ, projected from the point $[X, Y, Z]^T$ in the frame Σ_{ci}. Let $\dot{\boldsymbol{r}}_{ci} = [T_x, T_y, T_z, \omega_x, \omega_y, \omega_z]^T$, then we have

$$\dot{\boldsymbol{\xi}} = \boldsymbol{\mathcal{J}}_{img}\dot{\boldsymbol{r}}_{ci} \tag{5.10}$$

where $\boldsymbol{\mathcal{J}}_{img}$ is the classical image Jacobian matrix [51],

$$\boldsymbol{\mathcal{J}}_{img} = \begin{bmatrix} \frac{f}{Z} & 0 & -\frac{u}{Z} & -\frac{uv}{f} & \frac{u^2+f^2}{f} & -v \\ 0 & \frac{f}{Z} & -\frac{v}{Z} & -\frac{v^2+f^2}{f} & \frac{uv}{f} & u \end{bmatrix} \tag{5.11}$$

where f is the camera's focal length, and Z is depth information.

Follow the method of the partitioned approach for image-based visual servoing approach [51], we change Eqn.(5.10) to be

$$\dot{\boldsymbol{\xi}} = \boldsymbol{\mathcal{J}}_{tz} T_z + \boldsymbol{\mathcal{J}}_{ref} \dot{\boldsymbol{r}}_{ref} \tag{5.12}$$

where $\dot{\boldsymbol{r}}_{ref} = [T_x, T_y, \omega_x, \omega_y, \omega_z]^T$, $\boldsymbol{\mathcal{J}}_{tz}$ is the third column of $\boldsymbol{\mathcal{J}}_{img}$, and $\boldsymbol{\mathcal{J}}_{ref}$ is formed by the rest five columns of $\boldsymbol{\mathcal{J}}_{img}$. Then we have

$$\dot{\boldsymbol{r}}_{ref} = \boldsymbol{\mathcal{J}}^{+}_{ref} (\dot{\boldsymbol{\xi}} - \boldsymbol{\mathcal{J}}_{tz} T_z) \tag{5.13}$$

where, $\boldsymbol{\mathcal{J}}^{+}_{ref}$ represents the pseudo-inverse for $\boldsymbol{\mathcal{J}}_{ref}$. The camera's $z-$axis translational control is given by

$$T_z = \gamma[\alpha(mdis(\boldsymbol{\zeta}^h_{end} - \boldsymbol{\zeta}^p_{end})) + (1-\alpha)(\zeta^h_{att} - \zeta^p_{att})] \tag{5.14}$$

where γ is a scalar gain factor, $\boldsymbol{\zeta}^h_{end} = (u'_h, v'_h)^T, \in \mathbb{Z}^2$ refers to the hole's endpoint, and $\boldsymbol{\zeta}^p_{end} = (u'_p, v'_p)^T, \in \mathbb{Z}^2$ represents the peg's endpoint, $\zeta^p_{att} \in \mathbb{Z}^1$ is for the peg's attitude and $\zeta^h_{att} \in \mathbb{Z}^1$ for the hole's attitude, α $(0 < \alpha < 1)$ is a scalar normalizing factor. $mdis(\cdot)$ represents the Manhattan distance calculation defined as

$$mdis(\boldsymbol{\zeta}^h_{end} - \boldsymbol{\zeta}^p_{end}) = \mid u'_h - u'_p \mid + \mid v'_h - v'_p \mid \tag{5.15}$$

Note that the image features related to Eqn.(5.14) are all from the eye-to-hand camera's image plane ζ. Here we only care about the one direction regulation to avoid the local minimum of T_z, which means $\alpha(mdis(\boldsymbol{\zeta}^h_{end} - \boldsymbol{\zeta}^p_{end}))$ and $(1-\alpha)(\zeta^h_{att} - \zeta^p_{att})$ have the same sign. The attitude for the peg ζ^p_{att} is defined as

$$\zeta^p_{att} = \delta v' / \delta u' \tag{5.16}$$

with $\delta v', \delta u'$ the image coordinate differences between the peg's two endpoints in image plane ζ. ζ^h_{att} is defined by the same method.

With T_z and $\dot{\boldsymbol{r}}_{ref}$ we then reconstruct the camera's motion vector $\dot{\boldsymbol{r}}_{ci} = [T_x, T_y, T_z, \omega_x, \omega_y, \omega_z]^T$, and with Eqn.(5.8) we can obtain the end-effector's velocity screw $\dot{\boldsymbol{r}}_e$. After that, with the robot arm's forward kinematics and its Jacobian matrix, we can further calculate the corresponding joint angles.

It should be pointed out, in order to construct the image Jacobian $\boldsymbol{\mathcal{J}}_{img}$, the depth Z should be known. Here, we roughly estimate it from the eye-to-hand camera's images by

$$\widehat{Z} = L_p \frac{\mid \boldsymbol{\zeta}^p_{end} - \boldsymbol{\zeta}^h_{end} \mid}{\zeta^p_l} + K_{cp} \tag{5.17}$$

where L_p is the peg's length which is known, $\zeta^p_l \in \mathbb{Z}^1$ is the length of the peg in ζ, and $\mid \boldsymbol{\zeta}^p_{end} - \boldsymbol{\zeta}^h_{end} \mid$ represents the distance from the peg to the hole. K_{cp} is the compensation part due to the offset from the peg to the eye-in-hand camera.

Line-parallel constraint (eye-in-hand camera)

Like the monocular approach, the robot arm's joint4 (as shown in Fig.5.2) is adopted to fit for an arbitrary heading angle of the hole by visual compliant motion. In fact, in order to realize line parallel constraint motion considering the peg's motion, the easiest way is to configure the eye-in-hand camera in such a way that the vertical plane passing through the optical axis of the camera is coincide with the plane σ (Fig.5.7(a)). Thus we simply adjust the hole's attitude in images to be vertical to keep the constraint, since the peg's attitude in images is always the same whether it moves or not. This actually requires the camera to be set in the center of the end-effector with strict accuracy relative to the peg's pose, whereas it is usually difficult to realize due to limited physical space and assembly error. In our case, the eye-in-hand camera and the peg are configured with an angle, and the same new image feature ξ_{head} as described before is adopted to realize the regulation of joint4 (please refer to the former section 5.2.2.2). During the experiments, we will see that this new image feature could work very well for the alignment. The control law for this visual compliant motion is

$$\tau_{head} = -K^p_{head}(\xi_{head} - \xi^*_{head}) - K^d_{head}\dot{q} + g \tag{5.18}$$

where, K^p_{head}, K^d_{head} are positive gain factors, τ_{head} is the input torque for the attitude accommodating joint, ξ^*_{head} is the calibrated value of ξ_{head} for alignment, $\dot{q}$ is the joint velocity, and g is the gravity compensation mainly due to the camera (the active peg is lightweight). Note that, the value of ξ^*_{head} is mainly affected by the external parameters of the eye-in-hand camera.

Co-point constraint (eye-to-hand camera)

As have been defined above, the attitude of peg and hole in the eye-to-hand camera's images are ζ^p_{att}, ζ^h_{att} respectively. These two are mainly reflecting the pitch angle ψ (Fig.5.1). Suppose the attitude angle of the peg is initially smaller than the hole's, under the robot arm's visual compliant motion, the hole's endpoint $\boldsymbol{H}(x, y, z)$ and the peg's endpoint $\boldsymbol{P}(x, y, z)$ reach the same point $\boldsymbol{\zeta}_{end} = (u'_0, v'_0)^T$ in image plane ζ. Since the robot arm is still moving, the peg's endpoint will generate a small displacement $\Delta\boldsymbol{\zeta}_{end} = (\Delta u', \Delta v')^T$ from $\boldsymbol{\zeta}_{end}$ in images. With the resolved-rate control, the active peg is controlled to eliminate the displacement, and as a result, the pitch angle of the peg becomes larger until the regulation finishes, and the adjusting process acts like the physical compliant motion. The control law for the active peg is

$$\boldsymbol{\tau}_{peg} = -K^p_{peg}\boldsymbol{J}^T(\frac{L_p}{\zeta^p_l}\Delta\boldsymbol{\zeta}_{end}) - K^d_{peg}\dot{\boldsymbol{q}}_p + \boldsymbol{g} \tag{5.19}$$

where, K^p_{peg}, K^d_{peg} are positive-definite coefficient matrices, $\boldsymbol{\tau}_{peg}$ are input torques for the active peg's two rotational joints, and $\dot{\boldsymbol{q}}_p$ is the peg's joint velocity, L_p/ζ^p_l acts as a scale factor, $\boldsymbol{g}$ is the gravity compensation, and $\boldsymbol{J}^T$ is the transpose of the active peg's Jacobian matrix. More details for the task-space PD control could be found in [91].

It should be noted that this simple approach fits for our high-speed visual feedback and the high-speed active peg which has big friction forces for the joints, thus the dynamic effects from the robot arm could be transferred to the endpoint of the peg, and visual compliant motion can be realized.

5.3.4 Peg-and-hole alignment

The peg-and-hole alignment is realized with the combination of the three visual compliant motions described above. The algorithm flow is shown in Fig.5.8.

To summarize, we have four convergence criteria from the two cameras for judging whether the alignment realized or not. They are: $\boldsymbol{err}^{\xi}_{end} = \boldsymbol{\xi}^p_{end} - \boldsymbol{\xi}^h_{end}$, the error between the peg and the hole's endpoint in image plane ξ; $err^{\xi}_{head} = \xi_{head} - \xi^*_{head}$, the error input for the line-parallel compliant motion; $err^{\zeta}_{att} = \zeta^p_{att} - \zeta^h_{att}$, the attitude error between peg and hole in image plane ζ; and $err^{\zeta}_{d} = \mid \boldsymbol{\zeta}^p_{end} - \boldsymbol{\zeta}^h_{end} \mid$, the distance between peg and hole's endpoint. The convergence time for alignment is defined as the time between the start of *phase* 1 and the end of *phase* 2 (Fig.5.8). Once the position alignment for hole's endpoint $\boldsymbol{H}(x, y, z)$ and peg's endpoint $\boldsymbol{P}(x, y, z)$ from the eye-to-hand camera's images is realized, the peg-and-hole alignment process moves from *phase* 1 into *phase* 2. After both the position and attitude alignment for peg and hole have been realized judging by both cameras, the alignment process moves out of *phase* 2, and active peg will then implement the insertion behavior.

During the *phase* 2 (Fig.5.8), since the active peg will be regulated to realize visual compliant motion, $\boldsymbol{\xi}^p_{end}$ would change, whereas the robot arm takes $\boldsymbol{\xi}^p_{end}$ as the target position for regulation. Since we want to realize a fast manipulation for the robot arm, a group of relatively large proportional gain factors is adopted. The high-speed active peg's motion may bring sudden changes of $\boldsymbol{\xi}^p_{end}$, which would cause unwanted effects for the robot arm's dynamic performance. In order to deal with such problem, as well as to prevent the sudden impact from the right start of the regulation due to the initial large visual errors, a shunting model [92] filter is adopted to modify the visual error $\boldsymbol{err}^{\xi}_{end} = \boldsymbol{\xi}^p_{end} - \boldsymbol{\xi}^h_{end}$. The shunting model is a neural-dynamics model and a typical shunting equation can be described as

$$\frac{dx_i}{dt} = -Ax_i + (B - x_i)S^e_i(t) - (D + x_i)S^i_i(t) \tag{5.20}$$

where $x_i \in \Re^1$ is the neural activity of ith-neuron. A, B and D are nonnegative constants describing the passive decay rate, the upper and lower bounds of x_i respectively. S_i^e and S_i^i are the excitatory input and the inhibitory input to the neuron respectively. The shunting model has the properties of automatic gain control, the state response bounded to the finite region $[-D, B]$, and smooth outputs even with inputs having sudden stimulus. Let the upper and lower bounds $B = D$, then the steady-state solution of Eqn.(5.20) is given by

$$x_i = x_i \frac{B}{A + \mid x_i \mid}, B = D \tag{5.21}$$

Then we have

$$\boldsymbol{err}_{end}^{\xi} = \boldsymbol{err}_{end}^{\xi} \frac{B}{A + \mid \boldsymbol{err}_{end}^{\xi} \mid} \tag{5.22}$$

Note that the parameter B decides the bounds, and A affect the duration time to reach the steady state.

5.3.5 Experimental evaluations

For both peg and hole, two markers made of light-reflecting material were fixed on the end part to indicate the endpoints (binary images for markers from two cameras are shown in Figure 5.9). The image processing algorithm calculated the moment feature for each marker to generate peg's and hole's image position ($\boldsymbol{\xi}_{end}^{p}$, $\boldsymbol{\xi}_{end}^{h}$ in image plane ξ; $\boldsymbol{\zeta}_{end}^{p}$, $\boldsymbol{\zeta}_{end}^{h}$ in image plane ζ), attitude angle (ξ_{att}^{h} in ξ; ζ_{att}^{p}, ζ_{att}^{h} in ζ), and the length information (ξ_{l}^{h} in ξ; ζ_{l}^{p} in ζ).

The hole was fixed on a pan-tilt platform with 50 mm offset from the platform's center, thus the hole's position $\boldsymbol{H}(x, y, z)$ and its attitude $\boldsymbol{H}(\varphi, \psi)$ could be set to different configurations. In the experiments, three different configurations were set randomly for the hole, and then three alignments were realized continuously. For the first alignment, from 0 - 5.0 s is for moving the active peg and the hole to the preparation pose. Here, we have set the preparation pose to be 5.0 s simply for the convenience of our experimental settings and it has no relation to the alignment process. For the second and third alignment, the preparation time takes 0.7 s. The insertion takes 0.5 s for each alignment (if alignment succeeds).

During the experiment, the coarse kinematic model of the robot arm as well as the active peg has been calibrated. Since the robot arm and the active peg have big reduction ratio for each rotational joint that adopts the harmonic gearbox, and the gravity compensation due the weight of the camera in Equation (5.18) and the weight of the active peg in Equation (5.19) has been ignored. As the experimental

Table 5.1: Average alignment performance.

Pose	Converge time (s)	Success rate (%)
1	0.39	85
2	0.68	90
3	0.53	85

results show later, this omission doesn't affect the convergence performance of the alignment.

Figure 5.11, 5.12, 5.13 show the process of the peg-and-hole alignment for three different configurations of the hole with two different point of view. The position and attitude alignment for the three times was converged at 0.366 s, 0.714 s, 0.456 s respectively (excluding the preparation time and insertion time), and then the insertions were triggered.

As shown in Figure 5.10(a), from the view of the eye-in-hand camera, the peg's position realized alignment with the hole's position for the three times, and as Figure 5.10(b) shows, for the regulation of the heading attitude by the image feature ξ_{head}, also reached the reference value for each time. From the view of the eye-to-hand camera, as Figure 5.10(c) shows, the attitude regulation for the pitch angle realized convergence for each time; in Figure 5.10(f), the image distances between the peg and hole's endpoint when alignment converged for three times was almost the same. From Figure 5.10(e), we can see that while the active peg conducted the visual compliant motion, the peg's endpoint could be kept within a small range although affected by the arm's motion and its dynamics. Finally, Figure 5.10(d) shows the image trajectory for the hole and the peg's endpoint during the first alignment.

Table 5.1 shows the average convergence time, success rate of the hole's three different pose for 20 trials.

In the experiment, for three configurations of the hole, the success rate of the alignment (insertion of the peg into the hole successfully conducted) was about 85%, with an average time of about 0.7 s (excluding the preparation time). Since in the experiment, we set the peg's outside diameter and the hole's inner diameter to be 10 mm, 14 mm respectively, the tolerance error for the insertion is ± 2 mm (the attitude was always well aligned). The videos of the experiment can be found on the website [93].

5.3.6 Discussions

As shown in Figure 5.14, the misalignment means that the peg's converged position was not in the clearance range. It can be seen that the error range along the horizontal direction - u had been exceeded the clearance range, while along the direction of v had been smaller than the clearance range. This means that the misalignment had been caused by the robot arm's dynamics in the directions along the horizontal axis of the image plane ξ during the *phase* 2 (Figure 5.8). As a matter of fact, currently the active peg can only conduct 2D motion due to the limited DOFs, and the dynamic compensation as proposed in our concept (Figure 2.2) could only be realized in the direction along the projection ray formed by $\boldsymbol{H}(x, y, z)$ and $\boldsymbol{\xi}_{end}$ (Figure 5.7(a)). In order to compensate for the dynamic effects along the horizontal axis of the image plane ξ brought by the robot arm, corresponding DOFs need to be added in the future work. On the other hand, the effectiveness of the proposed dynamic compensation concept thus becomes obvious thanks to the comparison of the failures. The other big reason for the failure lay in the fact that the insertion mechanism (the prismatic joint of the active peg) has been assembled very poorly, and it exhibits great vibrations, especially along the horizontal direction during the alignment task.

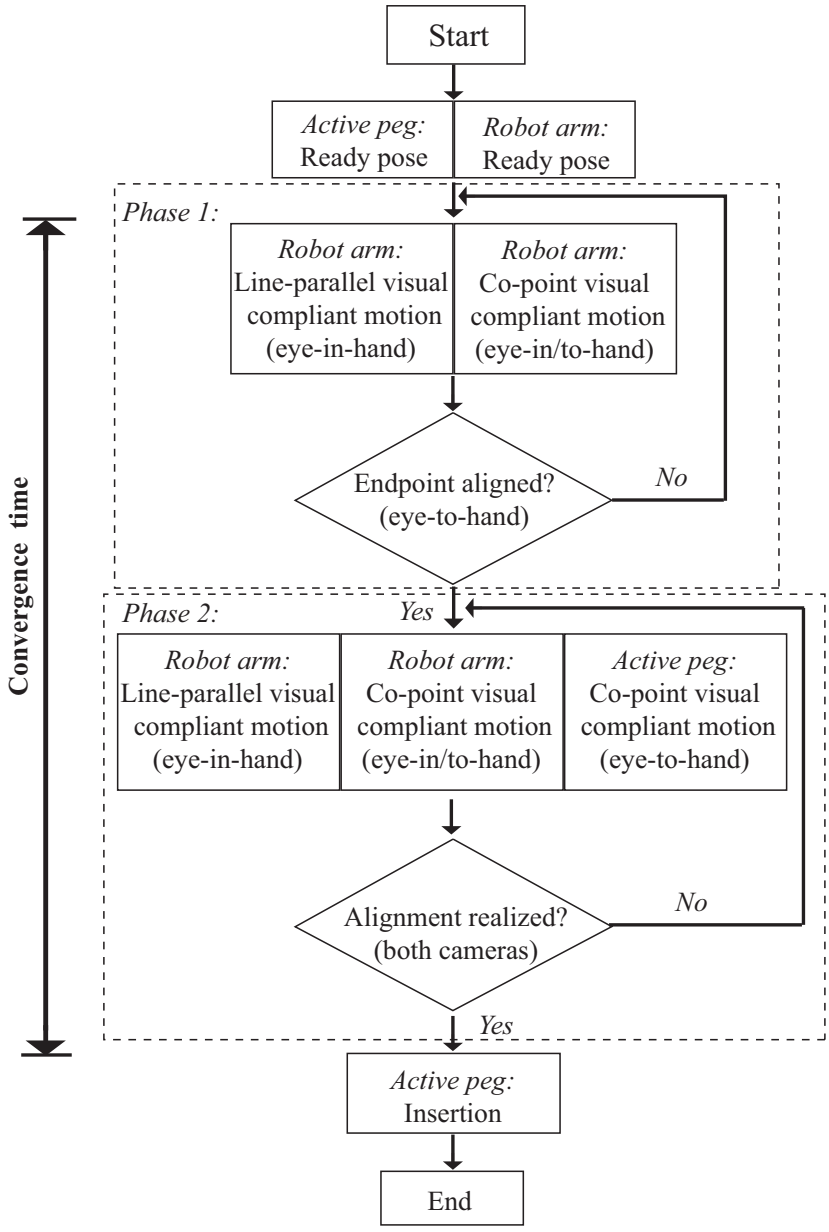

Figure 5.8: Algorithm flow of peg-and-hole alignment

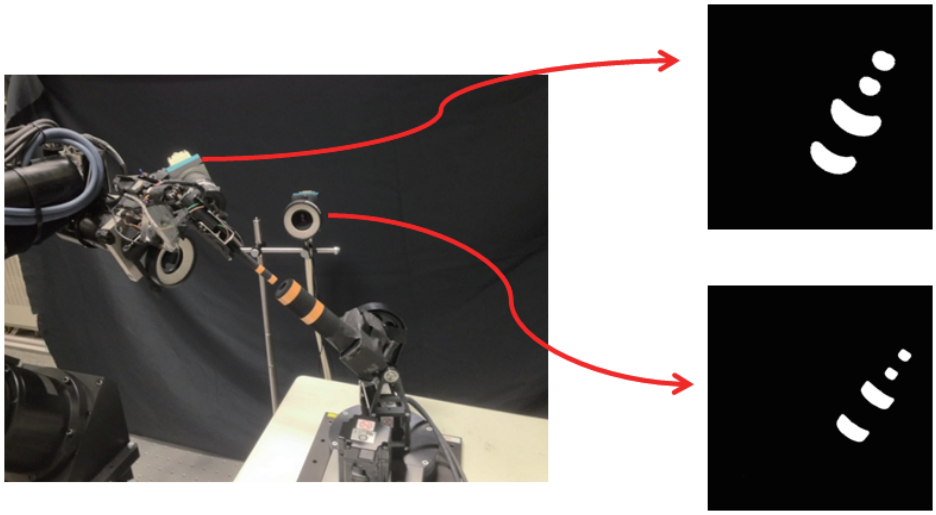

Figure 5.9: Binary images for markers

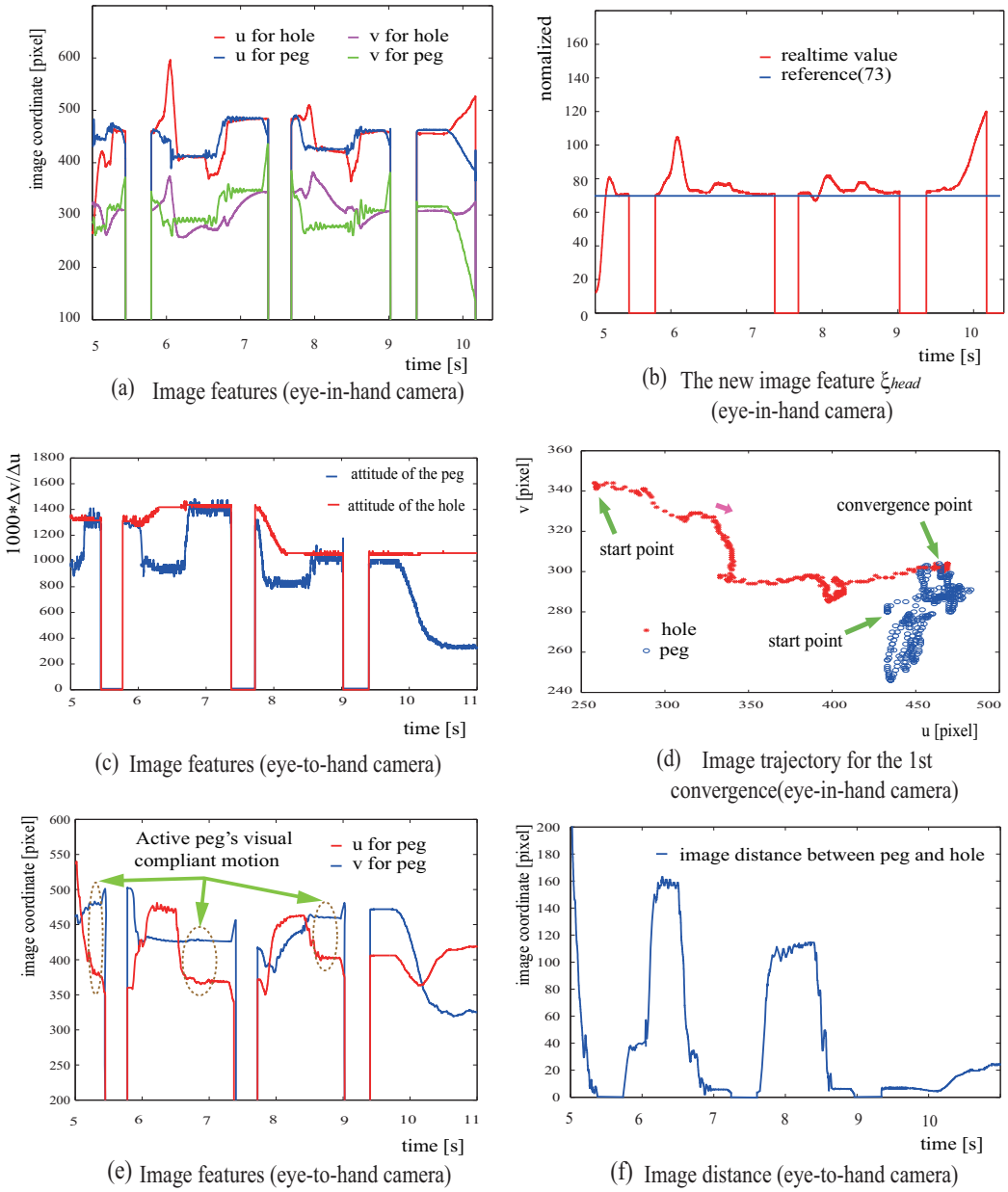

(a) Image features (eye-in-hand camera)

(b) The new image feature ξ_{head} (eye-in-hand camera)

(c) Image features (eye-to-hand camera)

(d) Image trajectory for the 1st convergence(eye-in-hand camera)

(e) Image features (eye-to-hand camera)

(f) Image distance (eye-to-hand camera)

Notes:

1) 0 ~ 5.0[s]: preparation ; 5.0 ~ 5.366 [s]: 1st alignment; 5.366 ~ 5.866 [s]: insertion
5.866 ~ 6.566[s]: preparation ; 6.566 ~ 7.280 [s]: 2nd alignment ; 7.280 ~ 7.780 [s]: insertion
7.780 ~ 8.480[s]: preparation ; 8.480 ~ 8.936 [s]: 3rd alignment ; 8.936 ~ 9.436[s]: insertion

2) The insertion will cause image features' value to zero.

Figure 5.10: Image features during alignment process

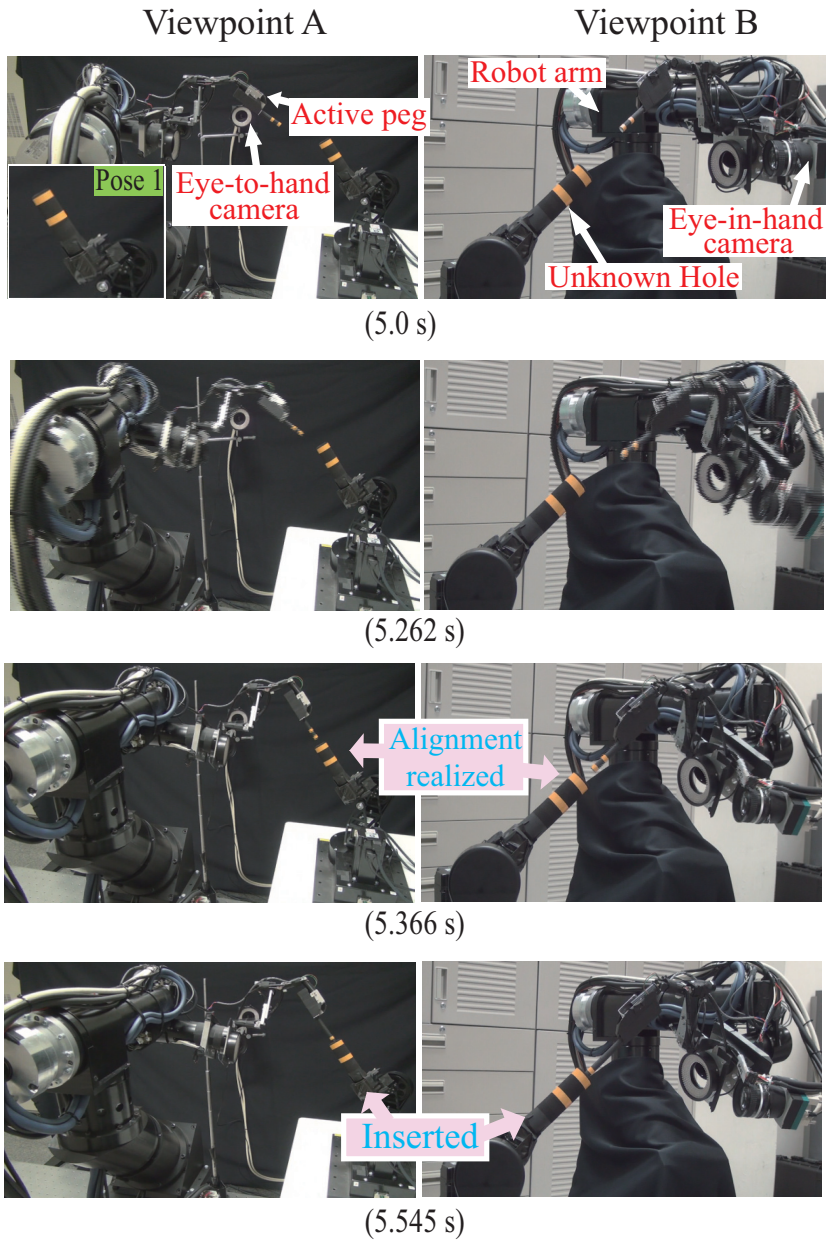

(a) Alginment - 1 (Hole's pose 1)

Figure 5.11: Continuous images for three times' alignment from two viewpoints

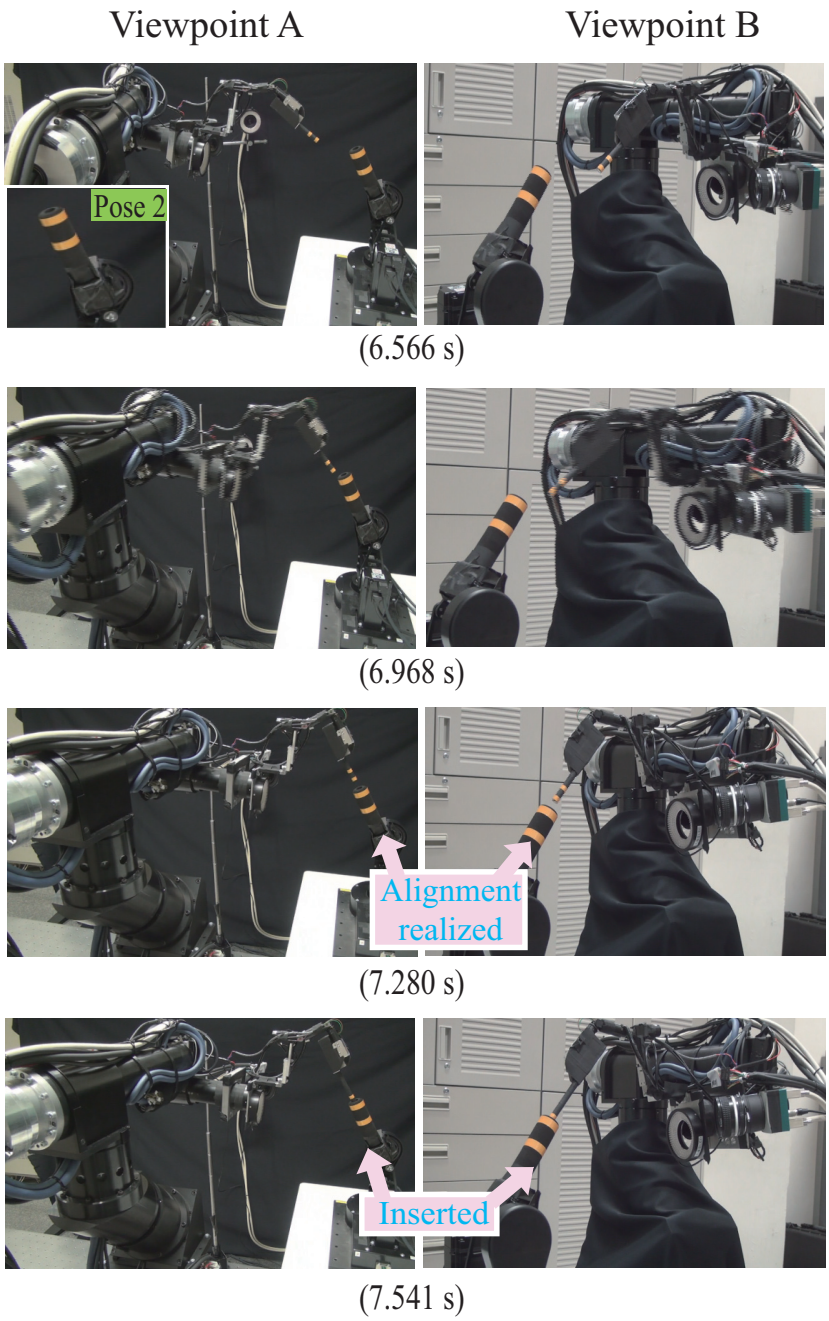

(b) Alginment - 2 (Hole's pose 2)

Figure 5.12: Continuous images for three times' alignment from two viewpoints (continue)

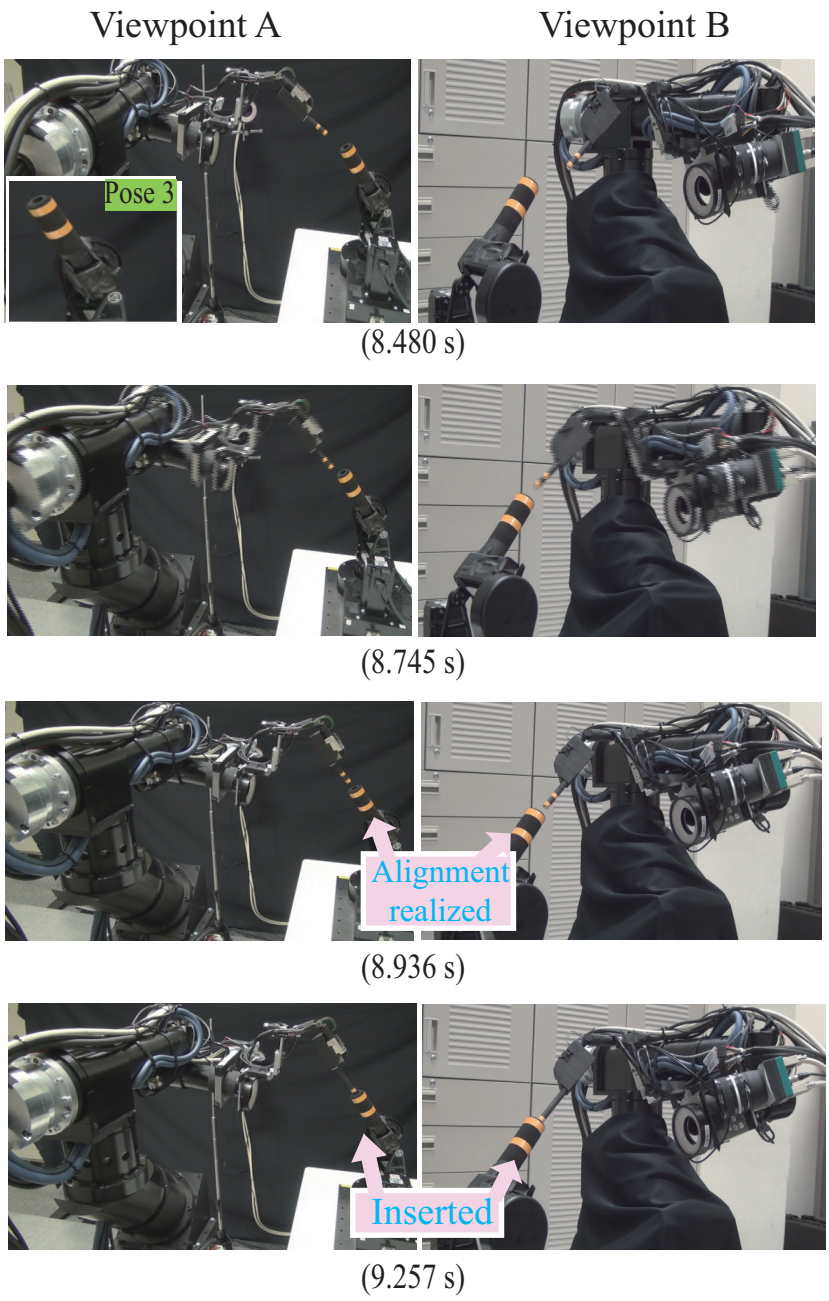

(c) Alginment - 3 (Hole's pose 3)

Figure 5.13: Continuous images for three times' alignment from two viewpoints (continue)

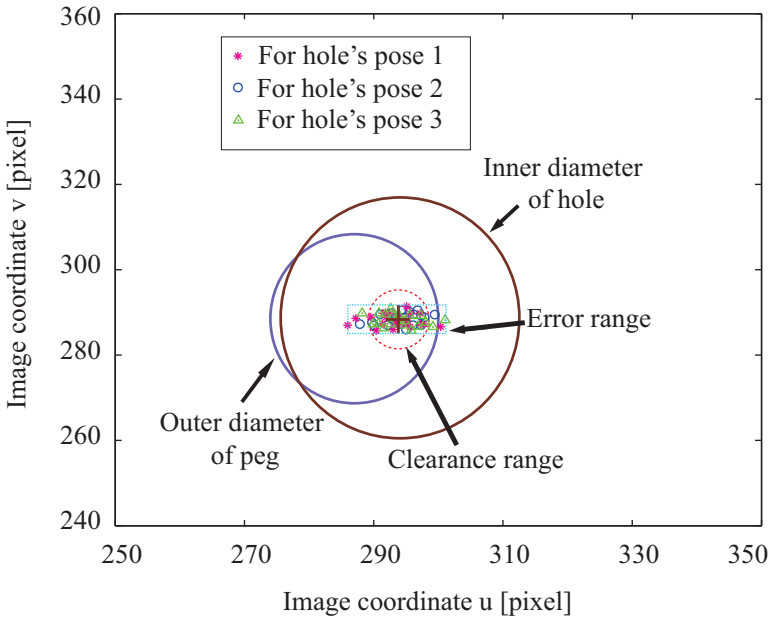

Figure 5.14: The error distribution of the peg's converged image position from eye-in-hand camera for 20 trials

5.4 Summary of this chapter

Concerning with the 3D peg-and-hole alignment problem, the monocular approach and the binocular approach based on the dynamic compensation concept have been proposed. Although the accuracy level for the peg-and-hole alignment in our experiments can not be competitive compared with the traditional approaches that adopt the force/torque sensor, peg-and-hole alignment based on high-speed visual servo under the compensation concept can be realized much faster than the traditional approaches. For instance, in [86], they realized the alignment with 0.1 mm clearance, whereas it took 13 s for the alignment process. Besides, as described in section 5.3.6, the accuracy level actually has the potential for improvement with the modification of the hardware system. What's more, since in the proposed vision-based alignment approaches, there is no need for contact between the peg and the hole throughout the whole process, it can be applied to some special manipulations where no contact is allowed between the peg and the hole while performing their alignment.

Chapter 6

Conclusions

6.1 Conclusions

In this thesis, in order to realize the high-speed and accurate interactive manipulation in a large workspace based on the vision sensor without modeling system dynamics, a dynamic compensation concept by adoption of high-speed lightweight compensation actuator as well as the high-speed visual feedback based on relative coordinate has been proposed. Unlike traditional approaches where the accurate models of the robot system as well as fine calibration works for robot and sensors are needed, the proposed approach fully takes advantages of the high-speed task-space vision sensing in compensating for the many uncertainties to realize accurate interactive positioning regulation under high speed.

Firstly, with the introduction of the background for robotic technology, the difficulties concerning with high-speed and accurate interactive manipulation with simple control approaches were summarized. Although there have been some related works in tackling these difficulties from the approach of compensation, no general and practical method is available. On the other hand, the vision-based robotic control has become much popular and critical in nowadays, especially with the application of high-speed vision systems which have been commercially available several years ago. The great advantage of the high-speed vision sensing is that it can provide with the task-space feedback information in high frequency and is not dependent on the kinematics, whereas the traditional joint-level sensing usually needs the conversion to the task-space through accurate kinematic models (mechanical backlash may bring great errors into this conversion). By fusing the high-speed visual feedback and a high-speed lightweight compensation actuator, it may be possible to realize high-speed and accurate interactive manipulation without considering the system dynamics. With this consideration, the dynamic compensation concept as well as the resulted dynamic compensation robotics

system (DCRS) is proposed.

Secondly, experimental systems in accordance with the dynamic compensation concept are introduced. In order to illustrate the importance of the two aspects of the dynamic compensation concept, namely the compensation actuator and the high-speed visual feedback, experimental evaluations based on a 1-DOF DCRS prototype have been conducted. Fast response order of the compensation actuator as well as high-speed frequency of the visual feedback have shown great effect on compensation performance through the evaluations.

The third, improved positioning-oriented algorithms based on relative coordinate high-speed visual feedback are proposed for the DCRS. The simplified IBVS approach for robot arms is depth-independent and is easy for implementation, although it can hardly be the optimal trajectory planner. The effectiveness of this approach is verified through numerical simulations and experimental high-speed tracking. As for the compensation actuator, a pre-compensated PD approach is proposed with the consideration of the dynamic impact from the main robot. Experimental evaluations show the better performance of the proposed approach compared with the simple PD control.

As the basic application task, the 1D positioning with the name of dynamic super picking is demonstrated by the developed 1-DOF DCRS. A much more sophisticated algorithm - pre-compensation fuzzy logic control (PFLC) is proposed by exploiting the motions for the 1-DOF linear DCRS. The PFLC is easy for implementation and proper for the high-speed compensation. Experimental evaluations for PFLC comparing with some other approaches, as well as the dynamic super picking task showed satisfying results.

After that, the application task is extended from 1D positioning into 3D position and attitude regulation, and the challenging task - fast peg-and-hole alignment with large position and attitude uncertainty is addressed. The difficulties for the fast alignment is not only due to the coupling between position alignment and attitude alignment, but also due to the dynamics of the robot arm. An active peg with accordance to the dynamic compensation concept is designed to cooperate with the robot arm. Two approaches, monocular and binocular are proposed to realize the fast alignment. In the monocular approach, the motion separation based on simplified IBVS for robot arm and step approaching visual servo for active peg enables the convergence for alignment within 2 s on average with 65% success rate. A visual compliance method is exploited for the binocular approach, and the convergence for alignment can be realized within 0.7 s on average with 85% success rate.

6.2 Into the application - a scenario in the near future

Ever since the first industrial robot *the Unimate* was installed in 1959, the key technologies of robotics have been greatly developed as the needs for robotic manipulation in manufacturing kept upgrading. Today industrial robots are key components of automotive industry, and it is said that more than 1.1 million industrial robots and robotic systems are operating in the factories all over the world [94], with the functioning such as:

- Improving quality of work for employees;
- Increasing production output rates;
- Improving product quality and consistency;
- Increasing exibility in product manufacturing;
- Reducing operating costs.

Nevertheless, since the cost for employing a robotic system is still not cheap , we may reasonably ask questions such as could these specialized robotic systems meet with much more dexterous manipulations in a much more dynamical environment? Or in another word, can they fit for much more flexible applications? Especially, high-speed manipulations with great environmental uncertainties are of great needs in real applications. Concerning with such issues, we think that the method of alteration based on modular assembly would be a good way for lowing the cost and improving the flexibility, and the main issue addressed this study is such kind of attempt as to improve the performance of the main robot (which is maybe old enough for retiring) by adopting the dynamic compensation concept. Let's consider such a scenario, which may happen in the near future:

A factory making engines for aircraft owns 50 old type industrial robot arms, which had been equipped several dozens of years ago for doing the task of automotive bolts fastening (refer to the Figure 6.1). The task of the bolt-fasten has been a rather critical procedure in assembling this certain type of engines. These arms experienced years of mechanical wear, and one day they can no longer be applied for this accurate manipulation, especially under high-speed motion, which had been the key aspect of making these arms outstanding in terms of high productivity and quality in the past years. In the usual way, they shall be retired and be replaced with the new ones. However, the managers of the factory feel a little bit of troublesome cause this obviously need a big budget, which would make

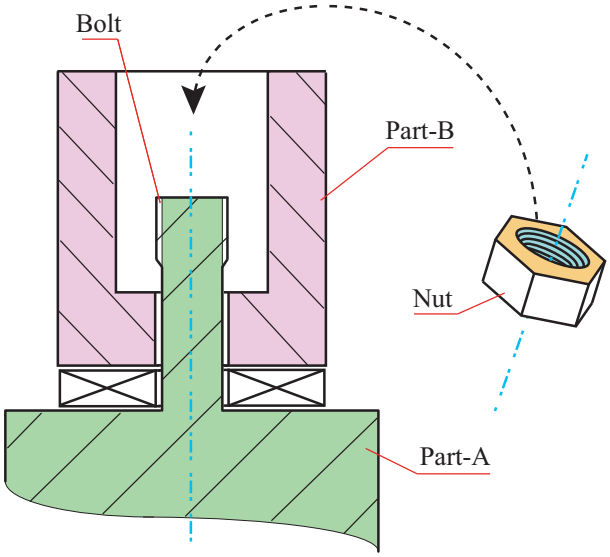

Figure 6.1: The bolt-fastening task.

the company's financial situation much worse under the background of worldwide depression of these days. At this time, a robot company comes up with a solution, and claims that it will only cost approximately 1/6 to 1/10 of the budget to recover these robot arms' production capacity. Their solution is based on the modular assembly and dynamic compensation concept. By adding a modularized compensation actuator as well as high-speed cameras onto the old robot arm , the dynamic defects of the old robot arm thus be compensated, and there will be no need for modification of the controller of the robot arm. With this approach, not only the production capacity has been recovered, but also the flexibility has been improved, and finally the factory realizes this updating with a very low cost.

Acknowledgements

Completion of this doctoral thesis was possible with the support of many people. I would like to express my sincere gratitude to all of them.

First of all, I am extremely grateful to my supervisor, Prof. Masatoshi Ishikawa, for his valuable guidance, the great support of the research environment, as well as the consistent encouragement I received throughout the research work. Prof. Ishikawa has always made himself available to discuss with my research despite his busy schedules and provided me with many great suggestions, and I always consider it as a great opportunity to do the doctoral program under his guidance, for that Prof. Ishikawa not only kindly teaches us about the research expertise, but also the philosophy of doing research. I think it will benefit me in the whole life.

Secondly, I would like to express my gratitude to Dr. Taku Senoo and Dr. Yuji Yamakawa. As the group leader of the Sensor Fusion devision, Dr. Senoo not only gave me the direct guidance and many helpful suggestions, but also supported me with all the facilities that I needed to carry out the research work. Dr. Yamakawa also helped me a lot throughout the whole research work, from discussion of approaches to setup of the experimental systems. I was greatly inspired by their research expertise in doing research, and extremely appreciate their generosity in sacrificing so much time and effort to help with my research work.

I acknowledge all the members of the defense committee, including Prof. Masayuki Inaba, Prof. Hiroshi Esaki, Prof. Hiroyuki Shinoda, Lecturer Hideki Nakayama and Assoc. Prof. Hiromasa Oku. I am extremely grateful for their great efforts in reading my thesis despite of their busy schedules, and for their many useful comments that helped refine this work. And it is a great honor for me to be instructed by the great teachers of their research field.

I am very grateful to Assoc. Prof. Hiromasa Oku, who has given me lots of support throughout the doctoral course. I acknowledge Dr.

Alvaro Cassinelli, Dr. Niklas Bergstrm and Dr. Yoshihiro Watanabe, for their kind support of my research and gave me many suggestions concerning their research field.

Special thanks to the Sensor Fusion group members, Akihito Noda, Kenichi Murakami, Hyuno Kim, Tomoki Tamada, Shisei Nakano, Masahiro Hirano and M. Sakti Alvissalim. It was a great honor and pleasure to be able to do research with all these genius people.

I would also like to express my appreciation to Mr. Tomohiko Hayakawa and Dr. Kohei Okumura, who have given me consistent encouragement and support throughout my research and study. Especially I thank Mr. Tomohiko Hayakawa, who acted as my tutor while I arrived at Japan, and gave me great help and encouragement to get used to the life here.

I acknowledge all the members from the Ishikawa Oku laboratory, including the kind secretaries and supporting stuffs, the doctor course students and the master course students. Thanks for their kind support and help, the laboratory has been the warm home for me in these years.

I wish to give thanks to all of the kind Japanese people, whose name I knew or not, who have helped and encouraged me to get good used to the life here in Japan. Among them, I would give special thanks to Kanamori-san, the householder of my apartment, who has been always kindly helped me with the living issues and given me encouragements and suggestions while I was encountered with problems or difficulties.

Condolences are sent to the great casualties during the Great East Japan Earthquake (the 3.11 Earthquake). Although I was very frightened when I personally experienced the earthquake and greatly shocked by the severe damages due to the tsunami, I was much more impressed by the great spirits of the Japanese people especially the local people who have suffered so much from the intensive disaster. During the one week volunteer visit to Otsuchi-cho in Iwate in May, 2012, I was deeply touched by the responsibility, the indomitability of the local people, and felt their great confidence and hope after witnessing the well-organized recovering work. I hope things would go well, and the local people could live back to the normal and even the much better life in the near future.

Thanks also to the Japanese Ministry of education, culture, sports, science and technology (MEXT) for the MEXT scholarship that I had been offered. Thanks to the 3-years program of this scholarship,

I had the chance to do the doctoral program here in Japan, and can always focus on the research work. Just as the good will of this joint program between the Japanese MEXT and Chinese Scholarship Council, the friendly exchange and mutual understanding is the best way for building good future of this region, and I will try my best to contribute to the friendship of these two countries.

I owe a lot to my family. Thanks for your endless encouragement and support at every stage of my personal and academic life, and I know that you have been long desired to see this achievement to come true.

The last, I would like to express my deep condolences to the passing away of our highly respected Dr. Carson Reynolds, from whom I have benefited a lot through the fruitful discussions with him and we will miss him forever.

References

[1] M. Ishikawa T. Komuro, I. Ishii. Vision chip architecture using general-purpose processing elements for 1ms vision system. *4th IEEE Int. Workshop on Computer Architecture for Machine Perception*, pages 276–279, 1997.

[2] Y. Yamakawa. *High-speed Manipulation using Deformation and Manipulation Models of Flexible Objects*. PhD thesis, The University of Tokyo, Department of System Informatics, 2010.

[3] *http://www.faulhaber.com/*.

[4] *http://www.mikrotron.de/*.

[5] *http://www.photron.co.jp/*.

[6] G. Bekey, R. Ambrose, V. Kumar, D. Lavery, A. Sanderson, B. Wilcox, J. Yuh, and Y. Zheng. *Robotics: State of the Art and Future Challenges*. World Scientific, 2008.

[7] Foxconn to use more robots in assembly lines. *http://www.itnews.com.au/News/265544,foxconn-to-use-more-robots-in-assembly-lines.aspx/*.

[8] S.A. Hutchinson, G. Hager, and P.I. Corke. A tutorial on visual servo control. *IEEE Trans. on Robot. and Autom.*, 12(5):651–670, 1996.

[9] R. Kelly, R. Carelli, O. Nasisi, B. Kuchen, and F. Reyes. Stable visual servoing of camera-in-hand robotic systems. *IEEE/ASME Trans. on Mechatronics*, 5(1):39–48, 2000.

[10] F. Chaumette. Potential problems of stability and convergence in image-based and position-based visual servoing. *The Confluence of Vision and Control, LNCIS Series, D. Kriegman, G. Hager, and A. Morse, Eds. New York: Springer Verlag*, 237:66–78, 1998.

[11] Y. Nakabo, M. Ishikawa, H. Toyoda, and S. Mizuno. 1ms column parallel vision system and its application of high speed target tracking. *Proc. of IEEE Int. Conf. on Robotics and Automation*, pages 650–655, 2000.

[12] F.L. Lewis, D.M. Dawson, and C.T. Abdallah. *Robot Manipulator Control: Theory and Practice*. New York: CRC Press, 2003.

[13] Y. Zhang, W.A. Gruver, and F. Gao. Dynamic simplification of three degree of freedom manipulators with closed chains. *Rob. Auton. Syst.*, 28(4):261–269, 1999.

[14] A.Y. Zomaya and A.S. MORRIS. The dynamic performance of robot manipulators under different operating conditions. *IEE Proc. on Control Theory and Applications*, 137(5):281–289, 1990.

[15] T. Senoo, A. Namiki, and M. Ishikawa. High-speed batting using a multi-jointed manipulator. *Proc. of IEEE Int. Conf. on Robotics and Automation*, pages 1191–1196, 2004.

[16] T. Senoo, A. Namiki, and M. Ishikawa. Ball control in high-speed batting motion using hybrid trajectory generator. *Proc. of IEEE Int. Conf. on Robotics and Automation*, pages 1762–1767, 2006.

[17] H. Oku, I. Ishii, and M. Ishikawa. Tracking a protozoon using high-speed visual feedback. *Proc. of 1st Ann. Int. IEEE-EMBS Special Topic Conf. on Microtechnologies in Medicine & Biology*, pages 156–159, 2000.

[18] H. Oku, I. Ishii, and M. Ishikawa. A microscopic visual feedback system. *Systems and Computers in Japan*, 35(13):71–79, 2004.

[19] N. Ogawa, H. Oku, K. Hashimoto, and M. Ishikawa. Motile cell galvanotaxis control using high-speed tracking system. *Proc. of IEEE Int. Conf. on Robotics and Automation*, pages 1646–1651, 2004.

[20] M. B. Leahy Jr. Industrial manipulator control with feedforward dynamic compensation. *Proc. of 27th. Conf. on decision and control*, pages 598–603, 1988.

[21] T. Yoshikawa. *Foundations of robotics: Analysis and Control*. Cambridge (MA): MIT Press, 1990.

[22] A. Karakasoglu, S.I. Sudharsanan, and M.K. Sundareshan. Identification and decentralized adaptive control using dynamical neural networks with application to robotic manipulators. *IEEE Tran. Neural Netw.*, 4(6):919–930, 1993.

[23] J. Imura, T. Sugie, and T. Yoshikawa. Adaptive robust control of robot manipulators-theory and experiment. *IEEE Trans. on Robot. and Autom.*, 10(5):705–710, 1994.

[24] P.R. Pagilla and M. Tomizuka. An adaptive output feedback controller for robot arms: stability and experiments. *Automatica*, 37(7):983–995, 2001.

[25] N. Sadegh and R. Horowitz. Stability and robustness analysis of a class of adaptive controllers for robotic manipulators. *Int. J. of Robotics Research*, 9(3):74–92, 1990.

[26] N. Hogan. Impedance control: An approach to manipulation, part 1 to part 3. *J. Dynam. Syst., Meas., Contr.*, 107(1):1–24, 1985.

[27] W. Lu and Q.H. Meng. Impedance control with adaptation for robotic manipulations. *IEEE Trans. on Robot. and Autom.*, 7(3):408–415, 1991.

[28] B. Isela, R. Fernando, M. Marco, and J.G. Emilio. A dynamic-compensation approach to impedance control of robot manipulators. *J. Intell. Robot Syst.*, 63(1):51–73, 2011.

[29] N. Hogan, A. Sharon, and E.D. Hardt. High bandwidth force regulation and inertia reduction using a macro/micro manipulator system. *Proc. of IEEE Int. Conf. on Robotics and Automation*, pages 126–132, 1988.

[30] A. Sharon, N. Hogan, and E.D. Hardt. The macro/micro manipulator: An improved architecture for robot control. *Robot. Comput.-Integr. Manuf.*, 10(3):209–222, 1993.

[31] J.Y. Lew and D.J. Trudnowski. Vibration control of a micro/macro-manipulator system. *IEEE Control Systems*, 16(1):26–31, 1996.

[32] M. Kimata, Y. Morita, H. Ukai, H. Kando, and F. Matsuno. Pds control of macro-micro arm. *Proc. of IEEE Int. Workshop on Advanced Motion Control*, pages 123–128, 2004.

[33] W.L. Ballhaus and S.M. Rock. End-point control of a two-link flexible robotic manipulator with a mini-manipulator: Dynamic coupling issues. *Proc. of the ASME Winter Annual Meeting*, pages 17–22, 1992.

[34] H.D. Stevens and J. How. The limitations of independent controller design for a multiple-link flexible macro-manipulator carrying a rigid mini-manipulator. *Proc. of 2nd Conf. on Robotics for Challenging Environments*, pages 93–99, 1996.

[35] T. Yoshikawa, K. Hosoda, T. Doi, and H. Murakami. Dynamic trajectory tracking control of flexible manipulator by macro-micro manipulator system. *Proc. of IEEE Int. Conf. on Robotics and Automation*, pages 1804–1809, 1994.

[36] A. Hodac and R. Siegwart. Endpoint control of a fast and precise macro/micro-manipulator. *Proc. of 4th Int. Conf. on Motion and Vibration Control*, pages 883–888, 1998.

[37] A. Hodac and R. Siegwart. Decoupled macro/micro-manipulator for fast and precise assembly operations: design and experiments. *Proc. of SPIE on Microrobotics and Microassembly*, pages 122–130, 1999.

[38] T.W. Yang, W.L. Xu, and J.D. Han. Dynamic compensation control of flexible macromicro manipulator systems. *IEEE Trans. on Control systems technology*, 18(1):143–151, 2010.

[39] C. Cho, S. Kang, M. Kim, and J. Song. Macro-micro manipulation with visual tracking and its application to wheel assembly. *Int. J. Control Autom. Syst.*, 3(3):461–468, 2005.

[40] A. Namiki, Y. Imai, M. Ishikawa, and M. Kaneko. Development of a high-speed multifingered hand system and its application to catching. *Proc. of IEEE/RSJ Int. Conf. on Intelligent Robots and Systems*, pages 2666–2671, 2003.

[41] *http://www.youtube.com/watch?v=3nxjjztQKtY.*

[42] M. Ishikawa, A. Namiki, T. Senoo, and Y. Yamakawa. Ultra high-speed robot based on 1 khz vision system. *Proc. of IEEE/RSJ Int. Conf. on Intelligent Robots and Systems*, pages 5460–5461, 2012.

[43] J. Dunlap. *http://www.codeproject.com/Articles/16405/Queue-Linear-Flood-Fill-A-Fast-Flood-Fill-Algorith.*

[44] K.P.H. Berthold. *Robot Vision.* The MIT Press, 1986.

[45] S. Huang, Y. Yamakawa, T. Senoo, and M. Ishikawa. Dynamic compensation by fusing a high-speed actuator and high-speed visual feedback with its application to fast peg-and-hole alignment. *Advanced Robotics*, 28(9):613–624, 2014.

[46] Y.H. Liu, H. Wang, C. Wang, and K. Lam. Uncalibrated visual servoing of robots using a depth-independent interaction matrix. *IEEE Trans. on Robotics*, 22(4):804–817, 2006.

[47] H. Wang, Y.H. Liu, and D. Zhou. Adaptive visual servoing using point and line features with an uncalibrated eye-in-hand camera. *IEEE Trans. on Robotics*, 24(4):843–856, 2008.

[48] D.A. Luca, G. Oriolo, and G.P. Robuffo. Feature depth observation for image-based visual servoing: theory and experiments. *Int. J. of Robotics Research*, 27(10):1093–1116, 2008.

[49] K. Deguchi. Optimal motion control for imagebased visual servoing by decoupling translation and rotation. *Proc. of IEEE/RSJ Int. Conf. on Intelligent Robots and Systems*, pages 705–711, 1998.

[50] E. Malis, F. Chaumette, and S. Boudet. 2-1/2d visual servoing. *IEEE Trans. on Robot. and Autom.*, 15(2):238–250, 1999.

[51] P.I. Corke and S.A. Hutchinson. A new partitioned approach to image-based visual servoing control. *IEEE Trans. on Robot. and Autom.*, 17(4):507–515, 2001.

[52] K. Deguchi. Image based visual servoing with partitioned approach. *Proc. of the Workshop on Science of Computer Vision*, pages 75–85, 2002.

[53] K. Hosoda and M. Asada. Versatile visual servoing without knowledge of true jacobian. *Proc. of IEEE/RSJ Int. Conf. on Intelligent Robots and Systems*, pages 186–193, 1994.

[54] K. Deguchi, H. Sakurai, and S. Ushida. A goal oriented just-in-time visual servoing for ball catching robot arm. *Proc. of Int. Conf. Intelligent robots and systems*, pages 3034–3039, 2008.

[55] X. Lv and X. Huang. Fuzzy adaptive kalman filtering based estimation of image jacobian for uncalibrated visual servoing. *Proc. of IEEE/RSJ Int. Conf. on Intelligent Robots and Systems*, pages 2167–2162, 2006.

[56] M. Jagersand, O. Fuentes, and R. Nelson. Experimental evaluation of uncalibrated visual servoing for precision manipulation. *Proc. of IEEE Int. Conf. on Robotics and Automation*, pages 2874–2880, 1997.

[57] J.A. Piepmeier, G.V. McMurray, and H. Lipkin. Uncalibrated dynamic visual servoing. *IEEE Trans. on Robot. and Autom.*, 20(1):143–147, 2004.

[58] S. Huang, Y. Yamakawa, T. Senoo, and M. Ishikawa. A direct visual servoing scheme based on simplified interaction matrix for high-speed manipulation. *Proc. of IEEE Int. Conf. on Robotics and Biomimetics*, pages 1950–1955, 2012.

[59] C.W. WAMPLER. Manipulator inverse kinematic solutions based on vector formulations and damped least squares methods. *IEEE Trans. on Systems, Man, and Cybernetics*, 16(1):93–101, 1986.

[60] P.I. Corke. Robotics toolbox for matlab. *IEEE Robotics and Automation Magazine*, 3(1):24–32, 1996.

[61] M.W. Spong, S.A. Hutchinson, and M. Vidyasagar. *Robot Dynamics and Control*. John Wiley & Sons, 2004.

[62] E. Aboaf, S. Drucker, and C.G. Atkeson. Task-level robot learning juggling a tennis ball more accurately. *Proc. of IEEE Int. Conf. on Robotics and Automation*, pages 1290–1295, 1989.

[63] K. Nishiwaki, A. Konno, K. Nagashima, M. Inaba, and H. Inoue. The humanoid saika that catches a thrown ball. *Proc. of Int. Workshop on Robot and Human Communication*, pages 94–99, 1997.

[64] U. Frese, B. Bäuml, S. Haidacher, G. Schreiber, I. Schaefer, M. Hähnle, and G. Hirzinger. Off-the-shelf vision for a robotic ball catcher. *Proc. of IEEE/RSJ Int. Conf. on Intelligent Robots and Systems*, pages 1623–1629, 2001.

[65] M. Riley and C.G. Atkeson. Robot catching: Towards engaging human-humanoid interaction. *Auton. Robots*, 12(1):119–128, 2002.

[66] B. Bäuml, T. Wimböck, and G. Hirzinger. Kinematically optimal catching a ying ball with a hand-arm-system. *Proc. of IEEE/RSJ Int. Conf. on Intelligent Robots and Systems*, pages 2592–2599, 2010.

[67] O. Birbach, U. Frese, and B. Bäuml. Realtime perception for catching: a ying ball with a mobile humanoid. *Proc. of IEEE Int. Conf. on Robotics and Automation*, pages 5955–5962, 2011.

[68] R. Mori, K. Hashimoto, and F. Miyazaki. Tracking and catching of 3d ying target based on gag strategy. *Proc. of IEEE Int. Conf. on Robotics and Automation*, pages 5189–5194, 2004.

[69] K. Deguchi, H. Sakurai, and S. Ushida. A goal oriented just-in-time visual servoing for ball catching robot arm. *Proc. of IEEE/RSJ Int. Conf. on Intelligent Robots and Systems*, pages 3034–3039, 2008.

[70] N. Furukawa, A. Namiki, T. Senoo, and M. Ishikawa. Dynamic regrasping using a high-speed multifingered hand and a high-speed vision system. *Proc. of IEEE Int. Conf. on Robotics and Automation*, pages 181–187, 2006.

[71] K. Murakami, T. Senoo, and M. Ishikawa. High-speed catching based on inverse motion approach. *Proc. of IEEE Int. Conf. Robotics and Biomimetics*, pages 1308–1313, 2011.

[72] T. Senoo, D. Yoneyama, A. Namiki, and M. Ishikawa. Tweezers manipulation using high-speed visual servoing based on contact analysis. *Proc. of IEEE Int. Conf. Robotics and Biomimetics*, pages 1936–1941, 2011.

[73] Y. Yamakawa, A. Namiki, and M. Ishikawa. Card manipulation using a high-speed robot system with high-speed visual feedback. *Proc. of IEEE/RSJ Int. Conf. on Intelligent Robots and Systems*, pages 4762–4767, 2012.

[74] S. Huang, Y. Yamakawa, T. Senoo, and M. Ishikawa. A pre-compensation fuzzy logic algorithm designed for the dynamic compensation robotic system (under review).

[75] C. Lee. Fuzzy logic in control systems: Fuzzy logic controller - part 1 and part 2. *IEEE Trans. Syst. Man Cybernet*, 20(2):404–435, 1990.

[76] T. Ross. *Fuzzy logic with engineering applications (3rd ed.)*. John Wiley & Sons, 2010.

[77] J. Kim, S. Lee, and K. Kim. Fuzzy precompensation of pid controllers. *Proc. of IEEE conf. on Control Applications*, pages 183–188, 1993.

[78] S. Alavandar, T. Jain, and M. Nigam. Bacterial foraging optimized hybrid fuzzy precompensated pd control of two link rigid flexible manipulator. *Int. J. of Computational Intelligence Systems*, 2(1):51–59, 2009.

[79] The MathWorks Inc. Fuzzy logic toolbox user's guide. *Int. J. of Computational Intelligence Systems*.

[80] *http://www.k2.t.u-tokyo.ac.jp/fusion/DynamicCompensation/index-e.html*.

[81] D.E. Whitney. Quasi-static assembly of compliantly supported rigid parts. *J. Dyn. Syst., Meas., Control*, 104(1):65–77, 1982.

[82] I. Kim and D. Lim. Active peg-in-hole of chamferless parts using force/moment sensor. *Proc. of IEEE/RSJ Int. Conf. on Intelligent Robots and Systems*, pages 948–953, 1999.

[83] J. Wang, A. Liu, X. Tao, and H. Cho. Microassembly of micro peg-and-hole using uncalibrated visual servoing method. *Precision Engineering*, 32:173–181, 2008.

[84] R.J. Chang, C.Y. Lin, and P.S. Lin. Visual-based automation of peg-in-hole microassembly process. *J. of Manuf. Sci. Eng.*, 133(4):041015–1–12, 2011.

[85] B.H. Yoshimi and P.K. Allen. Active, uncalibrated visual servoing. *Proc. of IEEE Int. Conf. on Robotics and Automation*, pages 156–161, 1994.

[86] G. Morel, E. Malis, and S. Boudet. Impedance based combination of visual and force control. *Proc. of IEEE Int. Conf. on Robotics and Automation*, pages 1743–1748, 1998.

[87] S. Huang, Y. Yamakawa, T. Senoo, and M. Ishikawa. Realizing peg-and-hole alignment with one eye-in-hand high-speed camera. *Proc. of IEEE/ASME Int. Conf. on Advanced Intelligent Mechatronics*, pages 1127–1132, 2013.

[88] S. Huang, K. Murakami, Y. Yamakawa, T. Senoo, and M. Ishikawa. Fast peg-and-hole alignment using visual compliance. *Proc. of IEEE/RSJ Int. Conf. on Intelligent Robots and Systems*, pages 286–292, 2013.

[89] A. Castano and S. Hutchinson. Visual compliance: task-directed visual servo control. *IEEE Trans. on Robot. and Autom.*, 10(3):334–342, 1994.

[90] M.W. Spong, S.A. Hutchinson, and M. Vidyasagar. *Robot modeling and control*. John Wiley & Sons, 2006.

[91] C.C. Cheah. Task-space pd control of robot manipulators: Unified analysis and duality property. *Int. J. of Robotics Research*, 27(10):1152–1170, 2008.

[92] S. Grossberg. Nonlinear neural networks: Principles, mechanisms, and architecture. *Neural Networks*, 1(1):17–61, 1988.

[93] *http://www.k2.t.u-tokyo.ac.jp/fusion/PegHoleAlignment/*.

[94] The International Federation of Robotics IFR. History of industrial robots: From the first installation until today. 2012.